

Optical spectroscopy of charge-tunable atomically thin semiconductors at cryogenic temperatures

Jessica Lindlau



München 2019

Optical spectroscopy of charge-tunable atomically thin semiconductors at cryogenic temperatures

Dissertation
an der Fakultät für Physik
der Ludwig-Maximilians-Universität
München

vorgelegt von
Jessica Lindlau
geboren in München

München, den 31.01.2019

Erstgutachter: Prof. Dr. Alexander Högele
Zweitgutachter: Prof. Dr. Ursula Wurstbauer
Tag der mündlichen Prüfung: 26.03.2019

Zusammenfassung

Seit der mechanischen Isolierung von Graphen faszinieren atomar dünne zweidimensionale Materialien die Festkörperphysik. Eine interessante Gruppe der Dünnschichtmaterialien sind die halbleitenden Übergangsmetalldichalkogenide (TMDs) MoS_2 , MoSe_2 , WS_2 und WSe_2 , die sich durch ihre besonderen optischen und elektronischen Eigenschaften auszeichnen. Im Grenzfall der TMD Einzellage kommt es an den Bandkanten der ungleichen K und K' Randpunkte des reziproken Gitters zu einem Übergang von einer indirekten zu einer direkten Bandlücke. An diesen Randpunkten, die auch als Valleys bezeichnet werden, finden die optischen Übergänge statt. Durch ausgeprägte Licht-Materie-Wechselwirkung werden relaxierte Leitungsbandelektronen mit Leerstellen im Valenzband korreliert, die robuste und stark gebundene Exzitonen bilden. Diese Exzitonen sind energetisch zweifach entartet und weisen Valley-spezifische optische Auswahlregeln auf.

Im Rahmen dieser Arbeit wurden einzel- und doppelagige TMDs mit konfokaler Spektroskopie untersucht. Zunächst wurde die optische Anregung und Detektion der Valley-Quantenfreiheitsgrade an einzelnen MoS_2 Lagen erforscht. Der binäre Freiheitsgrad wurde durch Materialqualität als auch Phononen-Streuung beeinflusst, die sich auf den Relaxationsprozess optisch angeregter Exzitonen auswirken. In diesem Zusammenhang wurde, durch Störstellen begünstigte, verbotene Streuung zwischen Exzitonen und longitudinal optischen Phononen mit Raman-Spektroskopie identifiziert. In Kombination mit hyperspektralen Profilen der Raman-Intensitäten in externen Magnetfeldern wurden räumliche Veränderungen der Exziton-Phonon Wechselwirkung abgebildet.

Darüber hinaus zeigte sich die Exziton-Phonon Kopplung in den reich strukturierten Photolumineszenzspektren der TMDs. Die Zuordnung exzitonischer Merkmale ist allerdings umstritten, insbesondere wenn keine Kontrolle über das Ladungsniveau vorliegt. Im Ergebnis wurde zur Erklärung unbekannter Photolumineszenzlinien von TMD Einzellagen ein durch indirekte Übergänge erweitertes Modell entwickelt. Hierbei wurde unbekannte Emission mit akustischen und optischen Phononen-Seitenbanden von indirekten Exzitonen in Verbindung gebracht und durch umfangreiche Experimente unterstützt. Motiviert durch das Modell der TMD Einzellagen wurde außerdem ein detailliertes Verständnis der spektralen Signaturen von WSe_2 Doppellagen erarbeitet. Das Aufweichen strikter Impulserhaltung durch Verspannungen und Unordnung im Kristall ermöglichte ein Aufhellen indirekter Übergänge, wodurch die exzitonische Bandstruktur der WSe_2 Doppellage rekonstruiert werden konnte. Die zusätzliche Kontrolle über das Ladungsniveau bestätigte die Zuordnung der niederenergetischen indirekten Exzitonen. Diese Erkenntnisse tragen zum Verständnis der Materialeigenschaften von TMD Kristallen und zur Realisierung opto-valleytronischer Anwendungen bei.

Abstract

Two-dimensional layered materials have attracted much attention in condensed matter physics. Inspired by the mechanical exfoliation of graphene, a broad range of atomically thin materials are being explored today. A prominent class with intriguing optical and electronic properties includes the semiconducting transition metal dichalcogenides (TMDs) MoS₂, MoSe₂, WS₂, and WSe₂. They exhibit a crossover from an indirect band gap for multilayers to a direct band gap in the monolayer limit, with optical transitions in the visible to the near-infrared spectral range. At the energy minima of inequivalent K and K' valleys of monolayered TMDs, pronounced light-matter interactions correlate conduction band electrons and empty valence states to form robust and tightly bound excitons. These band-edge excitons are degenerate in energy and exhibit valley-dependent optical selection rules.

In the framework of this thesis, properties of TMD monolayers and bilayers were studied with optical spectroscopy. By this means, optical initialization and detection of valley pseudospins was demonstrated in monolayer MoS₂, as a representative material. The valley degree of freedom of photoexcited excitons was found to be influenced by relaxation processes that were strongly dependent on material quality and affected by phonon scattering. In this context, impurity-mediated forbidden scattering between excitons and longitudinal optical phonons was identified with Raman spectroscopy. These studies, combined with hyperspectral profiles of Raman mode intensities in external magnetic fields, revealed unexpected spatial variations of exciton-phonon interactions.

The role of exciton-phonon coupling was also established in the photoluminescence spectra of TMDs with rich excitonic signatures. Photoluminescence features are, however, controversial in their assignment, especially if doping control is unavailable. While dipole-allowed emission in monolayered TMDs is commonly attributed to momentum-direct transitions, lowest-energy emission in bilayer TMDs arises from momentum-indirect states. In this work, a model of momentum-indirect transitions was developed to explain previously unidentified photoluminescence peaks of monolayer TMDs. Their emission features were related to acoustic and optical phonon sidebands of momentum-indirect excitons and confirmed in comprehensive experiments. Motivated by the model for monolayer TMDs, a detailed understanding of spectral signatures of bilayer WSe₂ was also developed. Brightening of momentum-dark transitions by breaking strict momentum conservation with strain and disorder allowed to identify the bilayer excitonic band structure. Control of doping confirmed the assignment of low-energy momentum-dark states and allowed to determine their binding energy to an excess electron. The findings shed light on the origin of quantum dot formation in bilayer TMDs and facilitate advances directed towards opto-valleytronic device applications.

Contents

Zusammenfassung	i
Abstract	iii
List of publications	vii
List of abbreviations	ix
1 Introduction	1
2 Theoretical aspects of transition metal dichalcogenides	5
2.1 Crystal structure and electronic properties	6
2.2 Symmetry and optical selection rules	8
2.3 Fundamentals of valley excitons	10
2.4 Phonons and Raman scattering	13
3 Experimental setup for cryogenic optical spectroscopy	19
3.1 Optical setup	20
3.2 Collection efficiency	23
4 Optical properties of transition metal dichalcogenides	27
4.1 Introduction	28
4.2 Photoluminescence and Raman spectroscopy of MoS ₂	28
4.3 Fröhlich interactions in monolayer MoS ₂	31
4.4 Magneto-Raman imaging of mode intensities in monolayer MoS ₂	33
4.5 Conclusions	37
5 Momentum-dark excitons in monolayer semiconductors	39
5.1 Introduction	40
5.2 Spectral decomposition of monolayer photoluminescence	40
5.2.1 Analysis of MoSe ₂ emission	42
5.2.2 Analysis of WSe ₂ and WS ₂ emission	45
5.2.3 Momentum-indirect excitons in WSe ₂ and WS ₂	47
5.3 Conclusions	49

6	Exciton photoluminescence from monolayer tungsten diselenide	51
6.1	Introduction	52
6.2	Charge-tunable reflectance and photoluminescence	52
6.3	Photoluminescence evolution with excitation energy and power	54
6.4	Exciton decay dynamics	57
6.5	Exciton g -factors in WSe ₂ monolayers and bilayers	61
6.6	Conclusions	62
7	Momentum-dark excitons in bilayer systems	63
7.1	Introduction	64
7.2	Photoluminescence spectroscopy of bilayer WSe ₂	64
7.3	Excitons in bilayer WSe ₂	66
7.4	Effects of strain and local disorder	70
7.5	Field-effect control of doping in bilayer WSe ₂	74
7.6	Magneto-optical properties of bilayer quantum dots	77
7.7	Spectral signatures in MoSe ₂ -WSe ₂ heterobilayers	79
7.8	Conclusions	81
8	Summary and perspectives	83
	References	87

List of publications

- [P1] A. Neumann, **J. Lindlau**, M. Nutz, A. D. Mohite, H. Yamaguchi, and A. Högele. *Signatures of defect-localized charged excitons in the photoluminescence of monolayer molybdenum disulfide*. *Phys. Rev. Mater.* **2**, 124003 (2018).
- [P2] B. Miller, **J. Lindlau**, M. Bommert, A. Neumann, H. Yamaguchi, A. Holleitner, A. Högele, and U. Wurstbauer. *Tuning the Fröhlich exciton-phonon scattering in monolayer MoS₂*. ArXiv e-prints (2018). [arXiv:1811.09320](https://arxiv.org/abs/1811.09320).
- [P3] **J. Lindlau**, M. Selig, A. Neumann, L. Colombier, J. Förste, V. Funk, M. Förg, J. Kim, G. Berghäuser, T. Taniguchi, K. Watanabe, F. Wang, E. Malic, and A. Högele. *The role of momentum-dark excitons in the elementary optical response of bilayer WSe₂*. *Nat. Commun.* **9**, 2586 (2018).
- [P4] **J. Lindlau**, R. Cedric, V. Funk, J. Förste, M. Förg, L. Colombier, A. Neumann, E. Courtade, S. Shree, M. Manca, T. Taniguchi, K. Watanabe, M. M. Glazov, X. Marie, B. Urbaszek, and A. Högele. *Identifying optical signatures of momentum-dark excitons in monolayer transition metal dichalcogenides*. ArXiv e-prints (2017). [arXiv:1710.00988](https://arxiv.org/abs/1710.00988).
- [P5] M. Förg, L. Colombier, R. Patel, **J. Lindlau**, A. D. Mohite, H. Yamaguchi, D. Hunger, and A. Högele. *Cavity-control of bright and dark interlayer excitons in van der Waals heterostructures*. ArXiv e-prints (2017). [arXiv:1710.00990](https://arxiv.org/abs/1710.00990).
- [P6] A. Neumann*, **J. Lindlau***, and A. Högele. *Contamination of polymethylmethacrylate by organic quantum emitters*. ArXiv e-prints (2017). [arXiv:1706.08341](https://arxiv.org/abs/1706.08341).
- * These authors contributed equally to this work.
- [P7] A. Neumann, **J. Lindlau**, L. Colombier, M. Nutz, S. Najmaei, J. Lou, A. D. Mohite, H. Yamaguchi, and A. Högele. *Opto-valleytronic imaging of atomically thin semiconductors*. *Nat. Nanotechnol.* **12**, 329–335 (2017).
- [P8] T. Zhang, A. Neumann, **J. Lindlau**, Y. Wu, G. Pramanik, B. Naydenov, F. Jelezko, F. Schüder, S. Huber, M. Huber, F. Stehr, A. Högele, T. Weil, and T. Liedl. *DNA-Based Self-Assembly of Fluorescent Nanodiamonds*. *J. Am. Chem. Soc.* **137**, 9776–9779 (2015).

List of abbreviations

2D	two-dimensional
APD	avalanche photodiode
BL	bilayer
BS	beam splitter
BZ	Brillouin zone
CB	conduction band
CCD	charge-coupled device
CVD	chemical vapor deposition
CW	continuous-wave
DR	differential reflectivity
FL	fluorescence
FWHM	full-width at half-maximum
HBL	heterobilayer
hBN	hexagonal boron nitride
HBT	Hanbury Brown-Twiss
HWP	half-wave plate
IR	irreducible representation
LA	longitudinal acoustic
LO	longitudinal optical
LPF	long-pass filter

LPO	linear polarizer
ML	monolayer
NA	numerical aperture
ND	nanodiamond
NV	nitrogen-vacancy
PL	photoluminescence
PLE	photoluminescence excitation
QA	quasi-acoustic
QD	quantum dot
QWP	quarter-wave plate
QY	quantum yield
SPF	short-pass filter
TA	transverse acoustic
TMD	transition metal dichalcogenide
TO	transverse optical
VB	valence band
ZPL	zero-phonon line

Chapter 1

Introduction

New inventions are often triggered by curiosity, a basic instinct of mankind. Despite challenges, the path of research allows to follow new ways of thinking that lead to scientific breakthroughs and discoveries. The first approach to a profound understanding of nature was based on the inspection of the environment with light. Ever since, instruments and techniques were developed to discover physical laws at small and large dimensions. At the nanoscale, material properties are fundamentally different than at macroscopic dimensions and valuable for the development of novel technologies. This is reflected by the growing demand for new materials with versatile characteristics. As one example, the electronic and mechanical properties of graphene provide opportunities for flexible and wearable devices, data and energy storage, photodetectors, and batteries [1].

Following the footsteps of graphene [2, 3], new atomically thin materials featuring promising physical phenomena have emerged. Part of that class are the semiconducting transition metal dichalcogenides (TMDs) which include MoS_2 , MoSe_2 , WS_2 , and WSe_2 in the hexagonal H phase. Their diverse optical characteristics were studied in this thesis. In the monolayer (ML) limit, they exhibit a direct band gap in the visible to the near-infrared spectral range at the K and K' points of their hexagonal Brillouin zone (BZ) [4, 5]. These low-energy pockets or valleys are degenerate in energy but not equivalent. Broken inversion symmetry of the crystal lattice in combination with strong spin-orbit coupling lead to coupled spin and valley degrees of freedom of band-edge charge carriers [6]. Strong light-matter coupling facilitates pronounced absorption, where Coulomb interactions correlate electrons and empty valence band states to form tightly bound excitons. While optical dipole transitions of lowest-energy excitons in molybdenum-based MLs are spin-allowed, the exciton ground state of ML tungsten dichalcogenides WSe_2 and WS_2 is spin-dark [7–14]. This difference stems from a reversed energetic ordering of spin-polarized conduction subbands in molybdenum and tungsten dichalcogenide MLs [15–19]. Despite

this distinction, the K and K' valleys of both material subclasses can be conveniently addressed with circularly polarized light of opposite helicity [20–28]. These binary states therefore have promising potential for atomically thin optoelectronic and opto-valleytronic applications [29, 30]. As such, successful conversion of electrical information to optical polarization was demonstrated with chiral light emitting diodes [31, 32] and the reversed transformation by the valley Hall effect in ML MoS₂ [33]. Apart from ML TMDs, bilayers (BLs) are also relevant for technological applications due to their significance as hosts for single photon sources [34, 35], finite valley polarization [36], and potential utilization of the spin-layer locking effect [37]. They exhibit a momentum-indirect band gap and their properties are tunable by the alignment angle between the two layers [38, 39].

TMD MLs and BLs can be mechanically exfoliated from bulk crystals similar to the first isolation of graphene [40], or grown macroscopically by molecular beam epitaxy or chemical vapor deposition (CVD) [41–43]. While exfoliation often results in highest quality samples, the latter growth techniques are relevant for large scale commercial applications. CVD-grown crystals, in particular, are susceptible to molecular adsorption and crystal defects such as grain boundaries, which lead to rapid valley decoherence of excitons and therefore reduce the material quality. The exposed crystal surface is furthermore susceptible to fast nonradiative decay mechanisms that cause spectrally broad luminescence with reduced photon emission. On the other hand, defects and strain can induce useful single photon emission with properties known from self-assembled quantum dots (QDs) [34, 44–49], and deterministic formation of TMD QDs may provide new avenues towards scalable quantum arrays [35].

In this work, confocal photoluminescence (PL) and Raman spectroscopy were used to study TMD MLs and BLs. Basic material properties were investigated by analyzing Raman modes of the crystal which are sensitive to the number of layers [50], temperature [51], strain [52, 53], adsorbate deposition [54], and charge doping [55]. In MoS₂ MLs defect-mediated forbidden scattering between excitons and in-plane optical phonons was examined for excitation near-resonant with the fundamental exciton. Enhanced exciton-phonon interactions were accompanied by valley depolarization and valley decoherence of excitons [22, 23]. With cryogenic mapping of Raman mode intensities in magnetic fields, spatial variations of crystal quality and local environment were identified. Field-dependent correlations between Raman scattering intensities and polarization-resolved PL indicated that exciton valley dynamics are linked to Raman processes and their optical selection rules.

Complementary to Raman spectroscopy, band-edge excitons were characterized with PL spectroscopy and differential reflectivity (DR). In the presence of additional charges, excitons [56–58] can form charged three-particle complexes or trions with

binding energies of roughly 30 meV [59, 60]. Owing to the coincidence of almost identical trion binding and optical phonon energies in TMD MLs [61, 62], spectral signatures of samples even with active charge control remain controversial to date [63]. In this work, unidentified peaks in charge-controlled cryogenic PL spectra were explained in terms of phonon sideband replicas of momentum-dark excitons. The concept of theoretically predicted momentum-indirect excitons in MLs was further investigated with experiments. To support our model, these included studies of the exciton PL excitation (PLE) power dependence, polarization properties, radiative lifetime, and measurements of exciton g -factors.

As opposed to the direct electronic band gap in MLs, the indirect band gap of BL crystals results in reduced PL with richly structured spectra [64]. Despite intense research the intricate signatures in PL and absorption of BL MoSe₂, WS₂, and WSe₂ remain only insufficiently explained. A closed interpretation of emission spectra of BL WSe₂ as arising from both momentum-bright and momentum-dark exciton manifolds was developed in this work. Moreover, a microscopic understanding of bright QD emission arising from strained defect sites was acquired. These localized QD excitons in WSe₂ BL were used as sensors for the intrinsic material properties of the host crystal. Furthermore, the spectral evolution with doping was used to verify the hierarchy of lowest-energy excitons and allowed to determine trion binding energies of momentum-dark excitons in BL WSe₂. The conclusions apply to the entire class of BL TMDs and are not specific to WSe₂.

Scope of the thesis

Within the framework of this thesis, optical properties of TMD MLs and BLs were studied with optical spectroscopy. The main experimental results are either published or in preparation for publication.

First, basic theoretical concepts of the electronic and optical properties of TMDs are introduced (Chapter 2). Interband optical selection rules and the role of spin- and momentum-dark excitons in ML and BL TMDs are discussed. The latter excitons require interactions with phonons for emission. Phonon selection rules and their modification as a result of interactions with electrons or excitons are elaborated.

The performance of the confocal microscope was characterized with nitrogen-vacancy (NV) color centers in diamond as reference quantum emitters (Chapter 3). Fundamental PL and Raman characteristics of ML MoS₂, as a representative TMD, are described in Chapter 4. The degree of circular and linear polarization of the PL and Raman scattering was analyzed for excitation resonant with the fundamental

exciton. Mapping of Raman mode intensities was then used to characterize crystal quality and exciton-phonon interactions influenced by an external magnetic field.

A model to identify spectral PL signatures of TMD MLs based on momentum-dark excitons is introduced in Chapter 5 and substantiated with experiments on charge-tunable ML WSe₂ in Chapter 6. The discussion is followed by a comprehensive interpretation for BL WSe₂ emission spectra on the basis of both momentum-bright and momentum-dark excitons (Chapter 7). Strain- and defect-induced brightening of momentum-dark excitons in BL WSe₂ was used to identify the excitonic band structure. Finally, Chapter 8 provides a summary and perspectives of this work.

Chapter 2

Theoretical aspects of transition metal dichalcogenides

This chapter provides an overview of the electronic and optical properties of semi-conducting atomically thin TMDs. In the monolayer form, they feature a direct band gap in the visible to the near-infrared spectral range at the K and K' points or valleys of their hexagonal Brillouin zone. Due to the presence of spin-orbit coupling, this valley pseudospin of band-edge states is coupled to their spin degree of freedom and leads to valley-dependent optical selection rules of interband transitions. Based on a lattice symmetry analysis, we derive these optical selection rules and discuss the fundamental characteristics of valley excitons that are formed by strong Coulomb interactions. Finally, we introduce interactions of excitons and electrons with phonons, that give rise to photoluminescence features and anomalous Raman selection rules.

2.1 Crystal structure and electronic properties

THIS SECTION IS PARTLY BASED ON THE MANUSCRIPT [P4](#):

J. Lindlau, R. Cedric, V. Funk, J. Förste, M. Förg, L. Colombier, A. Neumann, E. Courtade, S. Shree, M. Manca, T. Taniguchi, K. Watanabe, M.M. Glazov, X. Marie, B. Urbaszek, and A. Högele. *Identifying optical signatures of momentum-dark excitons in monolayer transition metal dichalcogenides*. ArXiv e-prints (2017). [arXiv:1710.00988](#).

TMDs are layered materials of MX_2 sheets bound together by van der Waals forces, where M are transition metal atoms and X are chalcogen atoms. From this family, we study atomically thin crystals of the semiconducting group-VIB TMDs MoS_2 , MoSe_2 , WS_2 , and WSe_2 [30, 65–67]. Similar to graphene [40], they can be mechanically exfoliated from bulk crystals, or grown by either CVD [41, 42] or molecular beam epitaxy [43]. The crystal structure of single layers can exhibit three different phase configurations 1H, 1T, and 1T' [68]. In the hexagonal 1H arrangement, the individual layers consist of three covalently bonded atomic planes X-M-X in ABA stacking without a center of inversion (Figs. 2.1a and 2.1b). The 1T phase with rhombohedral (ABC) stacking is typically unstable and transforms into the 1T' form with 1D zigzag chains of M atoms [68]. This rare 1T' phase is interesting for quantum spin Hall physics and is naturally formed by WTe_2 MLs [69, 70]. In this thesis, we focus on the properties of group-VIB TMDs with the 1H lattice.

In bulk form, the crystals exhibit an indirect band gap which increases in energy when the number of layers is reduced and transforms to a direct band gap in the visible to the near-infrared spectral range for MLs. For this limit, band extrema are found at the K and K' points of the hexagonal BZ (Fig. 2.1c) of the honeycomb lattice [4, 5]. At these points, the main contributions to the conduction band (CB) and valence band (VB) states stem from d_{z^2} and d_{xy} , $d_{x^2-y^2}$ orbitals of the transition metal atoms, respectively [15, 71]. The degenerate energy minima or valleys are related by time-reversal symmetry, that combined with missing inversion symmetry imposes valley-contrasting out-of-plane Berry curvatures and orbital magnetic moments on band-edge states [6, 30]. Together with strong spin-orbit coupling, VB states exhibit large spin splittings Δ_{SO} of several hundreds of meV as estimated from first-principles calculations [15–17, 19, 71] and determined experimentally [36, 43]. The pronounced spin polarization of the VB is mainly attributed to chiral orbital compositions $d_{x^2-y^2} + id_{xy}$ ($d_{x^2-y^2} - id_{xy}$) with a magnetic quantum number of $m = +2$ ($m = -2$) for the K (K') valley. The CB spin splitting on the order of a few tens of meV [15–17, 19] is much smaller. It originates from minor band contributions of chalcogen p -orbitals and transition metal d_{xz} , d_{yz} orbitals to the dominant

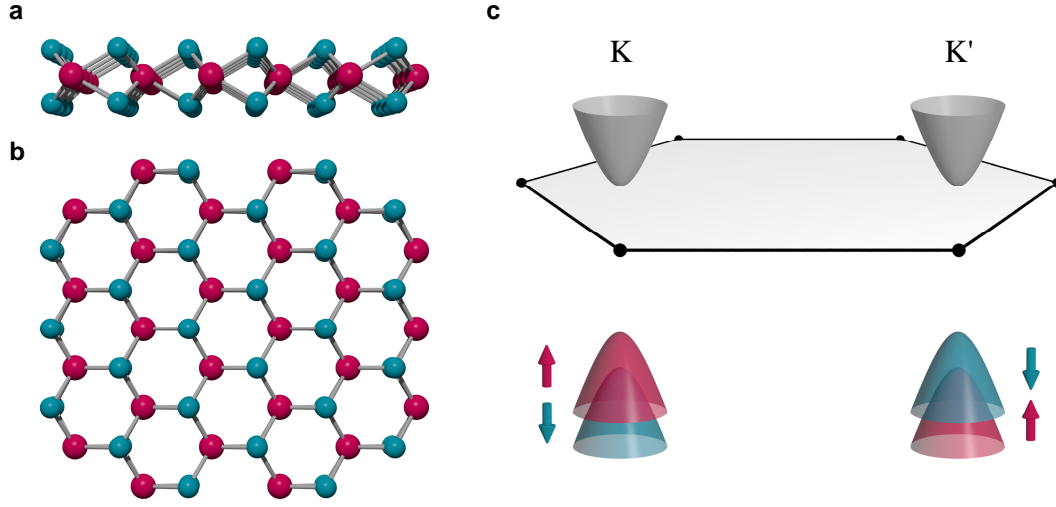


Figure 2.1: **a** and **b**, Real space lattice schematics of a MX_2 transition metal dichalcogenide monolayer in the 1H phase: side and top views, respectively, with transition metal (chalcogen) atoms in red (cyan). **c**, Schematic of the first Brillouin zone with hyperbolic band dispersions at the K and K' points. For simplicity, spin-orbit splitting is shown only for the valence subbands, that give rise to X and B excitons. Note that the spin-polarized subbands at K and K' are related by time reversal.

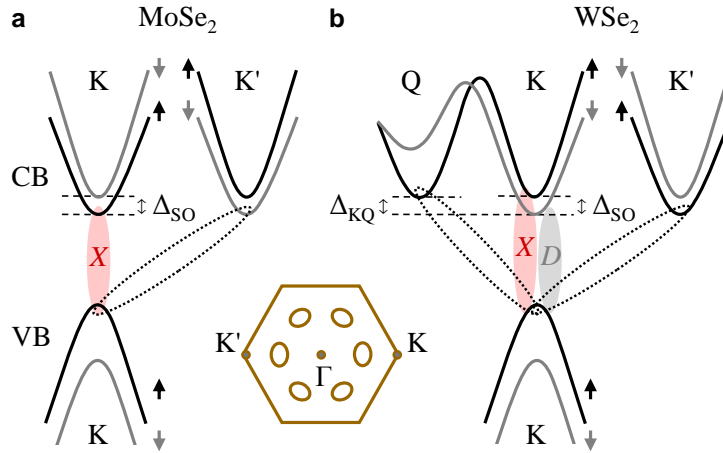


Figure 2.2: **a** and **b**, Schematic band structure in the first Brillouin zone (inset with high-symmetry points Γ , K and K' , and six inequivalent Q pockets) of molybdenum and tungsten dichalcogenide monolayers, respectively. Conduction band (CB) and valence band (VB) with spin-up and spin-down electron subbands (shown in black and gray, respectively), spin-orbit splitting Δ_{SO} , and the energy separation Δ_{KQ} between the conduction band minima at K and Q . Momentum-direct spin-bright and spin-forbidden excitons (X and D , indicated by ellipses shaded in red and gray) are formed by electrons and unoccupied states in the K valley. Momentum-dark excitons (dashed ellipses) with the empty state at K can be formed with electrons at Q or K' .

d_{z^2} character of the band with $m = 0$ [15, 17]. The interplay of their competing coupling to spin leads to reversed ordering of conduction subbands between ML molybdenum and tungsten dichalcogenides (Figs. 2.2a and 2.2b). In addition to the K and K' valleys, the CB of TMD MLs exhibits local minima at six nonequivalent Q pockets related pairwise by time-reversal symmetry (Fig. 2.2) [64, 72]. Depending on the specific material, the Q-valley band edges can be as far as $\Delta_{KQ} \simeq 160$ meV above the CB minimum as in MoSe₂, or in the range of ~ 0 –80 meV in tungsten-based MLs [19, 61, 73].

The photophysics of ML TMDs are dominated by strong Coulomb interactions that correlate band-edge CB electrons with empty states in the VB to form tightly bound excitons. They are commonly categorized according to their spin-polarized VB states into the lower-energy X excitons and their excited B counterparts. Each complex furthermore exhibits spin-bright and spin-dark electron-hole configurations arising from the conduction subbands. At the K and K' points, the excitons are valley-degenerate and are characterized by optical selection rules with valley-contrasting circular dichroism (see Section 2.2). This valley degeneracy of optical transitions can be lifted by a perpendicular magnetic field, which relies on an asymmetry of the orbital magnetic moments in the conduction and valence subbands with the same spin for a given valley [74–77]. The resulting valley Zeeman splitting between the K'- and K-valley excitons can be quantified by an effective exciton g -factor, with $g \approx 4$ for spin-bright X states [74–77] that are the lowest-energy excitons in MoS₂ and MoSe₂. For tungsten dichalcogenide MLs the exciton ground state is spin-forbidden [7–14] (Figs. 2.2a and 2.2b) and exhibits an exciton g -factor of ~ 9.4 as determined for ML WSe₂ [78, 79]. Beside spin-bright and spin-forbidden excitons, tungsten-based TMD MLs feature momentum-dark excitons with the empty state at K and electrons at K' or Q (Fig. 2.2).

2.2 Symmetry and optical selection rules

Optical selection rules for interband transitions in TMD MLs can be derived with group theory analysis. For an odd number of layers, inversion symmetry is broken and the space group symmetry reduces from D_{6h}^4 for bulk crystals to D_{3h}^1 for MLs. The subgroup C_{3h} of the ML D_{3h}^1 symmetry forms the group of the wavevector at the K and K' points. The two main symmetry operations of C_{3h} are C_3 and σ_h , which represent a $2\pi/3$ rotation around the z axis and horizontal reflection at the plane of transition metal atoms, respectively. Using these symmetry properties and $\mathbf{k} \cdot \mathbf{p}$ perturbation theory, a two-band Hamiltonian of the form [6, 18]

$$\hat{\mathcal{H}} = at(\tau k_x \hat{\sigma}_x + k_y \hat{\sigma}_y) + \frac{\Delta}{2} \hat{\sigma}_z - \lambda_v \tau \frac{\hat{\sigma}_z - 1}{2} \hat{s}_z + \lambda_c \tau \frac{\hat{\sigma}_z + 1}{2} \hat{s}_z \quad (2.1)$$

can be obtained to describe band-edge states with small wavevectors \mathbf{k} around the K and K' points. Here, a is the lattice constant, Δ the energy gap (without spin-orbit coupling), and t the effective hopping integral between the d -orbitals of the transition metal atoms including indirect interactions mediated by p -orbitals of the chalcogen atoms [15, 80]. The Pauli matrices $\hat{\sigma}$ act on the basis states, that are constructed with d_{z^2} , $d_{x^2-y^2}$, and d_{xy} orbitals of the transition metal atoms and are given by

$$|\psi_c\rangle = |d_{z^2}\rangle, \quad (2.2a)$$

$$|\psi_v^\tau\rangle = \frac{1}{\sqrt{2}}(|d_{x^2-y^2}\rangle + i\tau |d_{xy}\rangle), \quad (2.2b)$$

where the subscript c (v) indicates the CB (VB) and $\tau = \pm 1$ is the valley index (+1 for K and -1 for K') [6]. The basis states are adapted to the symmetry of the system at K and K', where the Bloch amplitudes correspond to the irreducible representations (IRs) Γ_1 in Eq. 2.2a and Γ_2 (Γ_3) in Eq. 2.2b for $\tau = +1$ ($\tau = -1$). The IRs are given in the Koster notation [81] and a transition metal atom is chosen to be the origin of point transformations. The second to last term in Eq. 2.1 accounts for spin-orbit coupling in the VB and stems from transition metal $d_{x^2-y^2}$ and d_{xy} orbitals. The VB spin splitting is given by $2\lambda_v$ and \hat{s}_z denotes the third Pauli matrix for spin. The last term of Eq. 2.1 is a phenomenological correction to the two-band model and accounts for the CB spin splitting ($2\lambda_c$). It corrects for coupling to remote transition metal d_{xz} and d_{yz} orbitals, and contributions from chalcogen p -orbitals [66].

In the two-band framework, where distant bands are ignored, the spin z component s_z is a good quantum number. The spin parts recast the Bloch amplitudes as additional products with spinors corresponding to $s_z = \pm 1/2$ with IRs $\Gamma_7(\uparrow)$ and $\Gamma_8(\downarrow)$ [82]. This results in K and K' IRs of $\Gamma_1 \times \Gamma_7 = \Gamma_7(\uparrow)$ and $\Gamma_1 \times \Gamma_8 = \Gamma_8(\downarrow)$ for the spin-polarized conduction subbands, and $\Gamma_2 \times \Gamma_7 = \Gamma_{10}(\uparrow)$ and $\Gamma_3 \times \Gamma_8 = \Gamma_9(\downarrow)$ for the upper valence subbands, respectively. In general, spin-orbit coupling introduces admixing of remote subbands that exhibit the same IR and different spins [14]. This becomes relevant for optical transitions among subbands with antiparallel spins (spin-dark transitions).

The optical selection rules for dipole-allowed interband transitions at K and K' are derived according to the transformation $\Gamma_c \times \Gamma_v^*$, where Γ_c (Γ_v) is the IR of the conduction (valence) subband and $\hat{\mathcal{T}}\Gamma_v = \Gamma_v^*$ is the time-reversed IR in the C_{3h} group [82]. The bright transitions involving the upper valence subbands and conduction subbands with the same spin are characterized by

$$\Gamma_7 \times \Gamma_{10}^* = \Gamma_2 \quad \text{and} \quad \Gamma_8 \times \Gamma_9^* = \Gamma_3, \quad (2.3)$$

for $\tau = +1$ and $\tau = -1$, and transform as $x+iy$ and $x-iy$, respectively. They describe dipoles of $1s$ -type X excitons (see next section) that are addressed by σ^+ and σ^- circularly polarized light with the electric field in the ML plane. In PL experiments, these selection rules are probed by the degree of circular and linear polarization, P_c and P_l , measured as the ratio of emission intensities $(I_{co} - I_{cr})/(I_{co} + I_{cr})$ that are detected in co-polarized (I_{co}) and cross-polarized (I_{cr}) configurations with a circularly or linearly polarized excitation laser. While P_c provides a direct measure of valley polarization [20–22], P_l quantifies coherent superpositions of K and K' transitions [23, 36] (see Section 4.2).

In contrast to the spin-bright transitions, the class of spin-dark transitions couples to light with out-of-plane polarization. Their IRs are determined by

$$\Gamma_8 \times \Gamma_{10}^* = \Gamma_4 \quad \text{and} \quad \Gamma_7 \times \Gamma_9^* = \Gamma_4. \quad (2.4)$$

These transitions are forbidden for excitation or detection at normal incidence but can be observed in experiments with a high numerical aperture (NA) objective [14].

2.3 Fundamentals of valley excitons

Excitons in ML TMDs exhibit an exceptionally large binding energy of roughly 0.5 eV. It arises from spatial confinement of out-of-plane motion, reduced screening of the dielectric environment, and large effective masses of band-edge states [83]. The excitons are largely of Wannier-Mott type as their wave functions extend over several unit cells with a Bohr radius of ~ 1 nm [84].

An exciton state $|S_{\mathbf{Q}}\rangle$, labeled by index S and center-of-mass momentum \mathbf{Q} , can be expanded as [85, 86]

$$|S_{\mathbf{Q}}\rangle = \sum_{vck} A_{vc\mathbf{Q}}^S(\mathbf{k}) |vck\mathbf{Q}\rangle. \quad (2.5)$$

In a two-band model, $c = \{s_c, \tau_c\}$ and $v = \{s_v, \tau_v\}$ denote the spin and valley indices of CB and VB single-particle states with wave vectors around K or K'. The states $|vck\mathbf{Q}\rangle$ are free electron-hole pairs consisting of an electron in $|ck + \mathbf{Q}\rangle$ and an empty state $\hat{T}|vk\rangle$, and the amplitudes $A_{vc\mathbf{Q}}^S(\mathbf{k})$ are Fourier transforms of the exciton envelope functions. The energy difference $E_{\mathbf{Q}}^S$ between an excited eigenstate and the crystal ground state is obtained by solving a set of simultaneous equations [86, 87]

$$[E_c(\mathbf{k} + \mathbf{Q}) - E_v(\mathbf{k})] A_{vc\mathbf{Q}}^S(\mathbf{k}) + \sum_{v'c'\mathbf{k}'} \langle vck\mathbf{Q} | \hat{K}^d + \hat{K}^x | v'c'\mathbf{k}'\mathbf{Q} \rangle A_{v'c'\mathbf{Q}}^S(\mathbf{k}') = E_{\mathbf{Q}}^S A_{vc\mathbf{Q}}^S(\mathbf{k}), \quad (2.6)$$

where $E_c(\mathbf{k} + \mathbf{Q})$ and $E_v(\mathbf{k})$ are single-electron CB and VB energies. The terms \hat{K}^d and \hat{K}^x denote the direct and exchange parts of the electron-hole interaction kernel with

$$\begin{aligned} & \langle v c \mathbf{k} \mathbf{Q} | \hat{K}^d | v' c' \mathbf{k}' \mathbf{Q} \rangle \\ &= - \int d\mathbf{r}_e d\mathbf{r}_h \psi_{c, \mathbf{k} + \mathbf{Q}}^*(\mathbf{r}_e) \psi_{v, \mathbf{k}}(\mathbf{r}_e) V(\mathbf{r}_e - \mathbf{r}_h) [\hat{\mathcal{T}} \psi_{v, \mathbf{k}}(\mathbf{r}_h)]^* [\hat{\mathcal{T}} \psi_{v', \mathbf{k}'}(\mathbf{r}_h)], \end{aligned} \quad (2.7a)$$

$$\begin{aligned} & \langle v c \mathbf{k} \mathbf{Q} | \hat{K}^x | v' c' \mathbf{k}' \mathbf{Q} \rangle \\ &= \int d\mathbf{r}_e d\mathbf{r}_h \psi_{c, \mathbf{k} + \mathbf{Q}}^*(\mathbf{r}_e) [\hat{\mathcal{T}} \psi_{v, \mathbf{k}}(\mathbf{r}_e)] V(\mathbf{r}_e - \mathbf{r}_h) \psi_{v', \mathbf{k}'}(\mathbf{r}_h) [\hat{\mathcal{T}} \psi_{v', \mathbf{k}'}(\mathbf{r}_h)]^*. \end{aligned} \quad (2.7b)$$

The wave functions $\psi_{c, \mathbf{k} + \mathbf{Q}}$ and $\psi_{v, \mathbf{k}}$ are eigenfunctions of the Hamiltonian in Eq. 2.1 and $V(\mathbf{r}_e - \mathbf{r}_h) = e^2 / (\kappa |\mathbf{r}_e - \mathbf{r}_h|)$ is the electron-hole interaction potential modified by the effective dielectric constant κ of the crystal (e is the elementary charge).

If the electron-hole exchange interaction \hat{K}^x is neglected, the exciton envelope functions and eigenenergies of exciton states in the effective-mass theory satisfy the hydrogen-like wave equation [87]

$$\left(-\frac{\hbar^2}{2\mu} \nabla_{\mathbf{r}}^2 - \frac{\hbar^2}{2M} \nabla_{\mathbf{R}}^2 - \frac{e^2}{\kappa r} \right) A_{vc\mathbf{Q}}^S(\mathbf{r}, \mathbf{R}) = \epsilon_{\mathbf{Q}}^S A_{vc\mathbf{Q}}^S(\mathbf{r}, \mathbf{R}), \quad (2.8)$$

where \hbar is the reduced Planck constant, $\mathbf{r} = \mathbf{r}_e - \mathbf{r}_h$ is the electron-hole separation, $\mathbf{R} = (m_e \mathbf{r}_e + m_h \mathbf{r}_h) / (m_e + m_h)$ with electron and hole effective masses m_e and m_h , and $\epsilon_{\mathbf{Q}}^S = E_{\mathbf{Q}}^S - E_g$ with the band gap E_g . The reduced and total exciton masses are given by $\mu = m_e m_h / (m_e + m_h)$ and $M = m_e + m_h$, respectively. The solutions of Eq. 2.8 with only in-plane motion form valley-degenerate excitonic bands

$$\epsilon_{\mathbf{Q}}^S = \frac{\hbar^2 Q^2}{2M} - \frac{R_y}{(n - 1/2)^2}, \quad (2.9)$$

with $R_y = \mu e^4 / (2\hbar^2 \kappa^2)$ and the principle quantum number $n \in \mathbb{N}^+$ describing the states $1s$, $2s$, etc. In absorption experiments, the exciton series of energy levels within the light cone deviates from the two-dimensional (2D) hydrogenic model due to nonlocal dielectric screening of Coulomb interactions induced by the strong dependence of $\kappa = \kappa(\mathbf{r})$ on the electron-hole separation of the exciton state [56, 57].

We continue with the main effects arising from the exchange term in Eq. 2.6 for lower-energy excitons associated with the upper valence subband. To this end, we construct an orthonormal basis set of Bloch-type valley excitons (with valley indices

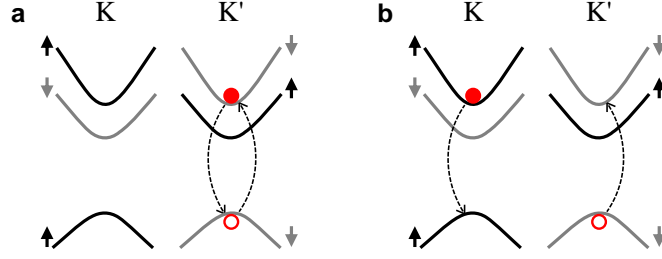


Figure 2.3: Schematic band structure at high-symmetry points K and K' in the first Brillouin zone of tungsten dichalcogenide monolayers. **a** and **b**, Mechanisms for electron-hole exchange interactions with intravalley and intervalley coupling, respectively.

$\tau = +1$ and -1) from K and K' states at $\mathbf{Q} = 0$ to expand eigenstates $|S_{\mathbf{Q}}\rangle$ with small \mathbf{Q} . These basis states can be written as [86, 88]:

$$|S_{\mathbf{Q}}^{\tau}\rangle \approx |e^{i\mathbf{Q}\cdot\mathbf{R}}S_0^{\tau}\rangle = \sum_{v\mathbf{c}\mathbf{k}} A_{v\mathbf{c}\mathbf{0}}^{S^{\tau}}(\mathbf{k}) |v\mathbf{c}\mathbf{k}\mathbf{Q}\rangle. \quad (2.10)$$

For spin-dark valley excitons the exchange term is negligible and zero if spin states are pure [86]. Thus, with the basis of spin-bright (X) excitons given above, Eq. 2.6 reduces to a 2×2 matrix. The corresponding matrix elements of the exchange interaction can be separated into long and short range parts, each including intravalley and intervalley components, $J_{\mathbf{Q}}^{\text{intra}}$ and $J_{\mathbf{Q}}^{\text{inter}}$, respectively. For TMD MLs, the short range intervalley part is zero due to the threefold rotational symmetry of the lattice [89]. Up to the leading order in \mathbf{Q} , the terms $J_{\mathbf{Q}}^{\text{intra}}$ and $J_{\mathbf{Q}}^{\text{inter}}$, corresponding to an interaction between the exciton momentum $\mathbf{Q} = (Q \cos \theta, Q \sin \theta)$ and its valley pseudospin τ , are given by [86, 89]:

$$\langle S_{\mathbf{Q}}^{\tau} | \hat{K}^x | S_{\mathbf{Q}}^{\tau'} \rangle_{\tau=\tau'} = J_{\mathbf{Q}}^{\text{intra}} \approx V(\mathbf{Q}) \frac{Q^2 D^2}{2e^2 a_B} + C, \quad (2.11a)$$

$$\langle S_{\mathbf{Q}}^{\tau} | \hat{K}^x | S_{\mathbf{Q}}^{\tau'} \rangle_{\tau \neq \tau'} = J_{\mathbf{Q}}^{\text{inter}} \approx V(\mathbf{Q}) \frac{Q^2 D^2}{2e^2 a_B} e^{i(\tau' - \tau)\theta}, \quad (2.11b)$$

where $V(\mathbf{Q}) = 2\pi e^2 / (Q\kappa)$ is the 2D Coulomb interaction in momentum space, a_B is the exciton Bohr radius, and the constant term C is the matrix element of the short range intravalley exchange interaction. The quantity $D^2 = 2(eat/E_g)^2$, with a and t defined in Eq. 2.1, is the squared modulus of the electric-dipole transition matrix element for electron-hole pair creation at the K or K' point [89, 90]. The two processes, $J_{\mathbf{Q}}^{\text{intra}}$ and $J_{\mathbf{Q}}^{\text{inter}}$ (Figs. 2.3a and 2.3b), give rise to an overall energy shift and coupling of the two valley configurations for the bright X exciton, causing valley depolarization on fast timescales [82, 91, 92].

Modified by the exchange interaction, the bright $1s$ X exciton with mass M and energy E_0^{1s} at $\mathbf{Q} = 0$ splits into two branches of equal superpositions of the two valleys. It is characterized by the dispersion [83, 86]

$$E_{\mathbf{Q}}^{1s} = E_0^{1s} + \frac{\hbar^2 Q^2}{2M} + J_{\mathbf{Q}}^{\text{intra}} \pm |J_{\mathbf{Q}}^{\text{inter}}|, \quad (2.12)$$

with eigenstates $|S_L\rangle$ and $|S_U\rangle$ for the lower and upper branches

$$|S_L\rangle = \frac{1}{\sqrt{2}}(e^{-i\theta}|S_{\mathbf{Q}^+1}\rangle - e^{i\theta}|S_{\mathbf{Q}^-1}\rangle), \quad (2.13a)$$

$$|S_U\rangle = \frac{1}{\sqrt{2}}(e^{-i\theta}|S_{\mathbf{Q}^+1}\rangle + e^{i\theta}|S_{\mathbf{Q}^-1}\rangle). \quad (2.13b)$$

Within the light cone, the lower (upper) branch couples to linearly polarized light with longitudinal (transverse) electric-field orientation along \mathbf{Q} . The upper branch shows close to linear dispersion of a massless Dirac particle with chirality 2 due to the threefold rotational symmetry of the lattice [83, 86, 93]. At the edge of the light cone, the splitting of the two branches is estimated to be on the order of a few meV and around 12 meV under a moderate strain of 1% for zero momentum [89].

2.4 Phonons and Raman scattering

Beside momentum-direct interband transitions, momentum-dark excitons also contribute to the optical signatures of molybdenum dichalcogenide MLs and even dominate the PL of tungsten-based ML and BL crystals at low temperatures (see Chapters 5–7). Radiative relaxation of momentum-dark excitons requires either localization of the exciton wavefunction or scattering with a phonon to fulfill momentum-conservation which is discussed in the following. The phonons relevant for exciton-phonon interactions in TMD MLs and BLs are the in-plane transverse and longitudinal acoustic (TA, LA) and analogous optical phonon modes (TO, LO) with E' symmetry, and the out-of-plane A_1 optical vibration with A' symmetry [61]. The normal displacements of the optical modes in a ML are sketched in Figs. 2.4a and 2.4b for the out-of-plane and in-plane vibrations, respectively. Note that we use the common molecular notation to describe phonon scattering processes.

For phonon-assisted recombination of a Q -momentum-indirect exciton (Q -valley electron and K -valley empty state, see Fig. 2.2), the CB electron can scatter a phonon to compensate for the momentum mismatch. The symmetry of the participating phonon is determined by the IRs of the initial (Γ_i) and final (Γ_f) electron state as $\Gamma_f^* \times \Gamma_i$. Therefore, the intersection between the symmetry groups C_s and C_{3h} of initial and final electron states at the Q and K points needs to be considered, which

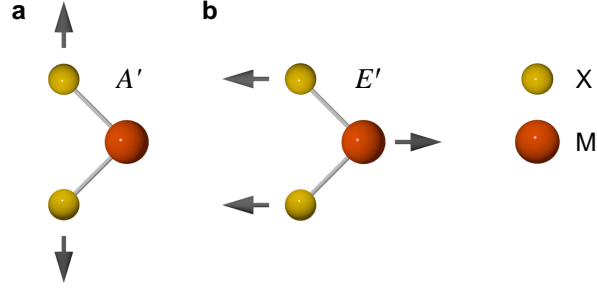


Figure 2.4: **a** and **b**, Schematics of normal displacements for the out-of-plane (A') and in-plane (E') optical vibration modes in monolayer MX_2 . The labels in molecular notation A' and E' indicate the symmetry at the K and K' points.

is C_s . In this symmetry group, subband states are represented by $\Gamma_3(\uparrow)$ and $\Gamma_4(\downarrow)$. With this considered, spin-conserving electron scattering with the IR Γ_1 is mediated by A' phonons. The analogue of these phonons in C_{3h} corresponds to acoustic E' and optical E' and A_1 phonons [81]. Provided that momentum conservation is fulfilled, combinations of these phonons are also allowed. Spin-conserving scattering processes of spin-like indirect excitons with Q momentum ensure photon emission with the polarization defined by the valley of the empty state. Transitions between the K and K' valleys can be considered analogously. For spin-conserving scattering they are enabled by phonon modes with E' symmetry (Γ_2), and for spin-flip transitions they are induced by A'' (Γ_4) or by E'' (Γ_5) phonons. Note that these spin-flip processes are possible due to a finite admixture of bands, with opposite spin orientations, that increases for momenta away from high symmetry points. Real intervalley spin flips can, however, be mediated by chiral phonons [94].

While optical selection rules of excitonic transitions mediated by phonons are determined by the symmetries of electron states, Raman scattering is governed by the lattice symmetry if Fröhlich interactions are negligible [95]. These interactions describe the coupling between electrons and the crystal polarization field induced by LO phonons. In the unperturbed limit, the scattered Raman intensity I_s is proportional to the Raman tensor \mathcal{R} :

$$I_s \propto |\mathbf{e}_i \cdot \mathcal{R} \cdot \mathbf{e}_s|^2, \quad (2.14)$$

where \mathbf{e}_i and \mathbf{e}_s are unity polarization vectors of the incident and scattered radiation, respectively. The Raman tensor expresses the modifications of the electric susceptibility (χ) induced by atomic vibrations:

$$\mathcal{R} = (\partial\chi/\partial\mathbf{u})_{\mathbf{u}=0} \cdot \mathbf{e}_{\mathbf{u}}(\omega_0), \quad (2.15)$$

where \mathbf{u} is the vector displacement of a given lattice atom, $\mathbf{e}_{\mathbf{u}} = \mathbf{u}/|\mathbf{u}|$ is a unit vector parallel to the phonon displacement, and ω_0 the phonon frequency. For A' and E' vibrations in a lattice with D_{3h} symmetry, \mathcal{R} is given by [96]:

$$A' : \begin{pmatrix} a & 0 & 0 \\ 0 & a & 0 \\ 0 & 0 & b \end{pmatrix}, \quad (2.16a)$$

$$E'(\text{LO}) : \begin{pmatrix} 0 & d' & 0 \\ d' & 0 & 0 \\ 0 & 0 & 0 \end{pmatrix}, \quad E'(\text{TO}) : \begin{pmatrix} d & 0 & 0 \\ 0 & -d & 0 \\ 0 & 0 & 0 \end{pmatrix}. \quad (2.16b)$$

With this, it is straightforward to derive the selection rules of the respective Raman processes. For circularly or linearly polarized incident fields, A' scattering is co-polarized with the initial polarization state. Both LO and TO components of E' are cross-polarized under circular excitation, whereas the TO (LO) component exhibits co-polarized (cross-polarized) scattering under linear excitation. Thus, unpolarized E' Raman scattering is observed for linearly polarized excitation of LO and TO components that are degenerate in energy.

In the presence of charge carriers or excitons, the scattering process of phonons can be described with Feynman diagrams. A representative Feynman diagram of a one-phonon Stokes Raman process is shown in Fig. 2.5. An initial photon with frequency ω_i interacts with an electron via excitation of a virtual exciton state X with energy E_X which is characterized by the electron-radiation interaction Hamiltonian $\hat{\mathcal{H}}_{\text{eR}}$ (filled sphere). Subsequently, the virtual exciton state X couples to a phonon via the electron-phonon interaction Hamiltonian $\hat{\mathcal{H}}_{\text{e-ion}}$ (open square). The emitted phonon is described by the Stokes Raman process and the virtual state X transforms to X' with energy $E_{X'}$. In the last step, the virtual exciton state X' interacts with the radiation field, scattering a photon with energy $\hbar\omega_s$. The scattering probability (\mathcal{P}) from the initial state $|i\rangle$ with energy E_i as given by Fermi's golden rule can be written as [95]

$$\mathcal{P} = \frac{2\pi}{\hbar} \left| \sum_{XX'} \frac{\langle i | \hat{\mathcal{H}}_{\text{eR}}(\omega_s) | X' \rangle \langle X' | \hat{\mathcal{H}}_{\text{e-ion}} | X \rangle \langle X | \hat{\mathcal{H}}_{\text{eR}}(\omega_i) | i \rangle}{[\hbar\omega_i - (E_X - E_i)] [\hbar\omega_i - \hbar\omega_0 - (E_{X'} - E_i)]} \right|^2 \delta(\hbar\omega_i - \hbar\omega_0 - \hbar\omega_s). \quad (2.17)$$

Here, we assume that the Raman scattering leaves the final electronic state unchanged from the initial state $|i\rangle$. In the limit of the electric-dipole approximation, the interaction Hamiltonian between the radiation and an electron is given by

$$\hat{\mathcal{H}}_{\text{eR}} = -e\mathbf{r} \cdot \mathbf{E}, \quad (2.18)$$

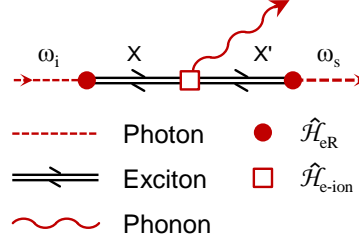


Figure 2.5: Feynman diagram of the one-phonon Stokes scattering process (see Ref. 95). The frequencies of the initial and scattered photons are denoted by ω_i and ω_s . X and X' are the excited and transformed virtual exciton states. Filled spheres mark the electron-radiation interaction Hamiltonian $\hat{\mathcal{H}}_{eR}$ and the open square denotes the electron-phonon interaction Hamiltonian $\hat{\mathcal{H}}_{e-ion}$.

with the electric field \mathbf{E} and the relative coordinate vector \mathbf{r} between the electron and hole.

The electron-phonon interaction Hamiltonian, $\hat{\mathcal{H}}_{e-ion}$, can have different contributions. Acoustic phonons interact with electrons via piezoelectric coupling associated with strain induced to the crystal, and long-wavelength optical phonons involve relative displacements of atoms regarded as microscopic distortions. In polar crystals, deformation-potential interactions of LO phonons induce an oscillating macroscopic polarization leading to an electric field \mathbf{E}_{LO} , which couples to electrons through Fröhlich interactions as [95]

$$\mathbf{E}_{LO} = -F\mathbf{u}_{LO} \quad \text{with} \quad F = [4\pi N\mu_p\omega_{LO}^2(\epsilon_\infty^{-1} - \epsilon_0^{-1})]^{1/2}. \quad (2.19)$$

The phonon amplitude \mathbf{u}_{LO} is the relative displacement of the negative to the positive ion, N is the number of unit cells per unit volume, μ_p is the reduced mass of the primitive cell defined as $\mu_p^{-1} = M_1^{-1} + M_2^{-1}$ (M_1 and M_2 are the masses of the two atoms in the cell), ω_{LO} is the LO phonon frequency, and ϵ_∞ and ϵ_0 are the high- and low-frequency dielectric constants, respectively. The Fröhlich Hamiltonian for this interaction is given by [95]

$$\hat{\mathcal{H}}_{Fr} = (ieF/q)u_{LO}, \quad (2.20a)$$

$$u_{LO} = \left(\frac{\hbar}{2N\mu_p\omega_{LO}} \right)^{1/2} \{ \hat{c}_q^+ \exp[i(\mathbf{q} \cdot \mathbf{r} - \omega_{LO}t)] + \text{c.c.} \}. \quad (2.20b)$$

Here, \mathbf{q} is the phonon wavevector, \hat{c}_q^+ is the phonon creation operator, and c.c. stands for the complex conjugate.

The Fröhlich Hamiltonian for exciton-phonon interactions ($\hat{\mathcal{H}}_{\text{Fr},X}$) follows similar considerations. For a $1s$ hydrogenic exciton state with Bohr radius a_B , the matrix element of $\hat{\mathcal{H}}_{\text{Fr},X}$ is given by [95]

$$\left| \langle 1s | \hat{\mathcal{H}}_{\text{Fr},X} | 1s \rangle \right| = \frac{C_F}{q} \left(\frac{1}{[1 + (p_h a_B q / 2)^2]^2} - \frac{1}{[1 + (p_e a_B q / 2)^2]^2} \right), \quad (2.21a)$$

$$C_F = e \left(\frac{2\pi \hbar \omega_{\text{LO}}}{NV_p} (\epsilon_\infty^{-1} - \epsilon_0^{-1}) \right)^{1/2}, \quad (2.21b)$$

where p_e and p_h are defined as $m_e/(m_e + m_h)$ and $m_h/(m_e + m_h)$, respectively, and V_p is the primitive cell. When excitons form resonant intermediate states, the wavevector dependence of the matrix element has strong influence on the selection rule for LO phonons as was shown in Ref. 97 for bulk CdS. This work confirmed large enhancement of forbidden scattering with polarization parallel to the incident radiation, independent of the crystal symmetry. For near-resonant Raman scattering with the $1s$ X exciton in ML MoS₂, we observed similar results (see Section 4.3 and Ref. P2).

Chapter 3

Experimental setup for cryogenic optical spectroscopy

PARTS OF THIS CHAPTER ARE ADAPTED WITH PERMISSION FROM REF. P8:

T. Zhang, A. Neumann, J. Lindlau, Y. Wu, G. Pramanik, B. Naydenov, F. Jelezko, F. Schüder, S. Huber, M. Huber, F. Stehr, A. Högele, T. Weil, and T. Liedl. *DNA-Based Self-Assembly of Fluorescent Nanodiamonds*. *J. Am. Chem. Soc.* **137**, 9776–9779 (2015).
Copyright 2015 American Chemical Society.

This chapter describes the confocal microscope used for room-temperature and cryogenic hyperspectroscopy. The optical resolution of the system at room temperature was sufficient to discern individual fluorescent nanodiamonds in dimer assemblies with ~ 400 nm separation. The collection efficiency of the microscope was benchmarked with a reference single-photon emitter, a nitrogen-vacancy center in bulk diamond. In comparison with the room-temperature performance, 67% of the fluorescence intensity was detected with low-temperature optics.

3.1 Optical setup

Measurements of PL, DR, and Raman spectroscopy were conducted at room and low temperatures with a home-built fiber-based confocal microscope (Fig. 3.1). The microscope was operated in back-scattering geometry and connected to a spectrometer¹ with a liquid nitrogen-cooled silicon charge-coupled device² (CCD) for spectroscopy with a resolution ranging from 0.5 meV to 0.05 meV. A combination of linear polarizers³ (LPOs) and achromatic quarter- and half-wave plates⁴ (QWPs and HWPs) in the excitation and detection optical paths enabled full polarization analysis. Optionally, the wave plates were mounted on piezo rotators⁵ for automated polarization-resolved spectroscopy (see Section 4.4). For cryogenic studies, the microscope was mounted in liquid helium at 4.2 K or in a closed-cycle cryostat⁶ with a base temperature of 3.1 K. The cryostat was equipped with a solenoid providing magnetic fields up to ± 9 T. Time-resolved studies were conducted with an avalanche photodiode⁷ (APD) or a streak camera⁸ (temporal resolution of ~ 0.3 ns or ~ 6 ps, respectively). Measurements of photon statistics were accomplished with two APDs in a Hanbury Brown and Twiss configuration [98].

For optical characterization of samples, a variety of laser sources was required. A 532 nm continuous-wave (CW) laser^{9,10} or a diode laser¹¹ tunable between 635–639 nm were used for PL and Raman spectroscopy. PL studies were also conducted with a home-built CW diode laser at 670 nm, a ps-pulsed diode laser¹² at 630 nm, or a Ti:sapphire laser¹³ operated either in CW mode or ps-pulsed mode in combination with a synchronously pumped optical parametric oscillator¹⁴. The latter configuration was used for subnanosecond time-resolved measurements. A ps-pulsed supercontinuum laser¹⁵ was used for DR measurements and to measure nanosecond PL lifetimes. Spectral filtering was accomplished with suitable combinations of short-pass filters (SPFs), long-pass filters (LPFs), and tunable band-pass filters¹⁶.

¹PI, Acton SP-2558

²PI, Spec-10:100BR/LN

³Thorlabs, LPVIS and LPVISB series

⁴B. Halle, RAC 3 series

⁵attocube systems, ANR240/RES

⁶attocube systems, attoDRY1000

⁷PicoQuant, τ -SPAD

⁸Hamamatsu, C5680-24S

⁹Coherent, Verdi G15

¹⁰CNI, MLL-III-532-50-1

¹¹New Focus, Velocity TLB-6704

¹²PicoQuant, LDH-P-C-630

¹³Coherent, Mira 900

¹⁴Coherent, Mira-OPO

¹⁵NKT Photonics, SuperK EXW-12

¹⁶Semrock, RazorEdge and VersaChrome series

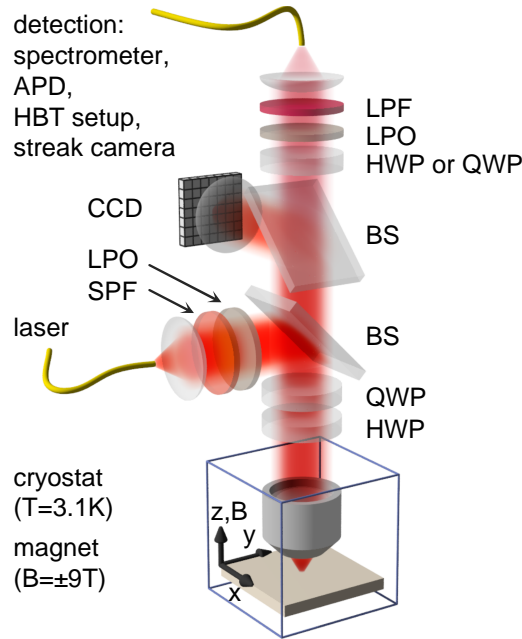


Figure 3.1: Schematic of the fiber-based confocal setup used for photoluminescence, differential reflectance, and Raman spectroscopy. Laser light collimated from a single-mode fiber was passed through a short-pass filter (SPF) and linear polarizer (LPO) before it was reflected off a beam splitter (BS) and guided to the sample through a focusing objective. In between, quarter- and half-wave plates (QWP and HWP) were used for polarization control. Signal collected by the objective was transmitted through the same wave plates, a polarization-maintaining BS pair, and was analyzed with a HWP or QWP and a LPO for polarization-resolved detection. Before being coupled into a single-mode fiber, the signal was spectrally filtered with a long-pass filter (LPF). Reflected laser light at the upper BS was imaged with a charge-coupled device (CCD) camera for microscope adjustment and sample orientation. The detection fiber was either coupled to a spectrometer, a single-photon counting avalanche photodiode (APD), a Hanbury Brown and Twiss (HBT) setup for autocorrelation experiments, or a streak camera. Samples were positioned in x , y , and z directions with a piezo scanner and piezo steppers into the focal spot of the objective. The microscope was operated either at room or low temperature in a helium bath or a closed-cycle cryostat (indicated by the blue box) with a base temperature of 3.1 K and capable of magnetic fields of up to ± 9 T. Modified from Ref. 99.

At low temperatures, the samples were positioned with piezo steppers and a piezo scanner¹⁷ into the diffraction-limited full-width at half-maximum (FWHM) spot of $0.6 \mu\text{m}$ diameter of an apochromatic objective¹⁸ with a NA of 0.82. High-resolution room-temperature experiments were performed with another objective¹⁹

¹⁷attocube systems, ANP101 series and ANSxy100/lr

¹⁸attocube systems, LT-APO/VISIR/0.82

¹⁹Olympus, UMPlanFl 100x/0.90 BD

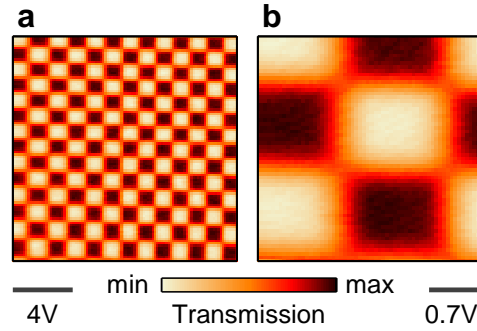


Figure 3.2: **a** and **b**, Color-coded optical transmission maps of a gold grid with $2\ \mu\text{m}$ periodicity. The data were used for calibration of the x , y piezo scanner at room temperature for applied voltages of 15 V and 3 V, respectively.

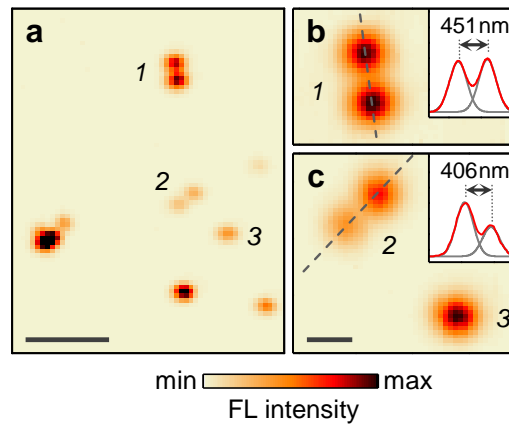


Figure 3.3: **a**, Color-coded confocal fluorescence map of nanodiamond dimer assemblies; the data was obtained at room temperature and 532 nm excitation. The dimers were assembled with DNA-origami nanotechnology and appear as pairs or individual fluorescence hotspots in the confocal map (scale bar is $2\ \mu\text{m}$). **b** and **c**, Zoom-in on nanodiamond dimers with corresponding line scans fitted with two Gaussians (scale bar is 400 nm).

(NA of 0.90). Prior to raster-scan measurements with high spatial precision, piezo scanner nonlinearities were determined as a function of applied voltage. Figs. 3.2a and 3.2b show optical transmission maps through a gold grid with $2\ \mu\text{m}$ periodicity on fused silica for travel ranges of 15 V and 3 V, respectively. From Fig. 3.2a we obtained mean x and y expansions of 840 nm and 930 nm per applied volt. Within the first three volts the piezo scanner, however, exhibited smaller values of 710 nm/V in x and 870 nm/V in y (Fig. 3.2b).

Combined with the room-temperature objective (NA of 0.90), the setup enabled confocal fluorescence (FL) imaging at the limit of diffraction. This allowed to identify

individual fluorescent nanodiamond (ND) dimers assembled with DNA nanotechnology (see Ref. P8 for details on sample fabrication). Fluorescent NDs emerge as a class of biocompatible markers with stable and robust optical characteristics due to their inert surface. They host several color centers including NV centers with a characteristic zero-phonon line (ZPL) at 637 nm accompanied by Stokes and anti-Stokes phonon sidebands between 600 nm and 700 nm. A room-temperature FL raster scan of fluorescent ND dimers on quartz, excited at 532 nm and with collection above 575 nm, is shown in Fig. 3.3a. With a spatial resolution of ~ 355 nm, the data revealed ND separations of 451 nm and 406 nm for two representative dimers (Figs. 3.3b and 3.3c). The measured values were well within the limits of the expected maximum center-to-center distance of 476 nm (see Ref. P8).

3.2 Collection efficiency

Apart from the spatial resolution given by the diffraction-limited excitation and detection spots, the collection efficiency is another key property of the setup. We estimate it by benchmarking an emitter of well known optical properties, a single NV color center in bulk diamond. A representative room-temperature FL spectrum of a single NV center is shown in Fig. 3.4a. The spectrum exhibited a ZPL at 637 nm and typical Raman signal of bulk diamond around 610 nm for excitation at 532 nm [100]. The single-photon statistics in the second-order coherence of the FL (inset of Fig. 3.4a) confirmed that only a single NV center was recorded. The histogram obtained at 330 kW/cm² and an acquisition time of 1000 s exhibited pronounced antibunching well below 0.5 at zero time delay, with overlaid bunching that is characteristic for high excitation powers [100].

Fig. 3.4b shows the excitation power dependence of the dipole orientation averaged NV center for circularly polarized excitation and detection with a fiber-coupled silicon APD. The NV FL (brown) was cleared from background emission of contaminant FL and Raman scattered photons (gray), that was separately measured away from the NV center. The fits to the data indicate a linear response of the background intensity and a saturation behavior for the NV center with maximum intensity (I_{\max}) of ~ 77 kcts/s. Compared to Ref. 101, the measured intensity was about a factor of 2.5 lower, if differences in collection angles of the objectives are accounted for. The losses likely occurred at the coupling interface to the single-mode detection fiber.

A more quantitative estimate of the collection efficiency using the NV center can be obtained by considering its radiative lifetime and FL quantum yield (QY), given by the ratio of emitted photons to absorbed photons per unit time. Time-resolved measurements of a representative NV center revealed biexponential decay with a FL lifetime of ~ 13 ns (Fig. 3.5a). The second decay contribution of ~ 3.3 ns stemmed

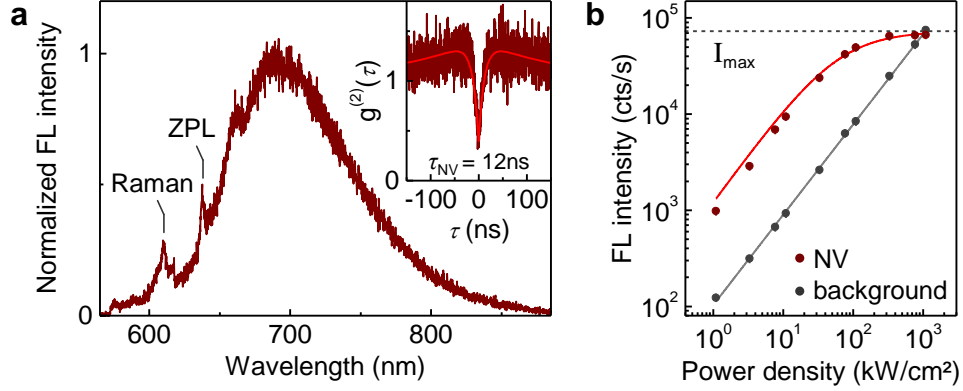


Figure 3.4: Optical properties of a nitrogen-vacancy (NV) center in bulk diamond, for room-temperature setup calibration using an Olympus, UMPlanFl 100x/0.90 BD, objective. **a**, Normalized fluorescence of an NV center with a characteristic zero-phonon line (ZPL) at 637 nm. The labeled Raman signal is characteristic for bulk diamond under the used 532 nm excitation. Inset: Second-order coherence as a function of delay time τ for a single NV center showing pronounced antibunching. The fit (red trace) yields a fluorescence lifetime of ~ 12 ns. **b**, Fluorescence power dependence under circularly polarized excitation of the same emitter (brown) with a saturation intensity maximum of ~ 73 kcts/s above the background signal (gray). The data was collected with a fiber-coupled avalanche photodiode.

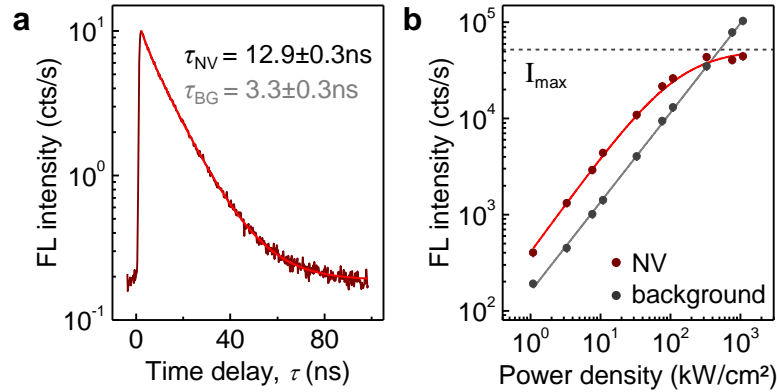


Figure 3.5: **a**, Temporal evolution of the fluorescence intensity for a single nitrogen-vacancy (NV) center in bulk diamond, red line is a biexponential fit to the data. The two transients stem from the radiative decay of the NV center ($\tau_{\text{NV}} = 12.9 \pm 0.3$ ns) and background signal ($\tau_{\text{BG}} = 3.3 \pm 0.3$ ns) **b**, Fluorescence power dependence under circularly polarized excitation of the same emitter (brown) with a maximum intensity (I_{max}) of ~ 52 kcts/s above the background signal (gray). All measurements were conducted at room temperature with an apochromatic objective (attocube systems, LT-APO/VISIR/0.82) and a fiber-coupled avalanche photodiode.

from background contaminant FL and was weak in magnitude (8%). The NV FL lifetime corresponds to a maximum photon emission rate of $\sim 5.4 \times 10^7 \text{ s}^{-1}$ if the QY of 70% for NV centers in bulk diamond is taken into account [102]. Thus, the measured I_{max} corresponds to 0.2% of the maximum photon emission rate.

The collection efficiency of the apochromat²⁰ used for low-temperature spectroscopy was determined at room temperature. Using this objective, the excitation power dependence of a single NV center (brown) and the background signal (gray) were again measured with circularly polarized excitation at 532 nm (Fig. 3.5b). The maximum FL intensity at saturation of the NV center was with 52 kcts/s a factor of 1.2 lower than for the high-performance room-temperature objective²¹ if the different of collection angles are considered (Fig. 3.4). The drawback of this reduced collection efficiency is, however, outbalanced by the benefits of the low-temperature applicability.

²⁰attocube systems, LT-APO/VISIR/0.82

²¹Olympus, UMPlanFl 100x/0.90 BD

Chapter 4

Optical properties of transition metal dichalcogenides

THIS CHAPTER IS PARTLY BASED ON THE PUBLICATION [P7](#) AND THE MANUSCRIPT [P2](#): A. Neumann, J. Lindlau, L. Colombier, M. Nutz, S. Najmaei, J. Lou, A.D. Mohite, H. Yamaguchi, and A. Högele. *Opto-valleytronic imaging of atomically thin semiconductors*. *Nat. Nanotechnol.* **12**, 329–335 (2017).

B. Miller, J. Lindlau, M. Bommert, A. Neumann, H. Yamaguchi, A. Holleitner, A. Högele, and U. Wurstbauer. *Tuning the Fröhlich exciton-phonon scattering in monolayer MoS₂*. ArXiv e-prints (2018). [arXiv:1811.09320](#).

In this chapter, optical selection rules in monolayer MoS₂ as a representative material are explored at cryogenic temperatures and excitation resonant with the blue shoulder of the ground-state exciton. For this resonance condition, we find symmetry-forbidden Raman scattering of longitudinal optical phonons in the limit of Fröhlich interactions. Moreover, crystal inhomogeneities caused by local strain and grain boundaries are visualized with macroscopic mapping of Raman scattered photons. In external magnetic fields of up to 9 T applied perpendicular to the crystal surface, our results indicate a dependence of Raman mode intensities on the valley Zeeman effect and exciton-phonon interactions.

4.1 Introduction

The valley degree of freedom manifests itself as the quantized angular motion of crystal electrons near the band edges. In analogy to spin it represents a resource for quantum information in conventional semiconductors such as aluminum arsenide [103] and silicon [104], or in atomically thin materials including graphene [105] and TMDs [6, 30]. Direct band-gap ML TMDs [4, 5] are particularly viable for practical realizations of valleytronic concepts as they enable initialization [6], manipulation [24], and detection [20–22] of the valley pseudospin by all-optical means. For excitation in resonance with the blue shoulder of the ground-state exciton, we study the valley pseudospin in ML MoS₂ with PL experiments at cryogenic temperatures.

Complementary to PL, Raman spectroscopy provides versatile and powerful means for the inspection of material quality being sensitive to the number of layers [50], charge doping [55], and strain fields [52] in TMD semiconductors. Moreover, exciton photophysics are connected to Raman scattering probabilities. Exciton-phonon interactions strongly influence phonon scattering and limit valley polarization and valley coherence of excitons [22, 23]. In our studies, Raman selection rules for ML MoS₂ are characterized at room and cryogenic temperatures under nonresonant and near-resonant excitation conditions with respect to the fundamental exciton. Additionally, we implement cryogenic 2D mapping of Raman mode intensities for MoS₂ ML crystals grown by CVD and transferred onto silicon oxide substrates. By raster-scanning the sample with respect to the confocal excitation and detection spots of $\sim 0.7 \mu\text{m}$ in diameter, we acquired spatial maps of MoS₂ flakes at 3 K and magnetic fields of up to 9 T. We observed significant inhomogeneities in the characteristics of Raman modes and interpret our findings on the basis of Raman scattering probabilities influenced by the exciton-laser detuning and exciton-phonon interactions.

4.2 Photoluminescence and Raman spectroscopy of MoS₂

A representative cryogenic PL spectrum of ML MoS₂ recorded with nonresonant excitation at 2.33 eV (532 nm) is shown in Fig. 4.1a. It features fundamental X and excited B exciton resonances around 1.9 eV and 2.0 eV, characteristic of MLs on SiO₂ [4, 5]. Additionally, the PL exhibited a redshifted peak near 1.7 eV stemming from localized excitons L . In contrast to a linear response of X excitons to excitation power, L excitons exhibited saturation [P7, 106].

In the following, we discuss the valley photophysics of X excitons. The valley degree of freedom of these band-edge excitons is conveniently addressed with PL polarimetry [30]. The degrees of circular and linear PL polarization, P_c and P_l , defined

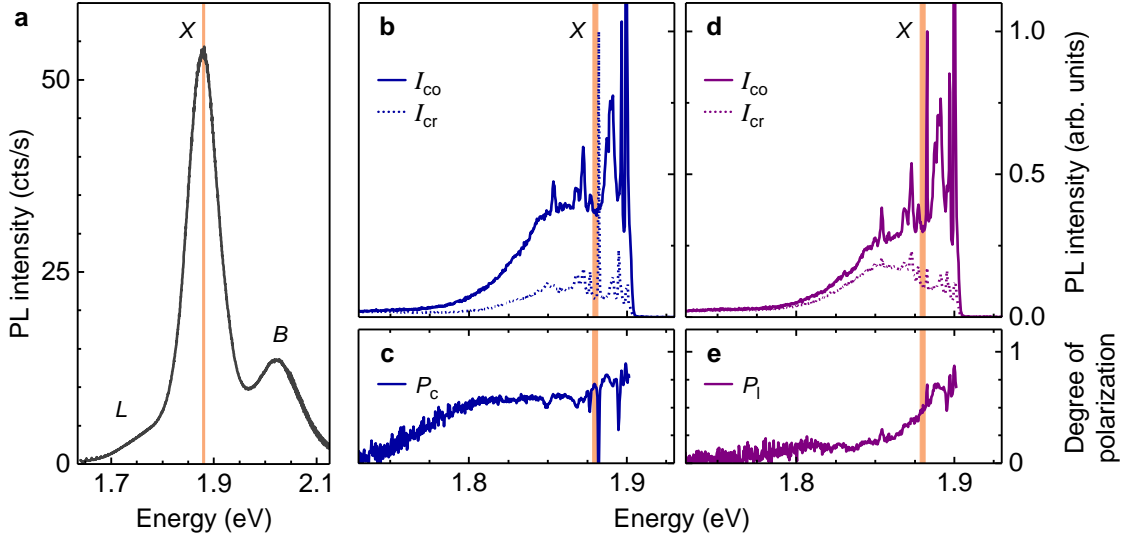


Figure 4.1: **a**, Cryogenic photoluminescence spectrum of monolayer MoS₂ under non-resonant excitation at 2.33 eV showing *X*, *B*, and low-energy (*L*) exciton features. **b**, Photoluminescence spectra recorded in co-polarized (solid trace, I_{co}) and cross-polarized (dashed trace, I_{cr}) configurations with circularly polarized excitation near-resonant with *X*. **c**, Corresponding degree of circular polarization P_c . **d**, Co- and cross-polarized photoluminescence spectra under linearly polarized near-resonant excitation and **e**, degree of linear polarization P_l . The red bands of same width indicate the PL maximum of *X* excitons. All measurements were recorded at 3 K on a regular monolayer region. For **b–e** an excitation laser at 1.95 eV and a long-pass filter at 1.90 eV were used; sharp features correspond to Raman scattered photons.

as the ratio of emission intensities $P = (I_{co} - I_{cr}) / (I_{co} + I_{cr})$ detected in co-polarized (I_{co}) and cross-polarized (I_{cr}) configurations with a circularly or linearly polarized excitation laser, are direct measures of valley polarization [20–22] and valley coherence [23, 36] (Figs. 4.1b–4.1e). Most values reported for degrees of circular and linear PL polarization in ML TMDs are below unity, and vary significantly with material quality, underlying substrate, and the excitation energy with respect to the ground-state exciton [20–22, 37, 92, 107–109]. Moreover, long-range exchange interactions between the electron and correlated empty state forming an exciton with finite momentum within the light cone give rise to exciton depolarization (see Section 2.3) [82, 91, 92]. In our experiments with excitation near-resonant with *X*, typical values for P_c reached up to 0.8 for *X* and decreased continuously below 1.8 eV, where emission from localized excitons became dominant (Fig. 4.1c). Note that the sharp spectral features (Figs. 4.1b–4.1e) stemming from Raman scattered photons exhibited different polarization selection rules. In contrast to P_c , the value of P_l was more sensitive to the spectral detuning from the excitation laser (Fig. 4.1e). Emission of localized

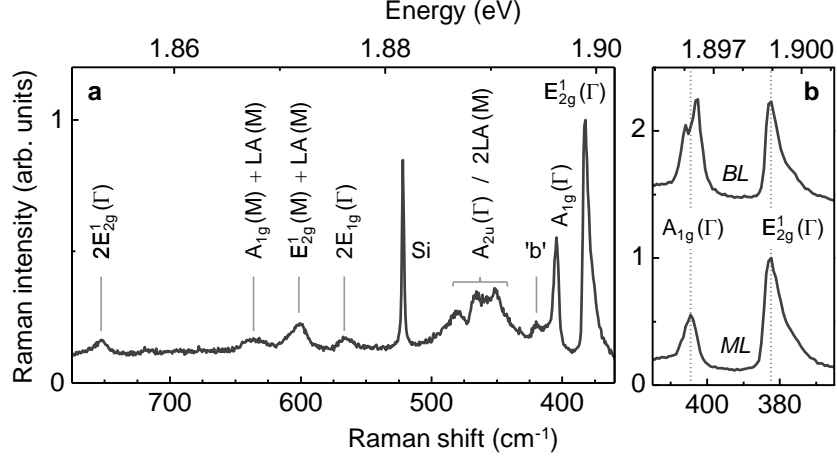


Figure 4.2: Raman spectra of monolayer and bilayer MoS₂ recorded at regular defect-free positions. **a**, Spectrum for near-resonant excitation at 1.95 eV with Raman modes assigned according to the MoS₂ bulk notation of Ref. 112. **b**, Spectra of the E_{2g}¹(Γ) and A_{1g}(Γ) Raman modes for near-resonant excitation at 1.95 eV on representative monolayer (ML) and bilayer (BL) positions; data were offset for clarity and dashed lines are guides to the eye. The splitting of the A_{1g}(Γ) mode is characteristic of bilayer transition metal dichalcogenides under resonant excitation [113]. All measurements were obtained at 3 K.

excitons below 1.8 eV as well as of excitons bound to excess charges (trions) that were spectrally overlapped with X excitons (see the Supplementary Information of Ref. P7) reduced P_1 already for small redshifts away from X . Charged excitons are especially susceptible to fast optical decoherence [110] and effects of electron-hole exchange [23]. The robustness of the valley degree of freedom in our measurements was therefore impaired by trion emission as well as disorder-induced localization of excitons at crystal defects or trapped charges [85, 111]. In addition, scattering of excitons with phonons also influence valley polarization and coherence [22, 23].

We studied the latter interactions with Raman spectroscopy in resonance with the blue shoulder of the ground-state exciton. A representative Raman spectrum obtained at a regular ML position with mode assignments given in bulk notation [112] is shown in Fig. 4.2. The two most pronounced peaks at 386 cm⁻¹ and 407 cm⁻¹ correspond to the in-plane E_{2g}¹ LO mode and the out-of-plane A_{1g} homopolar mode (see Fig. 2.4) [50]. The splitting of ~ 21 cm⁻¹ between the two modes is typical for low temperatures [51]. For basic characterizations, the Raman spectra were useful to identify BL regions, where the A_{1g}(Γ) mode exhibited a characteristic splitting [113] shown in Fig. 4.2b. A comprehensive discussion of the A_{1g}, E_{2g}¹, and other modes is provided in the following two sections.

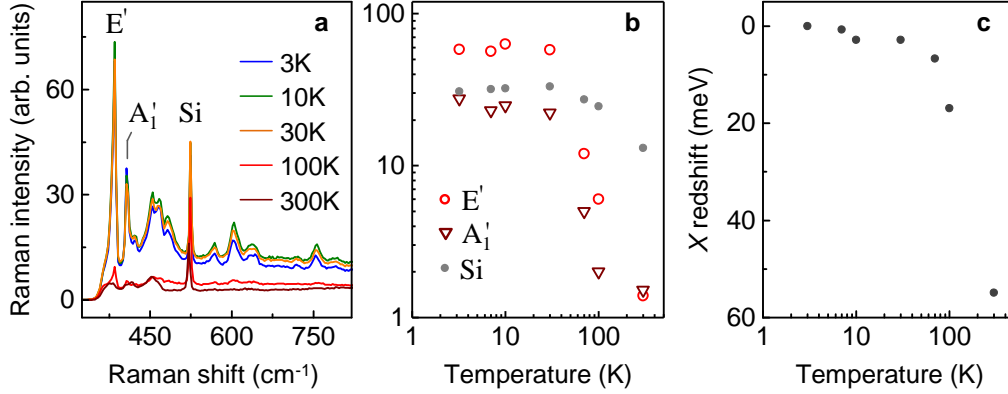


Figure 4.3: **a**, Evolution of monolayer MoS₂ Raman mode intensities for temperatures ranging from 3 K to 300 K under near-resonant excitation at 1.95 eV. **b**, Intensities of the E' (red), A₁' (brown), and silicon (Si, gray) Raman modes as a function of temperature. A sharp decrease in intensity is observed above 30 K for all MoS₂ Raman features, that was less pronounced for the silicon line. **c**, Temperature-induced redshift of the X resonance with respect to the 3 K energy of 1.864 eV (the data was acquired with excitation at 2.33 eV).

4.3 Fröhlich interactions in monolayer MoS₂

Raman spectroscopy is a major tool to identify and characterize materials. Raman scattered photons exhibit polarization-dependent optical selection rules, where their radiation inherits the symmetry of the crystal (see Section 2.4). Exciton-phonon interactions can, however, modify these optical selection rules. Here, we used Raman spectroscopy to study the temperature dependence of exciton-phonon coupling in MoS₂. Additionally, Raman selection rules were studied at room and cryogenic temperatures for nonresonant and near-resonant excitation with respect to the fundamental exciton. In the following, we limit our discussion to ML spectra and therefore use the ML mode notations at the Γ point of the BZ, $A_{1g} \rightarrow A_1'$ and $E_{2g}^1 \rightarrow E'$.

Fig. 4.3a shows the evolution of Raman spectra for a MoS₂ ML from cryogenic to room temperature at near-resonant excitation. The mode intensities of E', A₁', and the silicon (Si) line of the substrate are plotted in Fig. 4.3b for reference. The sharp intensity decrease of MoS₂ related Raman modes for temperatures above ~ 30 K, that was accompanied by a redshift of the X resonance (Fig. 4.3c), is attributed to the nonlinear dependence of the scattering probability on the exciton-laser detuning [114, 115] (see Eq. 2.17). From the data we extract an intensity change of about 13.5% (12.4%) for 1 meV decrease (increase) of the exciton-laser detuning at 3 K. In contrast, the silicon line exhibited less pronounced sensitivity.

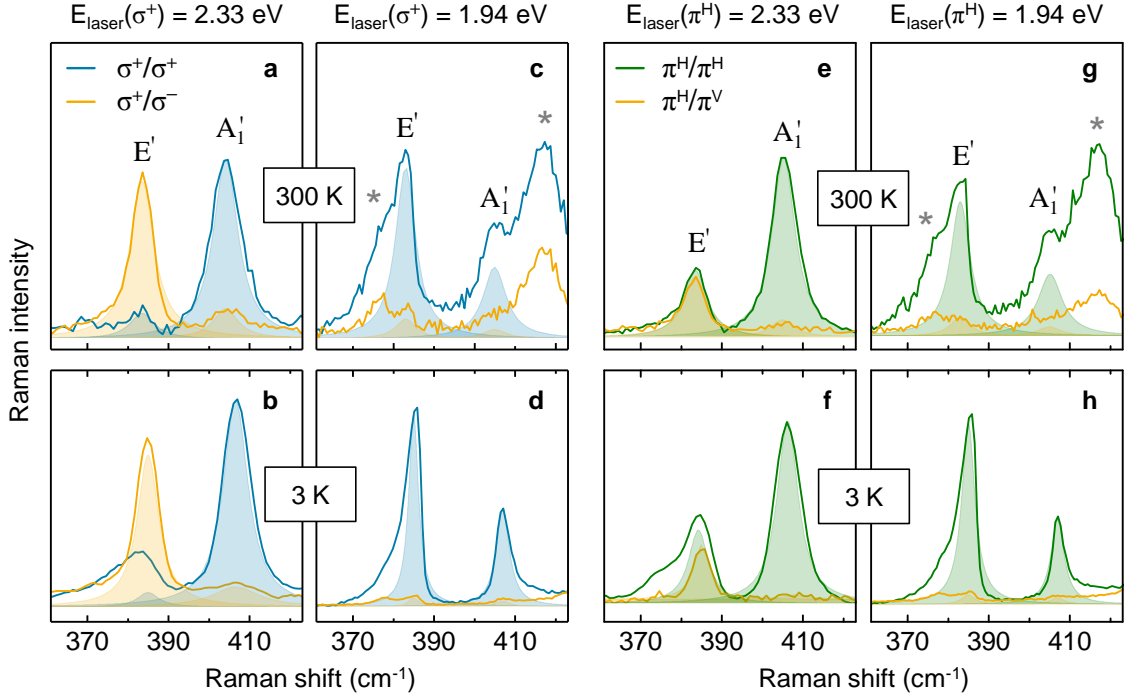


Figure 4.4: Polarization analysis of MoS₂ monolayer A₁' and E' Raman modes under circularly and linearly polarized excitation. **a**, Room-temperature (300 K) and **b**, cryogenic-temperature (3 K) spectra in co- and cross-circularly polarized analysis (σ^+/σ^+ , blue and σ^+/σ^- , yellow) for nonresonant excitation at $E_{\text{laser}}(\sigma^+) = 2.33$ eV. **c** and **d**, Same as **a** and **b** but for near-resonant excitation at $E_{\text{laser}}(\sigma^+) = 1.94$ eV. **e–h**, Analogous set of Raman spectra as in **a–d** but for linear excitation with co- and cross-linearly polarized analysis (π^H/π^H , green and π^H/π^V , yellow). Note the polarization change of the E' mode, which follows the laser polarization for near-resonant excitation in the limit of Fröhlich interactions. The filled Lorentzian distributions are model fits of A₁' and E', where contributions from the E_{1u}² mode (378 cm⁻¹) and the dispersive 'b' mode (418 cm⁻¹) were taken into account (both labeled with a gray star).

An increasing variation of the exciton-laser detuning will first reduce the Raman scattering intensity (Fig. 4.3) and for larger detunings, the optical selection rules of Raman modes can be modified. As such, for nonresonant excitation (2.33 eV) the E' and A₁' modes of ML MoS₂ exhibited polarization properties dictated by the D_{3h} symmetry of the crystal. This is shown in Figs. 4.4a (4.4b) and 4.4e (4.4f) for circularly and linearly polarized excitation, at 300 K (3 K), respectively. The E' mode showed cross-polarized response for circularly polarized excitation (yellow traces in Figs. 4.4a and 4.4b), while A₁' showed higher intensity for co-circularly polarized detection (blue traces). For nonresonant linearly polarized excitation (Figs. 4.4e

and 4.4f), unpolarized scattering was observed for E', whereas A'₁ was co-linearly polarized (green traces).

As opposed to nonresonant excitation, for excitation on the blue shoulder of X at 1.94 eV we observed symmetry-forbidden Raman scattering of E' phonons due to impurity-enhanced Fröhlich interactions (see Section 2.4 and Ref. P2). Figs. 4.4c (4.4d) and 4.4g (4.4h) show pronounced co-polarized scattering of A'₁ and E' Raman mode intensities at 300 K (3 K) for excitation in the circular and linear bases. For clarity, the scattered intensities of A'₁ and E' in Fig. 4.4 are indicated by filled Lorentzians obtained from model fits that correct for contributions from the E²_{1u} mode at 378 cm⁻¹ and the dispersive 'b' mode at 418 cm⁻¹. These modes become dominant for near-resonant excitation at room temperature due to a significant decrease of E' and A'₁ Raman mode intensities (see Fig. 4.3).

4.4 Magneto-Raman imaging of mode intensities in monolayer MoS₂

In this section spatially mapped Raman mode intensities of ML MoS₂ at cryogenic temperatures and magnetic fields perpendicular to the crystal surface were used to study the influence of excitons at different crystal sites on phonon scattering processes. The data presented here were obtained using excitation resonant with the blue shoulder of the fundamental exciton X.

Fig. 4.5a shows an optical image of an MoS₂ ML polycrystal grown by CVD and transferred onto Si/SiO₂ (see Ref. P7 for sample preparation). The star-shaped geometry of the flake corresponds to a cluster of single-crystal domains separated by grain boundaries [41, 42]. At these linear defects, the PL intensity of the fundamental exciton (X) was enhanced as shown in the raster-scan map of Fig. 4.5b. The single crystal areas between the grain boundaries exhibited weaker and spatially homogeneous intensity distributions. Variations in the optical properties of the crystal were also observed with Raman spectroscopy. We employed polarization-resolved Raman intensity mapping of the E¹_{2g} and A_{1g} modes (Figs. 4.5c and 4.5d) to probe exciton-phonon interactions [116]. The measurements were performed with co-circularly σ^+ polarized excitation and detection. While the A_{1g} mode exhibited co-polarized scattering according to the lattice symmetry, Fröhlich interactions enhanced co-polarized forbidden scattering of the E¹_{2g} mode (see Section 4.3). The MoS₂ crystal exhibited comparable intensity distributions for the two modes that deviated significantly from the exciton PL map, particularly around grain boundaries. In these areas enhanced Raman intensities for E¹_{2g} and less so for A_{1g} were

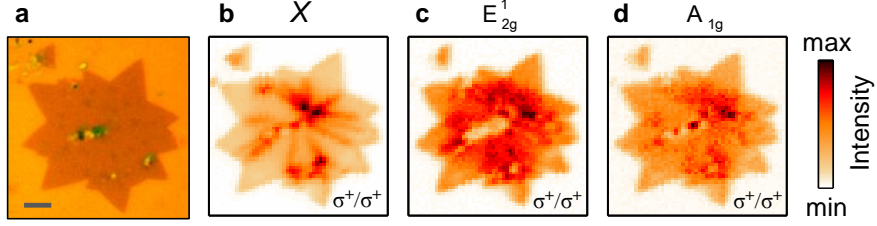


Figure 4.5: **a**, Optical image of a monolayer MoS₂ polycrystal grown by chemical vapor deposition and transferred onto Si/SiO₂; scale bar is 5 μm . **b**, **c**, and **d**, Raster-scan maps of the ground-state exciton (X) photoluminescence intensity, and the E_{2g}^1 and A_{1g} Raman mode intensities, respectively. The data were recorded at 3 K with a near-resonant (1.95 eV) circularly polarized laser and co-circularly polarized detection (σ^+/σ^+). Note that the grain boundaries of the flake are visible in **b** as red-colored regions.

possibly induced by local strain [41], with stronger coupling to in-plane than to out-of plane vibrations [52, 53, 117, 118].

As discussed previously, exciton-resonant excitation of a Raman process strongly influences the scattered intensity. In general, a Raman process can be enhanced if the initial photon, the scattered photon, or both are in resonance with an intermediate exciton state [95]. To tune the resonance condition of Raman scattering through the excitonic valley Zeeman effect, we applied a magnetic field in Faraday geometry to the sample. Figs. 4.6b and 4.6c show co-polarized intensity differences between right-handed and left-handed circularly polarized excitation (σ^+ and σ^-), normalized to their total intensity, of the E_{2g}^1 and A_{1g} modes at 9 T. At the same time, circularly polarized excitation also selectively generated either K (σ^+) or K' (σ^-) valley Zeeman split excitons (Fig. 4.6d). While green-colored ML areas are dominated by scattered radiation that is co-polarized in the σ^- basis, orange-colored domains occurring mainly at grain boundaries exhibited preferential scattering in the σ^+ basis. In the presence of a positive out-of-plane magnetic field, X excitons at K' are shifted to higher energies [77] and therefore reduce the separation to a blueshifted excitation laser (Fig. 4.6d). From temperature-dependent measurements (Fig. 4.3), we estimate an average Raman intensity change of 13% for a 1 meV decrease (increase) of the K'-valley (K-valley) exciton-laser detuning at 9 T and 3 K [119]. This agrees reasonably well with green-colored areas away from the edges (Figs. 4.6b and 4.6c) with an intensity enhancement of 5–12% for Raman scattering in the σ^- basis. Deviations from the expected changes to enhancements of about 27% at crystal edges (dark green) as well as pronounced scattering in the σ^+ basis for regions around grain boundaries (orange), however, escape our current understanding.

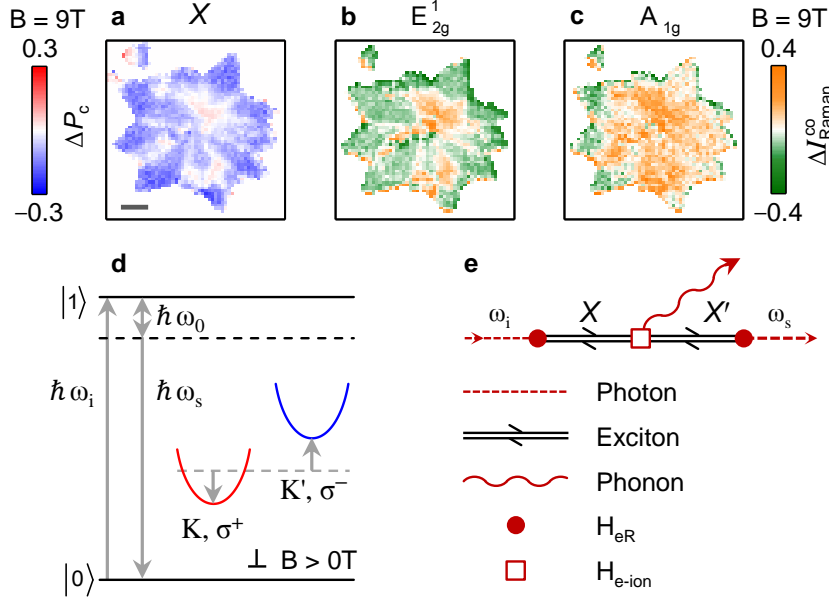


Figure 4.6: **a**, Changes in the degree of circular polarization (P_c) for the ground-state exciton (X) at 9 T and 3 K. The data was computed as the difference $\Delta P_c = P_c(\sigma^+) - P_c(\sigma^-)$ between measurements in the σ^+ and σ^- bases, scale bar is $5\ \mu\text{m}$. **b** and **c**, Maps of normalized differences $\Delta I_{\text{Raman}}^{\text{co}} = (I^{\sigma^+/\sigma^+} - I^{\sigma^-/\sigma^-}) / (I^{\sigma^+/\sigma^+} + I^{\sigma^-/\sigma^-})$ between σ^+ and σ^- polarized intensities for the E_{2g}^1 mode and the A_{1g} mode, measured with co-polarized excitation at 9 T and 3 K. **d**, Schematic of the Stokes Raman scattering process in monolayer MoS₂ with the crystal vacuum state $|0\rangle$ and an excited exciton state $|1\rangle$. Initial (scattered) laser photon energies are indicated by arrows and labeled with $\hbar\omega_i$ ($\hbar\omega_s$). Note the reduced energy of $\hbar\omega_s$ by $\hbar\omega_0$ with respect to $\hbar\omega_i$ due to phonon emission. A positive external magnetic field applied perpendicular to the layer surface lifts (reduces) the exciton ground state in the K' valley (K valley) and modifies the resonance condition of the Raman process. **e**, Feynman diagram of the one-phonon Stokes scattering process with phonon-exciton interaction, reproduced from Ref. 95. The frequencies of the initial and scattered photons are denoted by ω_i and ω_s ; X and X' are the excited and transformed virtual exciton states, respectively. The filled sphere marks the electron-radiation interaction Hamiltonian \mathcal{H}_{eR} and the open square denotes the electron-phonon interaction Hamiltonian \mathcal{H}_{e-ion} .

An out-of-plane magnetic field also changes the crystal symmetry of a ML from D_{3h} to C_{3h} and additionally modifies the Raman tensor \mathcal{R} through the field dependence of the second-order electron susceptibility $\alpha(B)$ [120]. These effects influence the lattice contribution to the Raman scattering intensity and conserve the Raman selection rules. Our observations of differences between intensities excited with opposite circular polarization (Figs. 4.6b and Fig. 4.6c) are therefore not explained by the magnetic-field dependence of the lattice contribution to the Raman tensor.

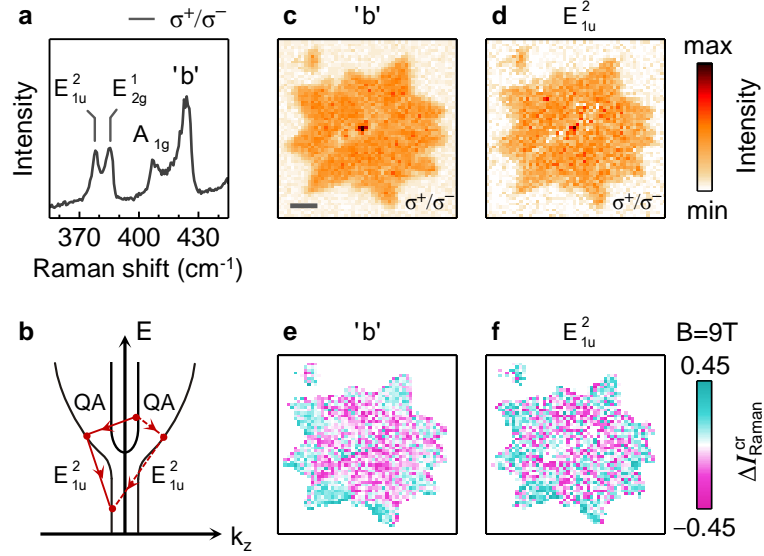


Figure 4.7: **a**, Raman spectrum of a MoS₂ monolayer under near-resonant circularly polarized excitation and cross-polarized detection (σ^+/σ^-) with the E_{1u}^2 mode at 378 cm⁻¹ and the dispersive 'b' mode at 424 cm⁻¹. **b**, Schematic of the 'b' mode scattering process, where an exciton-polariton scatters a longitudinal quasi-acoustic (QA) and an E_{1u}^2 phonon as proposed by Sekine et al. [121]. **c** and **d**, Raster-scan intensity maps of the 'b' and E_{1u}^2 Raman modes, respectively, with the same excitation and detection polarization as in **a** (σ^+/σ^-). **e** and **f**, 'b' and E_{1u}^2 Raman mode maps showing normalized intensity differences $\Delta I_{\text{Raman}}^{\text{cr}} = (I^{\sigma^+/\sigma^-} - I^{\sigma^-/\sigma^+}) / (I^{\sigma^+/\sigma^-} + I^{\sigma^-/\sigma^+})$ between σ^+ and σ^- polarized excitation with cross-polarized detection at 9 T. Note the similarities in color contrast among the two maps. All data were recorded at 3 K and with a laser at 1.95 eV.

Hence, we speculate that Raman scattering in our samples was influenced by the magnetic field dependence of exciton-phonon interactions in the Fröhlich limit (Fig. 4.6e). Fig. 4.6a shows a map of differences in P_c between σ^+ and σ^- polarized excitation at 9 T for X excitons. The blue domains at regular ML positions in Fig. 4.6a exhibited higher valley polarization at K', whereas light red areas around grain boundaries showed mainly K-valley polarization. The intensity distribution was remarkably similar to the pattern obtained for the map of the E_{2g}^1 mode (Fig. 4.6b). Our findings suggest that studies of exciton-phonon interactions in external magnetic fields may provide new insights into excitonic valley phenomena of TMD crystals.

Finally, we address two additional Raman modes. Figure 4.7a shows a representative Raman spectrum from a regular ML position for circularly polarized excitation and cross-polarized detection (σ^+/σ^-). With this polarization configuration, the E_{1u}^2 at 378 cm⁻¹ and the dispersive 'b' mode at 424 cm⁻¹ were most pronounced.

Sekine et al. [121] predicted that the two modes are correlated, as the 'b' mode results from two-phonon scattering of an exciton-polariton by a longitudinal quasi-acoustic (QA) phonon and an E_{1u}^2 phonon (Fig. 4.7b). The dependence of the 'b' mode on temperature, pressure, and the excitation energy have been used to study the electronic band structure and the role of intermediate exciton states [114]. In the following, we present indications for the involvement of E_{1u}^2 phonons in the proposed scattering mechanism of the 'b' mode.

Figs. 4.7c and 4.7d show intensity landscapes of the 'b' and E_{1u}^2 modes, respectively. Both modes exhibited spatially uniform intensity distributions at regular ML regions (note that the enhanced intensity at the center stems from a multilayer). However, at grain boundaries the intensities were reduced in the polarization configuration that maximized scattering in regular ML regions. This observation stands in contrast to the maps for the E_{2g}^1 and A_{1g} modes (Figs. 4.5c and 4.5d). The similar intensity distributions of the 'b' and E_{1u}^2 modes speak in favor of the scattering process proposed by Sekine et al.

A peculiar characteristic of the 'b' mode intensity is that it exhibits enhancement only if the scattered photon ($\hbar\omega_s$ in Fig. 4.6d) is in resonance with an intermediate exciton state [121]. We study this condition for the 'b' and the related E_{1u}^2 mode by analyzing normalized intensity differences between σ^+ and σ^- polarized excitation with cross-polarized detection $(I^{\sigma^+/\sigma^-} - I^{\sigma^-/\sigma^+}) / (I^{\sigma^+/\sigma^-} + I^{\sigma^-/\sigma^+})$ in a magnetic field of 9 T (Figs. 4.7e and 4.7f). If comparable Raman enhancement due to the incident and scattered resonances is assumed, the maps would show no contrast. This was not the case at regular crystal positions (cyan domains in Figs. 4.7e and 4.7f), where both modes exhibited intensity enhancement for scattered photons with σ^- polarization (I^{σ^+/σ^-} is larger than I^{σ^-/σ^+}). At these regions, the average changes of $10 \pm 1\%$ for the 'b' mode and $14 \pm 2\%$ for the E_{1u}^2 mode of their normalized intensity differences, however, exceeded the estimated enhancement of 5% for the outgoing resonance condition (obtained from the data of Fig. 4.3). Similar to our previous observations for the E_{2g}^1 and A_{1g} modes (Figs. 4.6b and 4.6c), areas around grain boundaries showed reversed patterns which are not explained by the resonance condition. Despite this, we emphasize that our measurements away from defects suggest that the E_{1u}^2 mode, just like the 'b' mode, exhibits intensity enhancement for exciton-resonant scattered photons.

4.5 Conclusions

In summary, we studied optical generation and detection of K- and K'-valley excitons in CVD-grown MoS_2 MLs. The valley degree of freedom was susceptible to exciton localization and trion formation. Furthermore, we identified pronounced exciton-

phonon interactions that modify Raman selection rules of LO phonons. The signal of Raman mode intensities was most pronounced at cryogenic temperatures and exhibited spatial inhomogeneities for excitation resonant with band-edge excitons. At regular crystal positions, a perpendicular magnetic field enabled tuning of Raman intensities in accord with the resonance to valley Zeeman split excitons. Finally, our data signifies a connection of the E_{1u}^2 Raman mode to the two-phonon scattering of the 'b' mode for ML MoS₂ with similar intensity enhancement with respect to the outgoing resonance.

Chapter 5

Momentum-dark excitons in monolayer semiconductors

THIS CHAPTER IS BASED ON THE MANUSCRIPT [P4](#):

J. Lindlau, R. Cedric, V. Funk, J. Förste, M. Förg, L. Colombier, A. Neumann, E. Courtade, S. Shree, M. Manca, T. Taniguchi, K. Watanabe, M.M. Glazov, X. Marie, B. Urbaszek, and A. Högele. *Identifying optical signatures of momentum-dark excitons in monolayer transition metal dichalcogenides*. ArXiv e-prints (2017). [arXiv:1710.00988](#).

TMD monolayers exhibit rich photoluminescence spectra associated with interband optical transitions of direct-gap semiconductors. Upon absorption of photons, direct excitons with zero center-of-mass momentum are formed by photoexcited electrons in the conduction band and the respective unoccupied states in the valence band of the same valley. The corresponding spectral signatures, however, are insufficient to explain the main characteristic peaks observed in the photoluminescence spectra of monolayer TMDs on the basis of momentum-direct band-edge excitons alone. In this chapter, we present a model including momentum-indirect excitons for the understanding of the versatile photoluminescence features. Taking into account phonon-assisted radiative recombination pathways for electrons and holes from dissimilar valleys, we interpret unidentified peaks in the emission spectra as acoustic and optical phonon sidebands of momentum-dark excitons. Our approach represents a crucial step towards a unified understanding of TMD photophysics and will facilitate the interpretation of optical, valley, and spin phenomena in TMDs arising from bright and dark exciton manifolds.

5.1 Introduction

While early PL spectroscopy studies have established elementary signatures of bright excitons in neutral [56–58] and charged TMD MLs [59, 60, 122], the emission from spin-forbidden excitons has been identified only recently [7, 10–14]. The observations of lowest-lying momentum-bright yet spin-forbidden states in tungsten dichalcogenide MLs explain some of the differences between the rich structure in the PL spectra of tungsten-based MLs and the rather simple one- or two-peak PL of ML molybdenum dichalcogenides [123]. Some of the main PL peaks that can be more intense than the bright exciton, however, have escaped unambiguous assignment and are thus commonly attributed to defect-localized excitons. Recently, the peaks with energy close to the trion energy were alternatively attributed to excitons bound to localized charges [124]. Moreover, unequivocal deconvolution of individual PL contributions from neutral and charged excitons has been compromised by the lack of control over the charge doping level in most samples and impeded further by the conspiracy of similar energy scales of optical phonons [61, 62] and trion binding energies [23, 60, 125]. In the following, we discuss a unifying explanation for unidentified PL features in the spectra of TMD MLs by expanding the realm of momentum-direct excitons with their momentum-indirect counterparts. This analysis benefits from the greatly improved optical quality of TMD MLs encapsulated in hexagonal boron nitride (hBN) [13, 123, 126–128] in charge-tunable structures.

5.2 Spectral decomposition of monolayer photoluminescence

As initially proposed by Dery and Song for combinations of electrons in K with empty VB states in K' in tungsten-based MLs [62], the rich PL spectra of TMD MLs are interpreted in the following by including indirect transitions associated with electrons and holes in dissimilar valleys [62, 86, 129–131] (see Section 2.1 and Fig 2.2). To this end, excitons are constructed by forming an empty state in the upper valence subband at the K valley and the Coulomb-correlated electron at the K' or, alternatively, at one of the Q points. Note that the hole state is formally associated with the time-reversal of the unoccupied state in the VB [85]. Neglecting the upper subband at the Q points due to sizable spin-orbit splittings of the order of 100 meV [19] and omitting electron-hole exchange for simplicity (energy scale of a few meV), the exciton spectrum is obtained as shown schematically in Fig. 5.1a. Two zero-momentum configurations with both electron and hole at K correspond to the well studied spin-allowed and spin-forbidden exciton (X and D) [10–12, 14, 84, 129].

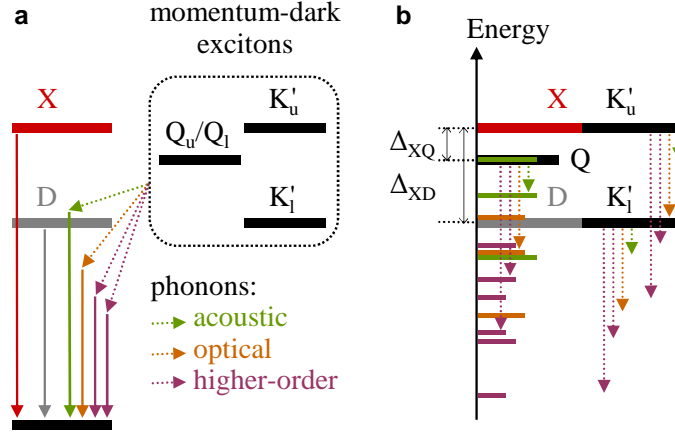


Figure 5.1: Basic concepts for the spectral decomposition of photoluminescence from monolayer transition metal dichalcogenides of direct and phonon-assisted radiative processes. **a** and **b**, Construction of a conceptual photoluminescence spectrum as the sum of the zero-phonon lines of X and D excitons (red and gray bars) and the phonon sidebands of momentum-dark excitons (colored bars). The energy position of the latter (black bars) can be reconstructed from their respective phonon replicas (green and orange bars) by considering in-plane transverse acoustic (TA) and longitudinal acoustic (LA) phonons as well as in-plane TO(E'), LO(E'), and out-of-plane A₁ optical phonon modes, and sidebands resulting from higher-order decay processes (purple bars) assisted by combinations of multiple phonons.

In addition to direct excitons, also excitons with finite center-of-mass momenta can be constructed from electrons in valleys other than the unoccupied state in K. They do not recombine directly via photon emission but require the assistance of acoustic or optical phonons. These momentum-dark excitons are labeled with capital letters denoting the electron valley with the subscript l (u) for spin-like (spin-unlike) configurations of the electron and hole spins (in electron spin notation). By neglecting electron-hole exchange, two pairs of degenerate states with electrons and holes in K (D and K'_l as well as X and K'_u), and degenerate spin-like and spin-unlike Q-excitons with electrons in six inequivalent Q pockets are obtained. The energetic ordering in Fig. 5.1a corresponds to tungsten-based MLs. In the presence of time-reversal symmetry, all states have their counterparts with the unoccupied state at the K' valley and reversed spin orientation.

As the manifold of momentum-dark excitons, shown encaged in Fig. 5.1a, has no dipolar radiative pathways due to momentum conservation constraints, the states do not appear directly in PL or reflection spectroscopy. However, in analogy to indirect band-gap bulk semiconductors such as silicon [132] or hBN [133], finite-momentum excitons can decay radiatively via simultaneous emission of phonons.

Such decay channels, indicated schematically in Figs. 5.1a and 5.1b by colored arrows and enabled by acoustic and optical phonons as well as higher-order combinations of multiphonon processes, will give rise to phonon replicas of momentum-dark excitons in the PL emission. Once the energy positions of all states are determined from spectral decomposition, the splittings Δ_{XD} and Δ_{XQ} are obtained as indicated in Fig. 5.1b.

5.2.1 Analysis of MoSe₂ emission

First, the analysis is applied to ML MoSe₂ encapsulated in hBN with active doping control. The cryogenic PL spectrum shown in Fig. 5.2a features two bright PL peaks, commonly attributed to the emission from neutral and charged excitons. In high signal-to-noise DR measurements in the gated structure, however, no trion signature was detected in addition to the solitary resonance of the neutral exciton (Fig. 5.2b) in contrast to doped samples [134]. Therefore, the intensive PL peak ~ 30 meV below X could also be interpreted as an optical phonon sideband of the momentum-dark exciton state K'_u that is set resonant with the bright exciton by neglecting electron-hole exchange. The respective acoustic sidebands would then contribute weak yet finite PL in between the two intensive peaks.

To obtain a model fit of the neutral ML MoSe₂ spectrum in the framework of this analysis shown by the red solid line in Fig. 5.2a, the ZPLs of resonant momentum-bright and momentum-dark states X and K'_u were modeled by homogeneously broadened Lorentzians with the joint FWHM linewidths γ_X and γ_M . Moreover, the phonon replicas of K'_u were restricted to first-order processes. By taking the corresponding phonon modes calculated in Ref. 61 (recapitulated in Table 5.1 for convenience) with explicit phonon energies of 16.6 and 19.9 meV for the TA and LA acoustic phonons, and 35.5, 37.4, and 25.6 meV for TO(E'), LO(E'), and A₁ optical phonons available for the scattering of the electron from the K' into the K valley, the fitting procedure determined the best-fit energy position (indicated by the dashed line) and linewidth $\gamma_X = 2.3$ meV for the ZPL of X and thus of K'_u .

Remarkably, the correspondence between the spectrum and the model fit in Fig. 5.2a was obtained with vanishing contributions from TO and LO phonons, and thus the lower-energy peak can be ascribed entirely to the A₁ optical sideband of K'_u . For phonon replicas to be as intense in emission as the bright exciton emission in the PL of neutral ML MoSe₂, long-lived population of dark states without efficient decay channels must be present. Such population can be provided by the reservoir of momentum-dark K'_u excitons, or by momentum-dark Q states if the value of 28 meV [61] instead of the much higher prediction of 137 meV [19] is anticipated for the splitting Δ_{KQ} in ML MoSe₂.

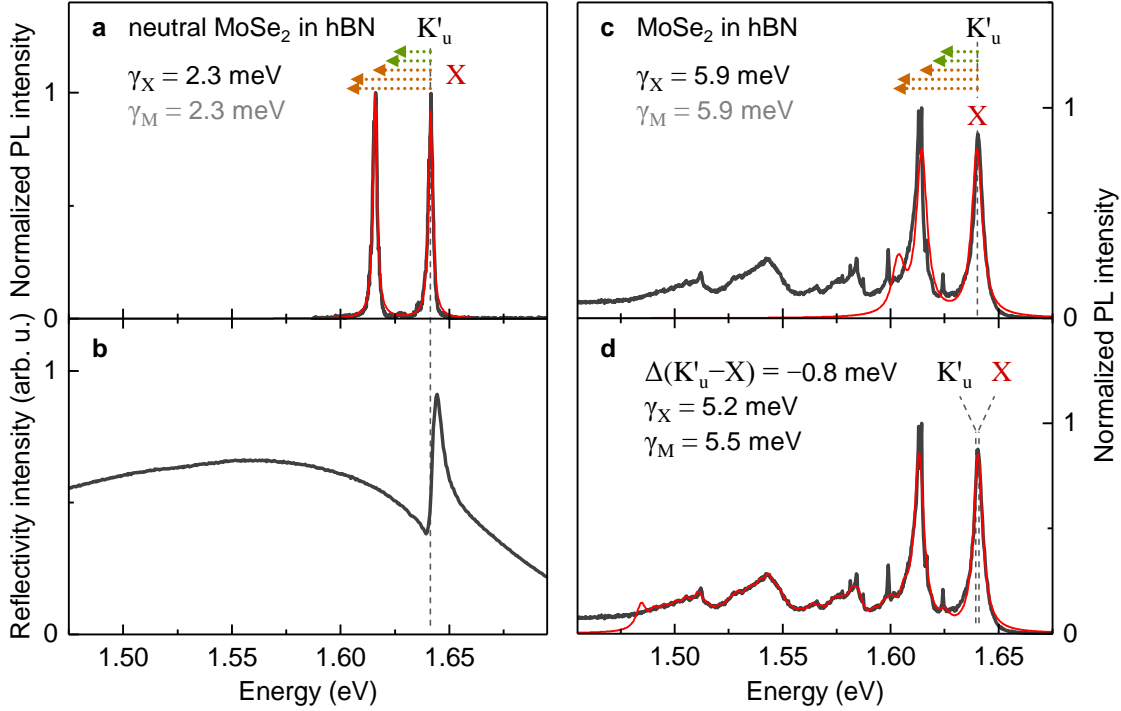


Figure 5.2: **a**, Spectral decomposition of cryogenic photoluminescence from monolayer MoSe₂. Basic model fit (red solid line) with first-order phonon replicas of momentum-dark K'_u excitons resonant with the bright exciton state X in the absence of electron-hole exchange. The best-fit energy position indicated by the dashed line was obtained with γ_X as fit parameter and γ_M set identical to γ_X . The green and orange arrows indicate phonon sidebands of momentum-dark excitons associated with acoustic and optical phonons with respective energies taken from Ref. 61. **b**, Corresponding reflectivity at gate voltage of +10 V. Note the absence of trion-related features. **c**, Same as **a** but for a monolayer MoSe₂ without active control of charge doping. **d**, Refined model fit (red solid line) with variable energy positions and linewidths of X and K'_u states and up to fourth-order phonon replicas with variable phonon energies bound by ± 2 meV around the values of Ref. 61. Free (fixed) fit parameters are given in the legends in black (gray).

The same analysis was also applied to ML MoSe₂ encapsulated in hBN without active doping control. As in Fig. 5.2a, the PL spectrum in Fig. 5.2c features two bright PL peaks. In addition, the PL exhibits an extended red wing with some structure commonly ascribed to localized excitons in potentials of unintentional disorder [135]. Again, it is assumed that the intensive PL peak ~ 30 meV below X is not related to trions but is instead composed of optical phonon sidebands of the momentum-dark exciton state K'_u resonant with the bright exciton in the absence of electron-hole exchange.

Mode	MoSe ₂			WS ₂			WSe ₂		
	Γ	K	Q	Γ	K	Q	Γ	K	Q
TA	0	16.6	13.3	0	17.4	15.9	0	15.6	11.6
LA	0	19.9	16.9	0	23.6	19.5	0	18.0	14.3
TO(E')	36.1	35.5	36.4	44.4	43.8	45.3	30.5	26.7	27.3
LO(E')	36.6	37.4	37.5	44.2	43.2	42.3	30.8	31.5	32.5
A ₁	30.3	25.6	27.1	51.8	48.0	50.0	30.8	31.0	30.4

Table 5.1: Phonon mode energies at the high-symmetry points of the first Brillouin zone for monolayer MoSe₂, WS₂, and WSe₂ used in the model fits. Higher-order scattering processes with phonon energies equal to the energy of LO(E') within 1 meV (listed in the table in gray) were discarded from our analysis for simplicity. All energies are given in meV and reproduced from Ref. 61.

The model fit to the ML MoSe₂ spectrum of Fig. 5.2c was obtained with ZPLs of momentum-bright and momentum-dark excitons modeled by homogeneously broadened Lorentzians at the same energy and with the same FWHM linewidth γ_X . Analogous to Fig. 5.2a, first-order scattering processes by acoustic and optical phonons with energies from Ref. 61 yield the two peaks as the main PL features with $\gamma_X = 5.9$ meV and best-fit energy positions indicated by the dashed lines.

To improve the fit up to the striking correspondence with the spectrum in Fig. 5.2d, the phonon energies were allowed to vary by ± 2 meV around their theoretical values. Such small variation of phonon energies account for sample-to-sample variations in the dielectric environment or strain and are well within the range of quantitative observations with Raman spectroscopy [136]. Moreover, phonon processes of up to fourth order were included (the cutoff to the model spectrum around 1.48 eV is because processes beyond fourth order were truncated), and the energy positions and the linewidths were allowed to vary for both X and K'_u states. Remarkably, all intricate features of the PL spectrum are well reproduced by the model fit without significant changes to the ZPL energies and linewidths, and with higher-order phonon processes improving the correspondence between the fit and the intricate spectral details of the extended red tail of the PL spectrum. The bright peak below X is interpreted as composed of optical phonon sidebands of the momentum-dark state K'_u that also gives rise to broad lower-energy PL peaks via its higher-order phonon replicas. In contrast, the emission from disorder-localized excitons [48], characterized by narrow spectral features in Fig. 5.2d, is not captured by the present model.

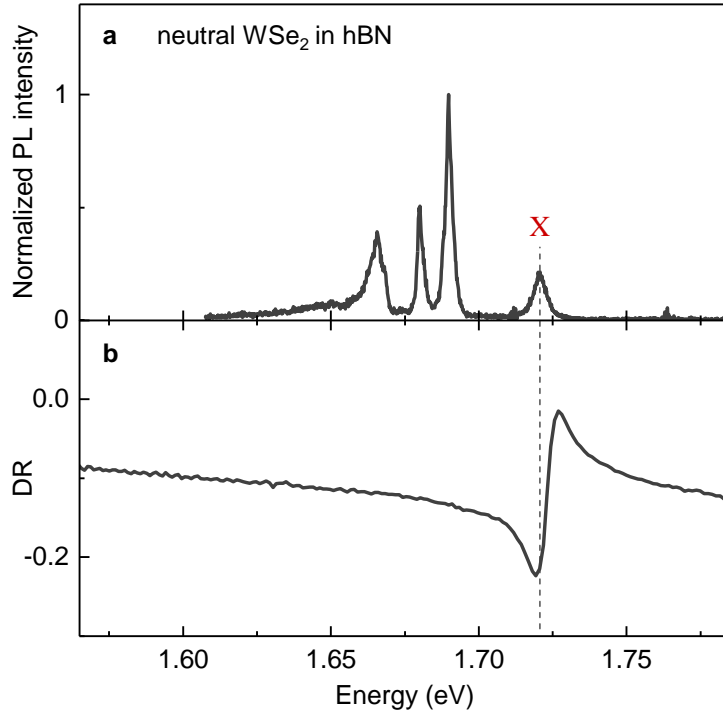


Figure 5.3: **a**, Photoluminescence spectrum of a neutral monolayer WSe_2 **b**, Corresponding differential reflectivity. Note the absence of trion-related features.

5.2.2 Analysis of WSe_2 and WS_2 emission

The analysis of the simple MoSe_2 emission has served as an illustration of the possible involvement of phonon-assisted recombination of momentum-dark excitons. In the next step the decomposition analysis was applied to ML WSe_2 with a rich spectrum of unidentified peaks [23] as in Fig. 5.3a (reproduced in Fig. 5.4a) recorded on ML WSe_2 encapsulated in hBN and tuned to the point of charge neutrality [137]. It features narrow spectral lines characteristic of high-quality MLs with PL close to the homogeneous limit [14, 123, 127] and a negligible contribution from trions was assumed, again based on the absence of a trion resonance in high signal-to-noise DR (see Fig. 5.3b). As discussed previously, the PL signatures of ML WSe_2 in Fig. 5.4a differ significantly from the PL of ML MoSe_2 in Fig. 5.2 because of the reversed ordering of spin-polarized subbands in tungsten and molybdenum dichalcogenides. To model the PL spectrum of WSe_2 , one has to include the spin-forbidden exciton state D redshifted by 40 meV from the ZPL of the bright state X in this specific sample [14, 137]. In order to obtain the best model fit shown as the red solid line in Fig. 5.4a, not only the phonon energies were allowed to vary around the values given for ML WSe_2 in Ref. 61 but also the energies and linewidths of the Lorentzian ZPLs

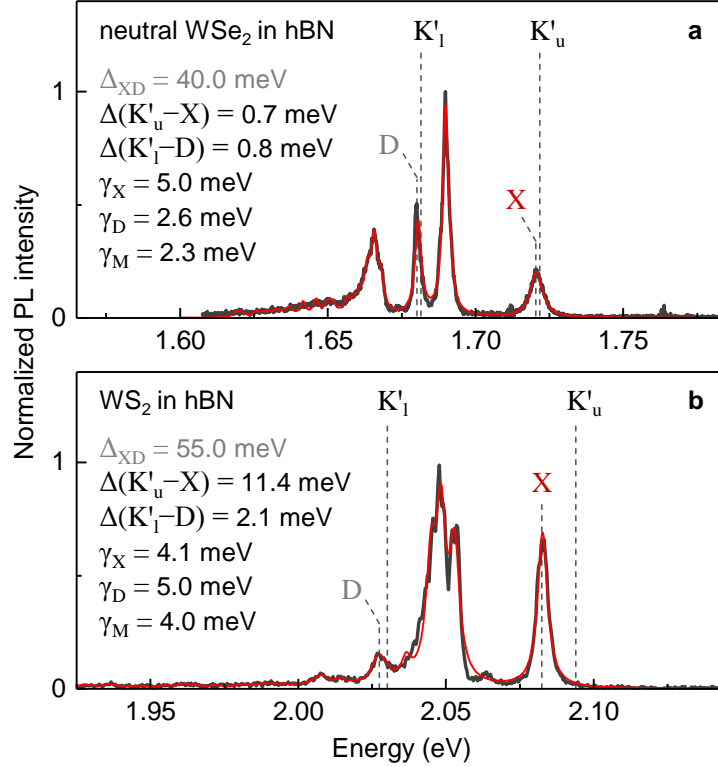


Figure 5.4: Spectral decomposition of cryogenic photoluminescence from monolayer WSe₂ and WS₂. **a**, Refined model fit (red solid line) to the spectrum of neutral monolayer WSe₂ including momentum-dark state K'₁ resonant with D at a fixed bright-dark splitting $\Delta_{XD} = 40$ meV and all other parameters determined from the best fit. **b**, Same for monolayer WS₂ without active charge control. Free (fixed) fit parameters are given in the legends in black (gray).

of D, K'₁, K'_u, and X states. Assuming similar timescales for phonon-assisted decay and transform-limited broadening of momentum-dark states, a joint linewidth γ_M was used for K'₁ and K'_u.

The best-fit model spectrum of Fig. 5.4a with up to third-order processes was obtained with $\gamma_X = 5.0$ meV and comparable linewidths of ~ 2.5 meV for both spin-forbidden and momentum-dark states at the respective energy positions of the ZPLs indicated by the dashed lines. The overall correspondence between the measured spectrum and the model is again compelling. It interprets the bright-most peak in between the bright and dark exciton ZPLs as composed of optical phonon replicas of the momentum-dark state K'_u, and the peak below D as acoustic sidebands of K'₁. Again, the peak 32 meV below the bright exciton is not attributed to trion emission for two reasons: First, the gated sample shows only one solitary resonance of the neutral exciton without additional trion features in DR. Second, this sample tuned

into the n -type regime exhibits a pronounced fine-structure splitting both in PL and reflectivity as a hallmark of negative trions (see Ref. 137). Without the ambiguity of unintentional doping, the electron-hole exchange splittings $\Delta(K'_u - X)$ and $\Delta(K'_1 - D)$ are of the order of a few meV.

The analogous spectral decomposition was also carried out for ML WS_2 sandwiched in hBN without means of field-effect charge control. The best fit to the PL spectrum of Fig. 5.4b was obtained according to the refined fitting procedure used for ML WSe_2 in Fig. 5.4a with a fixed bright-dark splitting of 55 meV derived from experiment [14] and similar values for the linewidths of bright and dark excitons in the range of 4–5 meV. It is worth pointing out the main similarities and differences in the PL spectra for the two tungsten-based MLs. For the WS_2 spectrum, only second-order processes were required since the absolute energies are larger as compared to WSe_2 [61]. Moreover, the phonon modes exhibit larger splittings (see Table 5.1). The LA-TA splitting at the K point of WS_2 , for example, exceeds the value in WSe_2 by ~ 4 meV. More significantly, the optical phonon energies differ by ~ 15 meV and up to ~ 20 meV at the Γ and K points, respectively.

Among the similar PL signatures is the weak peak below D and the intense peak between X and D with fine structure due to the specific optical phonon spectrum of WS_2 . Akin to WSe_2 , the former and the latter are assigned to acoustic and optical phonon replicas of momentum-dark states K'_1 and K'_u , respectively. Surprisingly, the best fit suggests an exchange splitting of $\Delta(K'_u - X) = 11.4$ meV in contrast to 2.7 meV for WSe_2 in Fig. 5.4a. The fit to WS_2 PL requires a significant upshift of the state K'_u in order to optimally accommodate the optical phonon sidebands into the intense and complexly structured PL peak between X and D. This could be an artifact of the nonquantified contribution from trions in this sample, or indicate that the set of involved momentum-dark excitons could be expanded by the Q-exciton manifold as will be discussed in the next section.

5.2.3 Momentum-indirect excitons in WSe_2 and WS_2

For WSe_2 MLs the Q-momentum excitons can play an important role, since the Q valley is in close proximity to the lowest CB minimum at K according to single-particle calculations [19, 61, 73]. Excitonic corrections have been predicted to reduce the energy level of Q-excitons well below the energy of the lowest spin-forbidden state D both in WSe_2 and WS_2 MLs [130, 131, 138]. This, however, is in contradiction to the analysis developed so far that explains the lowest-energy PL peak in terms of acoustic phonon replicas of the momentum-dark reservoir K'_1 . Any deeper momentum-dark state should exhibit large population with pronounced PL phonon sidebands as in the case of BL WSe_2 with momentum-indirect band gap (see

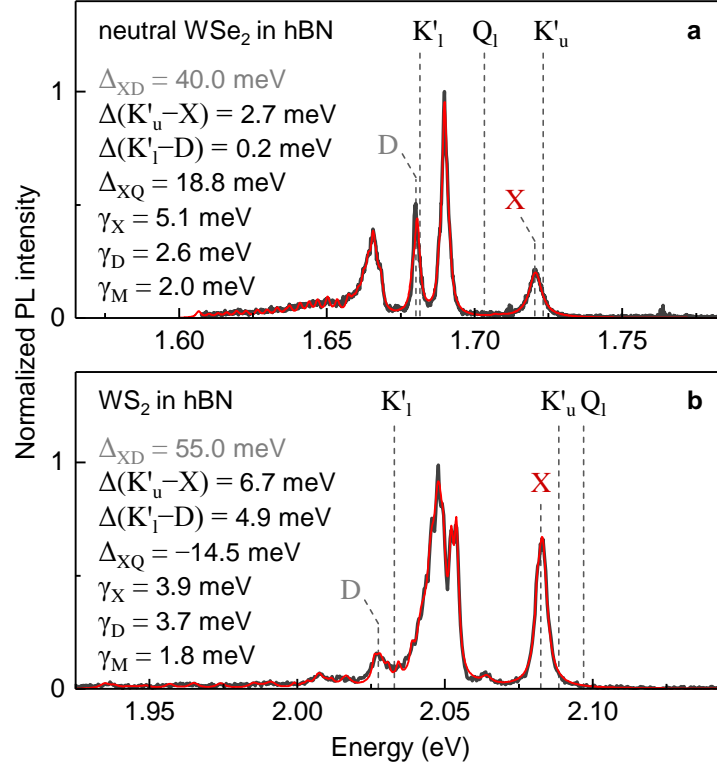


Figure 5.5: Decomposition of monolayer WSe₂ and WS₂ spectra including Q-momentum excitons. **a** and **b**, Same as Figs. 5.4a and 5.4b but with involvement of the Q-exciton manifold placed in between the states X and D in **a**, and above the state X in **b**. Free (fixed) fit parameters are given in the legends in black (gray).

Ref. P3). The only two remaining scenarios for the energy position of the Q-exciton level is in between D and X or above X (apart from placing it in resonance with K'_u or K'₁ with trivial implications).

The analysis of best fits shown in Fig. 5.5 suggests that the first scenario is better suited to model the spectrum of ML WSe₂. Note that second- and higher-order phonon-assisted processes were restricted to combinations of multiple phonons with total phonon momentum of Q or K depending on the respective initial valley of the electron. For example, the scattering of the electron from the Q valley into the K valley and subsequent emission of an optical phonon would involve an LA or TA phonon at the Q point and a zero-momentum optical phonon at the Γ point of the first BZ. With this approach to the best fit, the energy position of the Q₁ state in Fig. 5.5a is identified at $\Delta_{XQ} \simeq 19$ meV below the bright exciton with marginal variations in other fit parameters as compared to Fig. 5.4a. The corresponding energy-level hierarchy would assign the bright-most PL peak now to acoustic phonon replicas

of the Q-exciton manifold with contributions to the lowest-energy peak via optical sidebands.

In the case of ML WS₂ in Fig. 5.5b, on the other hand, the second scenario performed better. It adds an explanation to the first weak PL peak below X as an acoustic sideband of Q₁ with its respective optical sidebands merging into the most intense PL peak between X and D. Moreover, this configuration reduced the conspicuously large exchange splitting between X and K'_u found in the fit of Fig. 5.4b, and is at least qualitatively in line with theoretical calculations that predict a small separation between Q- and K-excitons in WS₂ rather than in WSe₂ MLs [138].

5.3 Conclusions

Overall, within the suggested approach good qualitative and satisfactory quantitative description of the spectra were found. Its quantitative validity is limited by the assumption of identical linewidths for all momentum-dark excitons which is not necessarily the case since different phonon-assisted pathways determine the effective lifetimes of momentum-dark excitons. Moreover, as opposed to the inclusion of both in-plane and out-of-plane optical phonon modes, the out-of-plane acoustic phonon mode ZA was discarded. The experimental precision limited by the spectral broadening even in best samples [14, 123, 127] currently provides an upper bound of a few meV on these effects.

Even with the current uncertainty in the values of exchange interaction and the energetic splittings between the valleys, the model highlights the importance of the role played by momentum-dark excitons in the elementary optical response of ML TMDs. The conclusions are fully in line with the interpretation of cryogenic spectra from BL WSe₂ [P3] and MoSe₂-WSe₂ heterostructures [P5] (Chapter 7). Based on the findings, further experimental work (Chapter 6) and more precise theoretical calculations of the single-particle band structure and phonon modes will finally consolidate a quantitative understanding of excitons in TMD MLs. Placed into a broader perspective of prevalent puzzles in TMD spectroscopy [63], the analysis provides sufficient guidelines for new interpretations.

Chapter 6

Exciton photoluminescence from monolayer tungsten diselenide

In the previous chapter a model was developed to interpret the photoluminescence of monolayer TMDs on the basis of momentum-indirect exciton transitions. Here, phonon-assisted emission of momentum-indirect excitons in monolayer WSe₂ is reexamined with comprehensive spectroscopy experiments and compared to alternative interpretations based on exciton localization. The studies include the analysis of power dependence, degree of polarization, decay dynamics, and g -factors of the low-energy excitons with controlled doping level. The data in this chapter were obtained from an electrostatically-tunable WSe₂ crystal encapsulated in hexagonal boron nitride.

6.1 Introduction

In contrast to spin-allowed lowest-energy exciton transitions in molybdenum based ML TMDs, the ground-state exciton for WS₂ and WSe₂ is spin-forbidden [7–14]. Therefore, emission spectra of ML WS₂ and WSe₂ are more complex. Apart from neutral excitons [56–58] and their charged counterparts referred to as trions [59, 60, 122], the PL signatures are complemented by emission from spin-dark excitons [7, 10–14]. The photophysics of unidentified peaks, however, remain puzzling [63]. An uncontrolled charge environment in most samples, in combination with similar scales of optical phonon [61, 62] and trion binding [23, 60, 125] energies, complicate the analysis. Unidentified spectral resonances have been attributed to defect-localized excitons [92, 139–141] and to excitons bound to localized charges at extrinsic defects in the substrate [124]. An alternative interpretation based on momentum-indirect excitons was discussed in the previous chapter. The experimental data presented in the following provides additional evidence in favor of this framework. Within a charge-controlled environment, absorption and PL measurements of an hBN-encapsulated WSe₂ ML were characterized as a function of the excitation power, lifetime, polarization, and magnetic field. The data indicate that momentum-indirect excitons are indeed the origin of unidentified peaks.

6.2 Charge-tunable reflectance and photoluminescence

The spectral signatures of excitons in ML WSe₂ undergo substantial changes upon doping. To discuss exciton specific properties, it is therefore beneficial to provide stable and well-defined charge doping. Fig. 6.1a shows the evolution of DR for an hBN-encapsulated ML WSe₂ incorporated in a field effect device. The data were measured as $(R_{\text{ML}} - R_{\text{BG}})/R_{\text{BG}}$, where R_{ML} and R_{BG} are the reflectivities on and off the ML, for gate voltages ranging from +17 V to –15 V. The false-color plot shows pronounced neutral exciton X₀ absorption at 1.72 eV for gate voltages around +14 V. For negative gate voltages, X₀ exhibited a blueshift with reduced contrast in agreement with the repulsive polaron branch of excitons coupled to a Fermi sea of electrons [122]. For simplicity, we restrict our analysis in the following discussion to doping regimes where bound trion states are formed among excitons and excess charges.

At +2 V, the Fermi energy was lifted above the lowest conduction spin-subband at K (K') as confirmed by the appearance of negatively charged trion peaks T₁ and T₂. An extra electron in the lower subband at K or K' can bind to an exciton in the K valley to form an intra- or intervalley trion. These trions exhibit a fine-structure

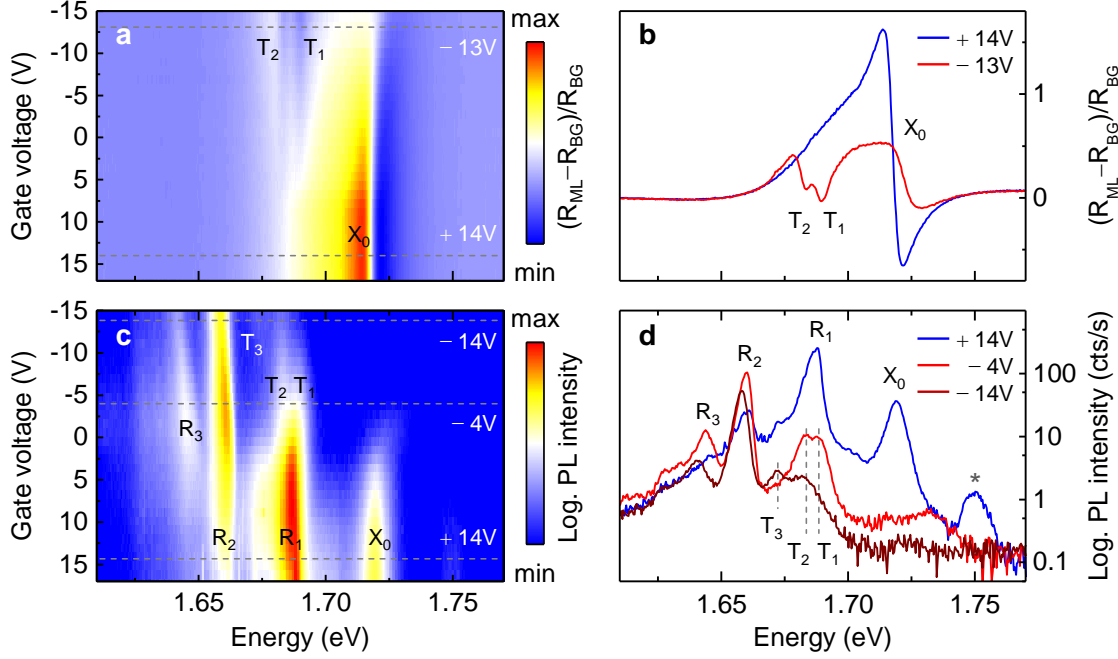


Figure 6.1: Field-effect control of reflectivity and photoluminescence for monolayer WSe_2 encapsulated in hexagonal boron nitride. **a**, Differential reflectivity evolution with gate voltage from +17 V to -15 V, measured as $(R_{\text{ML}} - R_{\text{BG}})/R_{\text{BG}}$, where R_{ML} and R_{BG} are reflectivities on and off the monolayer. The energy of the neutral exciton (X_0) exhibited a blueshift at negative gate voltages, where negatively charged trion peaks (T_1 and T_2) emerge. **b**, Differential reflectivity spectra extracted from **a** for neutral (+14 V) and electron doped (-13 V) conditions. **c**, Photoluminescence evolution for gate voltages ranging from +17 V to -15 V shown on a logarithmic color scale. The spectra feature additional peaks R_1 and R_2 at charge neutrality, and R_3 and T_3 at increasing electron concentrations. **d**, Spectra extracted from **c** for gate voltages of +14 V, -4 V, and -14 V (star marks Raman scattered photons). All data were recorded at 3.1 K. In **a** and **b** ps-pulsed white light excitation at $0.9 \mu\text{W}$ and 80 MHz repetition rate was used, in **c** and **d** a continuous-wave laser at 1.85 eV and $5 \mu\text{W}$ was employed.

splitting of 6 meV as a consequence of short-range Coulomb exchange between charge carriers in intra- and intervalley trion configurations [13, 137]. Representative DR spectra from the charge-neutral regime at +14 V (blue trace) and the electron-doped regime at -13 V (red trace) are shown in Fig. 6.1b. Note that resonances are modified by interference effects in the hBN-encapsulated heterostructure [142–144].

Complementary information was obtained from the spectrally-resolved PL evolution upon doping. Three different doping regimes can be identified from the logarithmic plot shown in Fig. 6.1c: charge neutrality at +14 V, the first electron-doped regime below -4 V with T_1 and T_2 trion emission, and a second electron-doped regime below -14 V where another peak T_3 appeared. The latter regime could be

associated with the point where the Fermi energy is lifted above the lowest conduction spin-subband at Q, providing a new reservoir of excess charges that enable formation of T_3 trions. This agrees with the analysis of the previous chapter that identified the energy of Q-excitons between the spin-dark and spin-bright excitons at K and K' . For direct comparison, spectra of each doping regime are shown in Fig. 6.1d. In addition to X_0 and trions, PL measurements revealed three new peaks labeled R_1 , R_2 , and R_3 , which were not observed in DR. In other studies, the peaks R_2 and R_3 were attributed to defect-localized excitons [92, 139–141], and R_1 was assigned to excitons bound to localized charges in the substrate as it is found at the same energy as the trion [124]. The latter scenario would result in an inhomogeneously broadened PL peak that reflects the distance variation of localized charges with respect to the exciton wavefunction in the TMD ML and contradict experimental observations. A common crystal defect class that forms well-defined sub-band-gap energy levels could in principle result in the observed PL peaks R_1 to R_3 [145]. These peaks were, however, absent in DR (Figs. 6.1a and 6.1b) providing an upper limit for the defect density. An alternative model with two scenarios based on phonon-assisted recombination of momentum-indirect excitons explaining these peaks was presented in the previous chapter. For the more probable case, R_1 was identified as an acoustic phonon sideband of momentum-indirect excitons with an electron in the Q valley and the correlated empty state in the K or K' valley. The peaks R_2 and R_3 were attributed to higher-order phonon replica of Q-excitons as well as acoustic (R_2) and optical (R_3) phonon sidebands from K'_1 , the momentum-dark counterpart of lowest-energy spin-dark excitons.

In the following, we present experimental data acquired in a doping-controlled environment tuned to charge neutrality to reveal the nature of R_1 to R_3 . Within the analysis, evidence is provided in support of the model of phonon-assisted recombination of momentum-indirect excitons in ML WSe_2 .

6.3 Photoluminescence evolution with excitation energy and power

Increased PL from semiconducting TMDs can be obtained by tuning the excitation laser to an excitonic absorption resonance. In Fig. 6.2a we show the evolution of the PL as a function of the excitation wavelength for ML WSe_2 , where maximum intensities were obtained for excitation at 669 nm (1.85 eV). In analogy to the excited state of the hydrogen atom [56], this energy corresponds to the $2s$ resonance of the neutral exciton X_0 [146]. The resonance effect was also observed for Raman scattered photons [95] labeled with white stars in Fig. 6.2a. Note that by coincidence one of

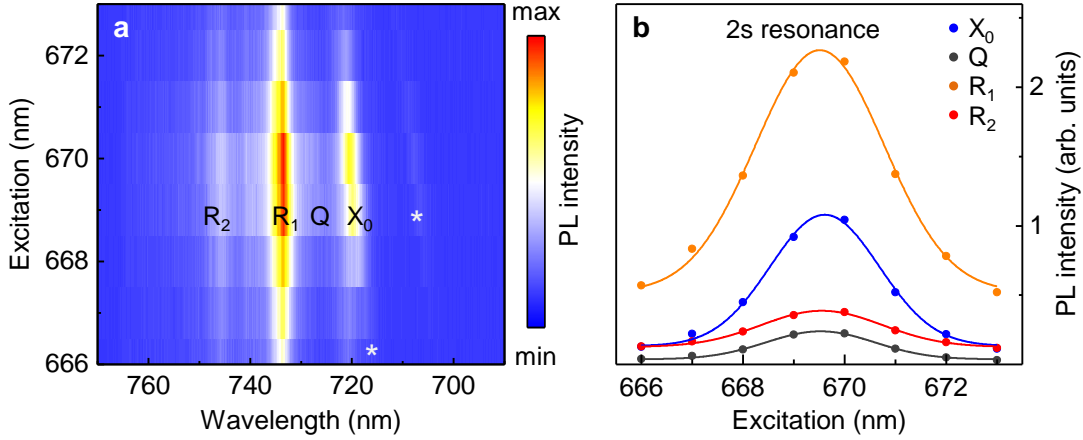


Figure 6.2: **a**, Photoluminescence evolution as a function of excitation wavelength for monolayer WSe₂ encapsulated in hexagonal boron nitride. **b**, Extracted total intensities of the peaks labeled X₀, Q, R₁, and R₂ in **a** showing enhancement when the excitation was tuned over the excitonic 2s resonance of X₀ at 669 nm (1.85 eV); solid lines are Gaussian fits to the data. The dim peaks marked with white stars in **a** correspond to Raman scattered photons. All data were recorded at 3.1 K with a ps-pulsed laser at 3 μW and 76 MHz repetition rate.

the Raman modes crosses the PL of X₀, suggesting a redshift of X₀ for increased excitation wavelengths [128, 146]. The PLE data is evaluated in Fig. 6.2b for all labeled PL peaks, including the dim feature between X₀ and R₁, that matched the energy of the momentum-indirect Q-exciton (see Chapter 5). The emission of this momentum-dark state was probably brightened by strain [147] induced by the sample fabrication process.

Alternatively, this peak could be related to the formation of biexcitons, a four-particle complex of two electrons and two holes that is expected to appear at higher laser powers [148–151]. A signature of biexcitons is their superlinear response with excitation power [152]. Fig. 6.3 shows PL spectra of ML WSe₂ for laser powers tuned from 0.02 to 800 μW (Fig. 6.3a) with peak intensities for X₀, Q and R₁, R₂, QD (Figs. 6.3b and 6.3c, respectively). X₀ and Q exhibited a linear power dependence that evolved into a sublinear response above 30 μW. The absence of superlinear growth contradicts the assignment of Q to biexciton emission.

In contrast to X₀ and Q, the replica peaks R₁ and R₂ showed a change in their PL growth from slope 1.0 to 0.6 above 0.5 μW. The sublinear slope indicates the presence of competing nonradiative recombination such as exciton-exciton annihilation [153–156]. In this regime, an exciton density of $5.8 \pm 0.5 \times 10^{12} \text{ cm}^{-2}$ corresponding to an average exciton separation of about 4 nm was experimentally determined in ML MoSe₂ [154]. By assuming a similar exciton density at the onset of R₁ and R₂

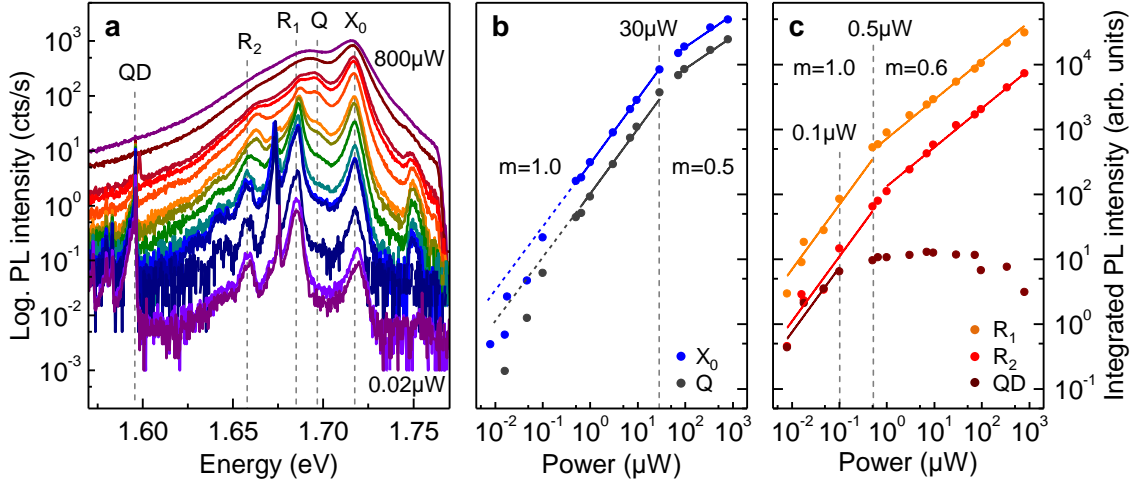


Figure 6.3: **a**, Photoluminescence spectra of monolayer WSe₂ encapsulated in hexagonal boron nitride for excitation powers tuned from 0.02 μW to 800 μW . The artificial cutoff at 1.77 eV was induced by an optical filter. **b** and **c**, Integrated intensities of the peaks in **a** labeled as X₀, Q, R₁, R₂, and QD. X₀ and Q exhibited linear response (slope $m = 1.0$, indicated by dashed and solid lines) at excitation powers below 30 μW , where the intensities started to saturate with slope $m = 0.5$. A change in slope from $m = 1.0$ to 0.6 at 0.5 μW for R₁ and R₂ indicates the onset of nonradiative recombination (solid lines are fits to the data). Spectrally narrow quantum dot (QD) emission saturated at excitation powers above 0.1 μW and photobleached above 70 μW . All data were recorded at 3.1 K with a ps-pulsed laser at 1.85 eV and 76 MHz repetition rate.

annihilation processes with defect localization as their origin, we estimate a defect density of about 0.35% in the WSe₂ ML. This, however, would result in a low-energy absorbance of about 0.75% [145] not observed in our DR measurements (Fig. 6.1).

In our samples, defect-localized emission from QDs was found at 1.59 eV. These emitters are known for their antibunched photon statistics and, as opposed to the short lifetimes of a few picoseconds for delocalized excitons in TMD MLs [139], they feature extended lifetimes in the nanosecond range [34, 44–47]. Fig. 6.4a shows a zoom into the PL spectrum of a QD, where the ZPL featured no fine-structure splitting. The PL dynamics of the ZPL (measured in the spectral band indicated in Fig. 6.4a) exhibited monoexponential decay with a lifetime of 127 ns (Fig. 6.4b), which is about a factor of 100 longer than the typical values reported for WSe₂ MLs [34, 44–47, 49].

In our experiments, most QDs saturated at excitation powers of roughly 0.1 μW and photobleached at powers above 70 μW (Fig. 6.3c). The different power dependence of R₁ and R₂ combined with their absence in reflection measurements suggests that localization is not their origin. The lifetime study of different PL peaks in the

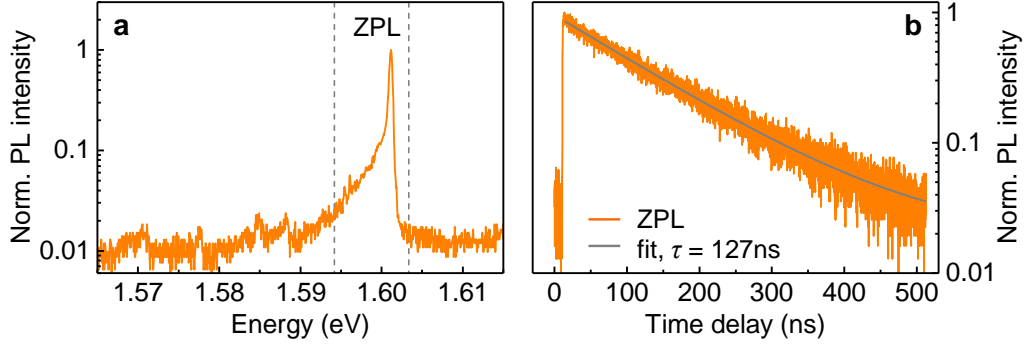


Figure 6.4: **a**, Photoluminescence spectrum of a quantum dot in monolayer WSe₂. **b**, Time-correlated photoluminescence of the quantum dot zero-phonon line (ZPL) measured in the spectral window indicated by the gray dashed lines in **a**; gray solid line is a mono-exponential fit to the data with decay constant τ of 127 ns. All data were recorded at 3.1 K with a ps-pulsed laser at 1.85 eV, 0.5 μW , and 2 MHz repetition rate.

next section further supports our analysis that R_1 and R_2 are related to momentum-indirect excitons.

6.4 Exciton decay dynamics

To obtain nonradiative contributions to the decays of X_0 , R_1 , and R_2 , we performed time-resolved PL measurements as a function of the excitation power. Fig. 6.5a shows a representative WSe₂ ML PL spectrum (gray), where spectral bands (blue, orange, and red) were used to filter the X_0 , R_1 , and R_2 resonances. Representative PL decay traces of the X_0 and R_1 bands at 1 μW , 10 μW , and 300 μW excitation are shown in Figs. 6.5b and 6.5c. The instrument response (gray trace) of 5.5 ps was limited by the detector (streak camera) resolution and pulse dispersion in our fiber-coupled microscope. For analysis, the data were fitted with incomplete bi- (X_0) or triexponential (R_1 and R_2) decay functions given by

$$\mathcal{I}(t) = y_0 + \sum_{n=0}^2 \sum_{i=1}^3 \frac{\sqrt{\pi} a_i T}{2} \left[1 + \text{erf} \left(\frac{2t_i(t + nt_{\text{rep}}) - T^2}{2t_i T} \right) \right] \exp \left(-\frac{T^2 - 4t_i(t + nt_{\text{rep}})}{4t_i^2} \right), \quad (6.1)$$

where $\mathcal{I}(t)$ is the time-resolved PL intensity, t the time delay, T is the laser pulse duration, t_{rep} the laser repetition rate, and y_0 the detection background. The time constants t_1 , t_2 , and t_3 for triexponential decay were fixed to 5.5 ps (resolution limit), 19.5 ps, and 60 ps, respectively, while the amplitudes a_i were varied, with a_3 set to zero for biexponential fits of X_0 . In our experiments, both the fast radiative decay

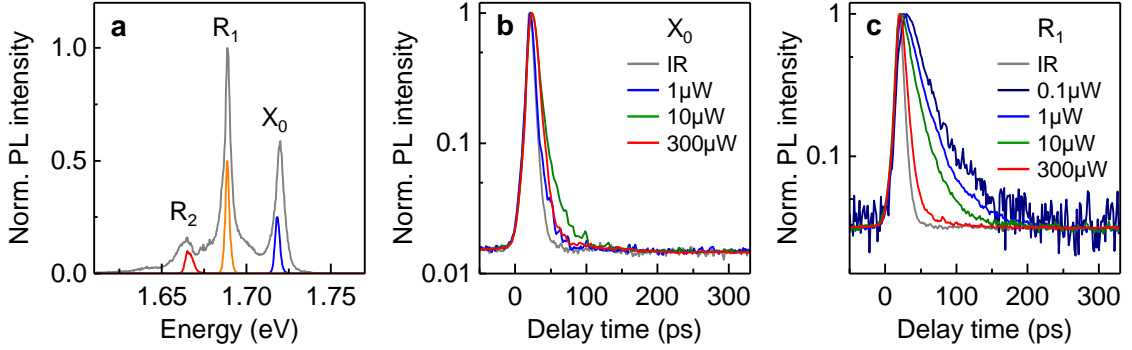


Figure 6.5: **a**, Photoluminescence spectrum (gray trace) of monolayer WSe₂ encapsulated in hexagonal boron nitride. Spectral bands for time-correlated measurements of the neutral exciton X₀, and replica peaks R₁ and R₂ are shown in blue, orange, and red, respectively. **b**, PL decay of the X₀ band for excitation powers of 1 μW, 10 μW, and 300 μW; the instrument response (IR) is shown in gray. **c**, Same as **b** for the R₁ band and including the decay trace at 0.1 μW. All data were recorded at 3.1 K with a ps-pulsed laser at 1.85 eV and 76 MHz repetition rate.

time of X₀ [139] and the nonradiative recombination time [154] for all spectral bands were restricted by the resolution limit t_1 .

We attribute the slower decay component t_2 , that was required for the biexponential fit of X₀, to recombination of momentum-indirect excitons. Similar decay times on the order of 25 ps have been reported for momentum-indirect excitons in BL WSe₂ at low temperatures [36]. Fig. 6.6b shows the evolution of fit components a_1 and a_2 with excitation power for the X₀ band. Fast radiative PL with amplitude a_1 dominates over the component a_2 for low excitation powers in the regime of linear response (Fig. 6.6a). At higher powers, resolution-limited nonradiative recombination, that is also captured by a_1 , outcompetes the radiative PL. This change is discernible in the sublinear growth of the PL intensity with excitation power (Fig. 6.6a). The relative increase of a_2 with respect to a_1 around $\sim 10 \mu\text{W}$ was likely due to spectral leakage from power-broadened momentum-indirect excitons (R₁) into the band of X₀ (compare to Fig. 6.3a). Alternatively, the increase of the 19.5 ps decay component in the spectral band of X₀ could stem from contributions of momentum-dark K'_u excitons (see Chapter 5) brightened by strain-induced relaxation of optical selection rules. This hypothesis was tested with polarization-resolved measurements and is discussed at a later point.

Fig. 6.6d shows the intensity ratio between the nonradiative (a_1) and the radiative (a_2 and a_3) decay contributions to R₁ and R₂. At low excitation powers, where nonradiative recombination is negligible, the decay of the R₁ and R₂ bands was governed by the timescale t_2 and contributions from t_3 at longer time delays.

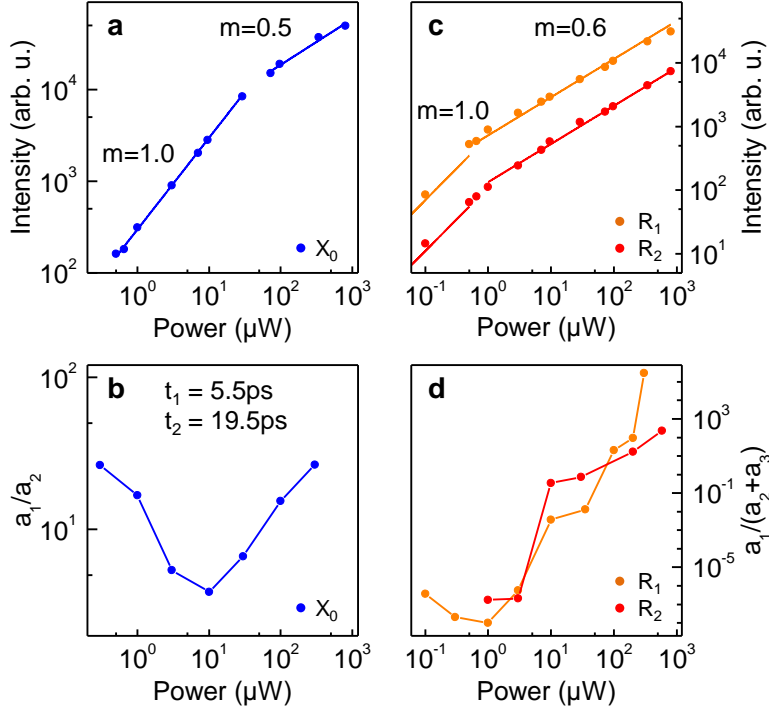


Figure 6.6: **a**, Excitation power dependence of the X₀ PL intensity (data reproduced from Fig. 6.3). **b**, Ratio a_1/a_2 between fast ($t_1 = 5.5$ ps) and slow ($t_2 = 19.5$ ps) amplitude components of X₀ decay traces (shown in Fig. 6.5b) with respect to the excitation power. **c**, Same as **a** for R₁ and R₂ resonances. **d**, Ratio $a_1/(a_2 + a_3)$ between nonradiative ($t_1 = 5.5$ ps) and radiative ($t_2 = 19.5$ ps, $t_3 = 60$ ps) amplitude components of R₁ and R₂ decay traces (Fig. 6.5c) with respect to the excitation power. Note that the onset of $a_1/(a_2 + a_3)$ is correlated with the decrease in slope m at 1 μW from 1.0 to 0.6 for R₁ and R₂. All data were recorded at 3.1 K with a ps-pulsed laser at 1.85 eV and 76 MHz repetition rate.

The vanishing contribution of the slow time constant t_3 above 1 μW is indicative for exciton localization at lower excitation powers [139]. For higher excitation powers, the increasing ratio of $a_1/(a_2 + a_3)$ together with the simultaneous sublinear power dependence of the R₁ and R₂ PL intensities signify a superlinear increase of nonradiative exciton recombination (Figs. 6.6d and 6.6c). From this we conclude that fast nonradiative processes are indeed captured by the resolution-limited t_1 decay.

We now return to the spectral band of X₀. As mentioned above, we studied polarization-resolved PL spectra to identify contributions from momentum-indirect K'_u excitons. Fig. 6.7 shows the degrees of circular (P_c) and linear (P_l) polarization, quantified as $P = (I_{co} - I_{cr})/(I_{co} + I_{cr})$, of emission intensities detected in co-polarized (I_{co}) and cross-polarized (I_{cr}) configurations for circularly or linearly

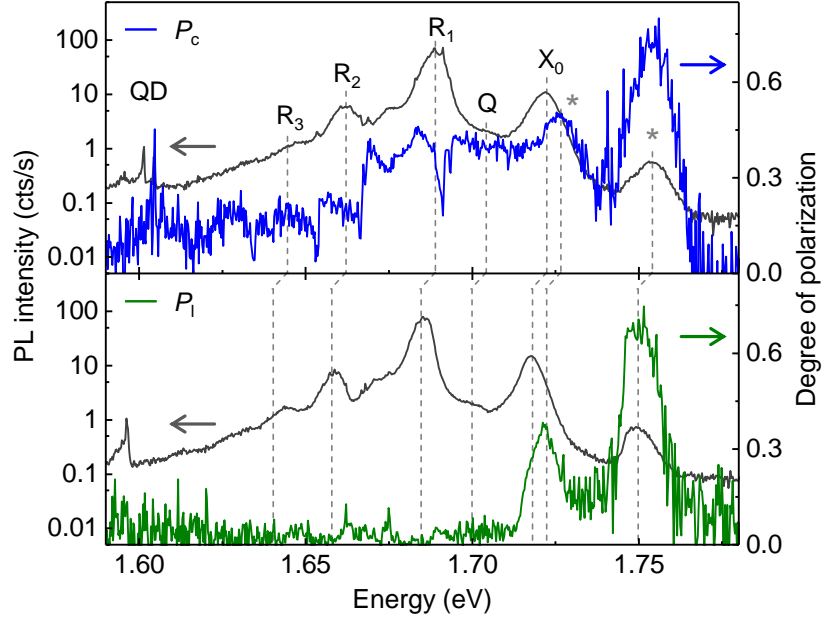


Figure 6.7: Photoluminescence of monolayer WSe_2 encapsulated in hexagonal boron nitride. Spectra in the upper and lower panels (gray traces) were taken at different positions with a spectral shift by 4 meV due to sample inhomogeneities. Labeled peaks are indicated by dashed lines and described in the main text. Blue and green traces in the upper and lower panels show spectrally-resolved degrees of circular and linear polarization (P_c and P_l , respectively). Note that X_0 maxima of P_c and P_l appear blueshifted to the photoluminescence at the dashed line. All data were recorded at 3.1 K with excitation at 1.85 eV and 3 μW .

polarized excitation. The P_c and P_l spectra (blue and green traces) exhibited maxima that were blue-detuned from the X_0 resonance in PL (gray traces). This observation indicates that decay components in the red wing of X_0 are not valley-conserving, as expected for K'_u excitons. Moreover, for the used excitation in resonance with the $2s$ exciton state of X_0 , the detected PL polarization of excitons was modified by spectrally overlapping Raman scattered photons that exhibited co-polarization with respect to the excitation light [128, 146]. These features are labeled with a gray star in Fig. 6.7 and have been identified previously (Fig. 6.2a). Meaningful spectral analysis can therefore only be performed with an excitation laser away from any exciton resonance to prevent Raman features from interfering with PL emission.

Apart from the substructure at X_0 , P_c exhibited narrow-lined dips at the emission of R_1 , R_2 , and R_3 . These dips of exciton recombination in the opposite valley might result from phonon replicas of momentum-dark excitons. For initial K'_u excitons, scattering of VB (CB) states for intervalley spin-flip transitions necessitates Γ_5 (Γ_4)

phonon symmetry exhibited by E'' (A'') modes (see Section 2.4). In other words, the scattering of empty states of momentum-dark K'_u excitons into the K' valley would facilitate σ^- polarized emission. The involved in-plane optical phonon mode E'' , where two selenium atoms vibrate out of phase and the tungsten atom is static, exhibits a longitudinal and a transverse component that could be related to the split-peak feature at R_1 . While these particular processes have not been considered in our spectral analysis, they provide indications for phonon-mediated scattering in the PL of ML TMDs.

6.5 Exciton g -factors in WSe_2 monolayers and bilayers

In this section, we compare the g -factors of low-energy excitons in hBN-encapsulated ML WSe_2 and BL WSe_2 . Figs. 6.8a and 6.8b show PL spectra of a ML and BL for linearly polarized excitation and valley-selective circularly polarized detection at -8 T. For the ML X_0 exciton, we obtained a g -factor of 4.3 ± 0.2 which agrees well with literature [76, 77]. The peaks R_1 and R_2 exhibited g -factors of 11.5 ± 0.2 and 11.5 ± 1.5 , respectively. Large g -factors of unidentified ML peaks have been reported previously and were attributed to localized excitons [157]. According to our model, the high g -factors of R_1 and R_2 are related to momentum-indirect excitons with electrons in the Q valley and empty states in K or K' . To test this assumption, we compare the g -factors of ML WSe_2 to the g -factors of momentum-indirect excitons P_1 to P_4 in BL WSe_2 . For these peaks we obtained g -factors ranging from 10 ± 2 to 12 ± 2 that were similar to the values found for R_1 and R_2 in ML crystals. In the following chapter, we identify the peaks P_1 to P_4 as excitons constructed with an electron residing in the Q valley. It is therefore tempting to relate the high g -factors of 11 ± 1 in MLs to momentum-indirect excitons of a similar type.

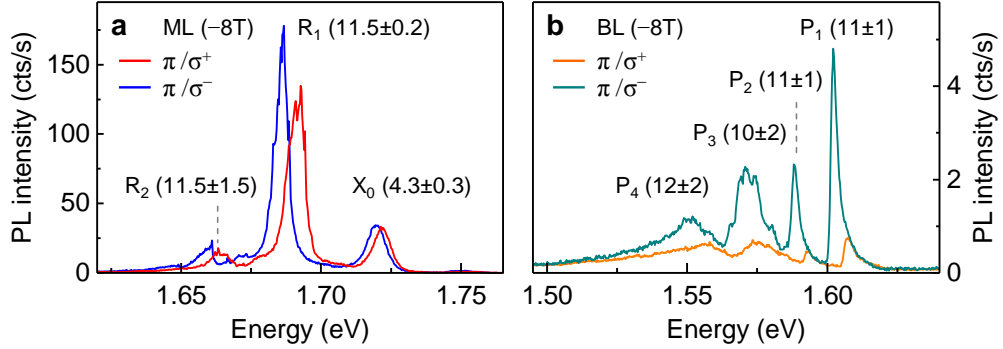


Figure 6.8: **a** and **b**, Photoluminescence spectra of monolayer (ML) and bilayer (BL) WSe₂ encapsulated in hexagonal boron nitride in an external magnetic field of -8 T perpendicular to the crystal surfaces. The data were recorded at 3.1 K with linearly polarized (π) excitation at 1.85 eV and 3 μ W, and detected in circularly polarized bases. Red (blue) and orange (cyan) traces in **a** and **b** correspond to σ^+ (σ^-) circularly polarized detection, probing the population and energy of excitons in the K (K') valley. Exciton g -factors of labeled peaks are given in parentheses. Note the similar g -factors for monolayer exciton replica peaks R_1 and R_2 of 11.5 ± 1.5 and bilayer peaks P_1 to P_4 ranging from 10 ± 2 to 12 ± 2 .

6.6 Conclusions

Absorption and PL characteristics for doping-controlled ML WSe₂ were studied to identify signatures of momentum-dark excitons. In agreement with our previous analysis, PL peaks R_1 , R_2 , and R_3 assigned to phonon sidebands of momentum-dark excitons were absent in reflectance measurements. The sublinear power dependence of R_1 and R_2 , without saturation at high laser fluences, contradicted signatures expected for exciton localization. Time-resolved measurements revealed resolution-limited nonradiative decay processes for replica peaks and X_0 excitons with lifetimes below 5.5 ps. Moreover, emission peaks associated with phonon replicas exhibited remarkably similar characteristics with momentum-indirect excitons of BL crystals, such as radiative lifetimes of ~ 20 ps and large excitonic g -factors of around 11.

Chapter 7

Momentum-dark excitons in bilayer systems

THIS CHAPTER IS ADAPTED FROM THE PUBLICATION [P3](#) AND THE MANUSCRIPT [P5](#):

J. Lindlau, M. Selig, A. Neumann, L. Colombier, J. Förste, V. Funk, M. Förg, J. Kim, G. Berghäuser, T. Taniguchi, K. Watanabe, F. Wang, E. Malic, and A. Högele. *The role of momentum-dark excitons in the elementary optical response of bilayer WSe₂*. *Nat. Commun.* **9**, 2586 (2018). Licensed under a Creative Commons Attribution 4.0 International (CC BY 4.0) License.

M. Förg, L. Colombier, R. Patel, J. Lindlau, A.D. Mohite, H. Yamaguchi, D. Hunger, and A. Högele. *Cavity-control of bright and dark interlayer excitons in van der Waals heterostructures*. ArXiv e-prints (2017). [arXiv:1710.00990](#).

Monolayer TMDs undergo substantial changes in the single-particle band structure and excitonic optical response upon the addition of just one layer. As opposed to the single-layer limit, the band gap of bilayer TMD semiconductors is indirect which results in reduced photoluminescence with richly structured spectra that have eluded a detailed understanding to date. In this chapter, we provide a closed interpretation of the elementary optical responses of bilayer WSe₂ as a representative material for the wider class of TMD semiconductors. By combining theoretical calculations with comprehensive spectroscopy experiments, we identify the crucial role of momentum-indirect excitons for the understanding of basic absorption and emission spectra ubiquitously exhibited by various TMD bilayers. Our results shed light on the origin of quantum dot formation in monolayer and bilayer crystals and will facilitate further advances directed at optoelectronic applications of layered TMD semiconductors in van der Waals heterostructures and devices.

7.1 Introduction

As opposed to MLs, in BL TMDs, the single-particle band gap is indirect because of a downshift of the CB energy at Q well below K and an upshift of the VB edge at the Γ point upon the addition of a second layer [4, 158–160]. In the specific case of BL WSe₂ crystals, the lowest CB minimum is located at Q, while the VB maximum at K exceeds the one at Γ only by 40 ± 30 meV according to angle-resolved photoemission spectroscopy [161]. The associated PL spectra are thus dominated by momentum-indirect transitions interconnecting electrons and holes in dissimilar valleys [36, 64, 140, 159, 162–165]. The BL emission is consistently less efficient, with PL from short-lived direct excitons [36] redshifted by a few tens of meV from the ML peak emission, and a second peak with larger redshift and longer lifetimes [36] attributed to momentum-indirect excitons composed of electrons in the K or Q valleys and holes in the K or Γ valleys [36, 64, 140, 164, 165]. A detailed understanding of both peaks, however, has remained elusive [63] despite the significance of BL TMDs as hosts of novel single-photon sources [34, 35], finite valley polarization [36], or potential utilization of the spin-layer locking effect in charged BLs [37].

In the following, a comprehensive study is presented of exciton manifolds in BL WSe₂. Using cryogenic spectroscopy of BL regions subjected to strain at unintentional disorder, brightening of momentum-indirect excitons is identified that in many cases is accompanied by the formation of QDs with intense emission of nonclassical light. Complementary experiments reveal the energy-level hierarchy of all excitons involved in determining the fundamental optical response of BL WSe₂. These findings, in good quantitative agreement with theoretical calculations, not only explain the intricate details of the BL PL spectra and the origin of the QD PL, they can be also generalized to other representatives of TMD materials to facilitate a detailed understanding of optoelectronic properties of BL and multilayer semiconductors.

7.2 Photoluminescence spectroscopy of bilayer WSe₂

Cryogenic spectroscopy of ML and BL WSe₂ was carried out on a flake shown in Fig. 7.1a obtained by standard exfoliation onto a Si/SiO₂ substrate (see Chapter 3 for details on the experimental setup). Extended ML and BL regions (marked with arrows) were identified by their respective contrast in the optical micrograph of Fig. 7.1a and by Raman spectroscopy. The dashed square indicates the region of the cryogenic hyperspectral raster-scan PL map recorded with a home-built confocal microscope. The false-color map in Fig. 7.1b shows PL peak maxima in the spectral range of 1.43–1.59 eV, highlighting extended homogeneous regions of bright ML and

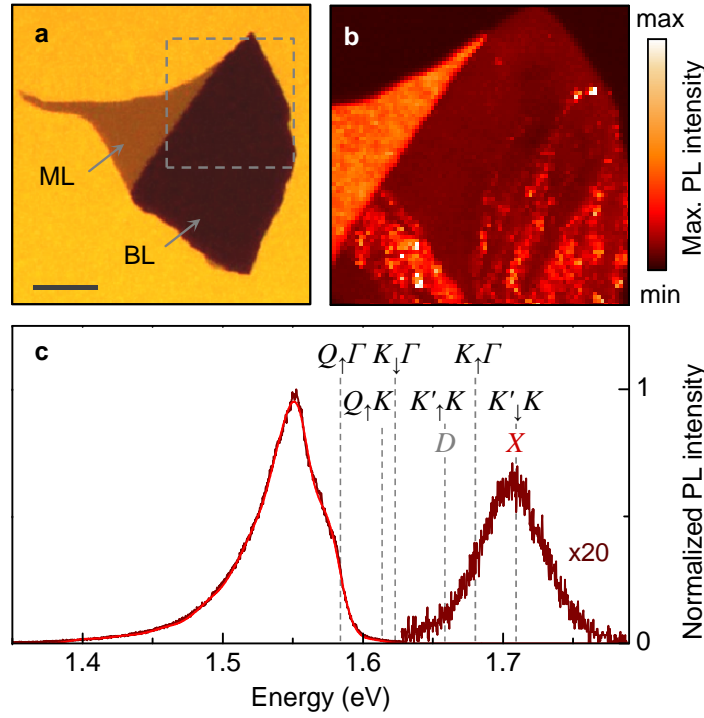


Figure 7.1: **a**, Optical micrograph of a WSe_2 flake exfoliated onto Si/SiO_2 with monolayer (ML) and bilayer (BL) regions indicated by the arrows (the scale bar is $15 \mu\text{m}$). **b**, Cryogenic raster-scan photoluminescence map of the upper corner indicated by the dashed square in **a**. False-color plot of the photoluminescence maxima in the spectral range of 1.43–1.59 eV. The bilayer exhibits extended and punctual regions of brightening attributed to strain at local folds. **c**, Normalized photoluminescence spectrum (brown, magnified by a factor of 20 in the range of 1.62–1.82 eV) at a representative bilayer position away from defects with model fit shown as red solid line. The energy positions of momentum-bright (X and D) and momentum-dark BL excitons ($Q_{\uparrow}\Gamma$, $Q_{\uparrow}K$, $K_{\downarrow}\Gamma$, $K'_{\uparrow}K$, $K_{\uparrow}\Gamma$, and $K'_{\downarrow}K$, labeled by the capital letters of electron and empty state valleys and the electron out-of-plane spin as subscript) are indicated by dashed lines. All spectroscopy measurements were performed at 4.2 K with excitation at 1.95 eV.

dim BL luminescence, as well as distinct BL regions of unintentional disorder with PL brightening due to local strain [34, 35].

A characteristic PL spectrum of BL WSe_2 on SiO_2 , recorded at 4.2 K on a representative position away from disorder, is shown in Fig. 7.1c. The PL exhibits a weak peak around 1.71 eV and a stronger peak around 1.55 eV consistent with previous PL studies of BL WSe_2 [36, 64, 140, 164]. Based on comprehensive experiments described in the following, we develop a model to interpret the PL of WSe_2 BLs as originating from both momentum-direct and momentum-indirect excitons with energy positions indicated by the dashed lines in Fig. 7.1c.

7.3 Excitons in bilayer WSe₂

To identify all relevant excitons that contribute to cryogenic PL and to interpret the model fit to the lower-energy PL peak shown as the red solid line in Fig. 7.1c, it is instructive to consider first the single-particle band structure of BL WSe₂ in Fig. 7.2a and the associated exciton dispersions plotted in Fig. 7.2b. The relevant states for the construction of excitons (indicated by ellipses in Fig. 7.2a) with an empty state located at the VB maxima in the K or Γ valley are the spin-polarized subband minima near K, Q, and K' valleys of the CB, with out-of-plane spin projections indicated by the arrows. We take the spin-degenerate VB maximum at Γ to be 40 meV below the energy of the spin-polarized band edge at K [161], and the energies of the CB at K, Q, and K' from density functional theory calculations [166, 167].

The excitonic dispersions, shown in Fig. 7.2b, were computed using the Wannier equation [168, 169] within the Keldysh formalism [170–172], taking explicitly the dielectric environment of the TMD material into account. The corresponding excitons, all of which have their counterparts with the empty VB state at K', can be separated into the class of zero-momentum excitons with spin-allowed and spin-forbidden configuration (labeled as X and D , respectively), and finite-momentum excitons involving Coulomb-correlated electrons and unoccupied VB states from dissimilar valleys (labeled in Fig. 7.2b according to the valleys of the CB electron and the VB unoccupied state as capital letters with the electron out-of-plane spin as subscript). All excitons but X are dipole-forbidden, either due to spin or momentum conservation constraints.

Energy minima of the branches are given in eV with respect to the bright exciton X (see Ref. P3 for the details of theoretical calculations). Consistent with the downshift (upshift) of the Q (Γ) valley in the CB (VB) of BL WSe₂, we found the smallest exciton gap for finite-momentum $Q_{\uparrow}\Gamma$ and $Q_{\uparrow}K$ excitons, followed by six branches involving an electron in K or K' (two energy-degenerate branches of D and $K'_{\uparrow}K$, and X and $K'_{\downarrow}K$ excitons with the unoccupied state at K, as well as exciton branches $K_{\uparrow}\Gamma$ and $K_{\downarrow}\Gamma$ with the empty VB state at Γ), and two branches of excitons at highest energies with electrons in one of the three spin-down polarized Q valleys forming $Q_{\downarrow}\Gamma$ and $Q_{\downarrow}K$ with the unoccupied states in Γ and K valleys, respectively. We emphasize that although we use a spin-tagged notation for Q-momentum excitons consistent with the schematics in Fig. 7.2a, there are energetically degenerate excitons composed of electrons from the other three inequivalent Q pockets with opposite spin.

Out of this set of excitons, spin-bright X states emit PL along the detection axis of our microscope, and the PL from spin-dark D excitons with in-plane emission is detected due to the high NA of the objective as well [14]. In contrast, all momentum-

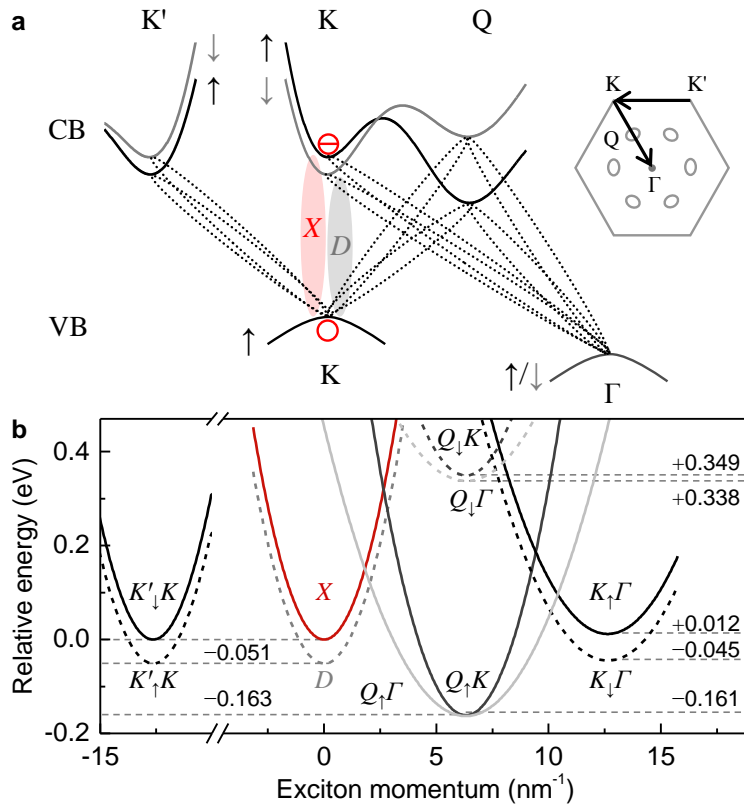


Figure 7.2: **a**, Schematic single-particle band diagram of the conduction and the valence bands of bilayer WSe_2 along high symmetry lines of the hexagonal Brillouin zone shown on the right. Zero-momentum spin-bright (X) and spin-dark (D) excitons are formed in the K valley by electrons from spin-up and spin-down conduction subbands indicated in black and gray, respectively, paired with a spin-up valence band empty state. Momentum-indirect excitons with electrons and unoccupied states in dissimilar valleys are indicated by dashed ellipses. **b**, Calculated dispersions of lowest-energy exciton manifolds in bilayer WSe_2 with energy minima given in eV with respect to the bright exciton X .

indirect excitons appear exclusively as phonon replicas of their optically dark ZPL as they emit photons only with the assistance of acoustic or optical phonons. With this constraint in mind, we note that the higher-energy peak of the BL spectrum in Fig. 7.1c is dominated by the ZPL of X (in accord with the onset of DR, shown in Fig. 7.3a) with a weak contribution from D to the red wing, while the lower-energy PL peak is a superposition of phonon sidebands of momentum-dark excitons $Q_{\uparrow}\Gamma$, $Q_{\uparrow}K$, and $K_{\downarrow}\Gamma$.

Postponing a detailed explanation for the energy ladder of all relevant exciton states indicated by the dashed lines in Fig. 7.1c, we first discuss the model fit of the lower-energy peak in the BL spectrum. For the decomposition of the peak (red solid

line in Fig. 7.1c) into the PL contributions from $Q_{\uparrow}\Gamma$, $Q_{\uparrow}K$, and $K_{\downarrow}\Gamma$, we set the energy positions of the respective dark ZPLs to the experimentally determined values and modeled the phonon replicas by inhomogeneously broadened Gaussians with a FWHM linewidth γ . For simplicity, we involved only one branch of acoustic and optical phonons (the LA and LO phonon branch) with energies given in Ref. 61. Best fit to the spectrum was obtained with the inhomogeneous linewidth $\gamma = 21$ meV. The inclusion of up to sixth-order scattering processes was required to reproduce the extended low-energy tail of the spectrum.

Same fitting procedure, applied to the PL spectrum of another sample of BL WSe₂ on SiO₂ shown in Fig. 7.3b, was obtained with $\gamma = 25$ meV and a global blueshift of momentum-dark exciton energies by 6 meV. The difference in the FWHM linewidths as well as the overall blueshift reflect differences in the effective dielectric environments of BL flakes for the two samples which in turn stem from variations in the exfoliation process. In both cases, second- and third-order scattering from $K_{\downarrow}\Gamma$ and $Q_{\uparrow}K$, respectively, and up to sixth-order scattering from the lowest state $Q_{\uparrow}\Gamma$ were included to reproduce the red-most wing of the PL spectrum. The presence of phonon scattering processes of such high order out of $Q_{\uparrow}\Gamma$ is consistent with efficient relaxation and trapping of exciton population in this lowest-energy momentum-dark state.

We used the same approach to model the PL spectra (brown) of two different samples of BL WSe₂ encapsulated in between two layers of hBN (Figs. 7.3c and 7.3d). The corresponding DR spectra (black), shown in Figs. 7.3c and 7.3d, respectively, highlight interference effects in reflectivity due to multiple reflection planes. To determine the energy position of momentum-indirect excitons referenced to the energy of the bright exciton, we used the respective PL data of each sample and kept all energy spacings constant. Best model fits to the data in Figs. 7.3c and 7.3d (red traces) were obtained for inhomogeneous linewidths of 21 meV and 8 meV, respectively. Despite the nominally identical procedures used in the fabrication of the two samples, the difference in the sample quality reflected by the different inhomogeneous broadenings is noticeable but not surprising. These differences in the spectral widths necessitated up to third-order phonon scattering in the model fit in Fig. 7.3c and only first-order (second-order) scattering from $K_{\downarrow}\Gamma$ and $Q_{\uparrow}K$ ($Q_{\uparrow}\Gamma$) were required for the model fit in Fig. 7.3d.

At the level of theory, the energetic ordering of $Q_{\uparrow}\Gamma$ and $Q_{\uparrow}K$ states is ambiguous given the small difference of 2 meV in the energy minima of the two branches (Fig. 7.2b). However, complementary spectroscopy experiments on strained BL regions and QDs discussed in the following remove this ambiguity and establish the energy-scale hierarchy for all excitons responsible for the elementary optical response

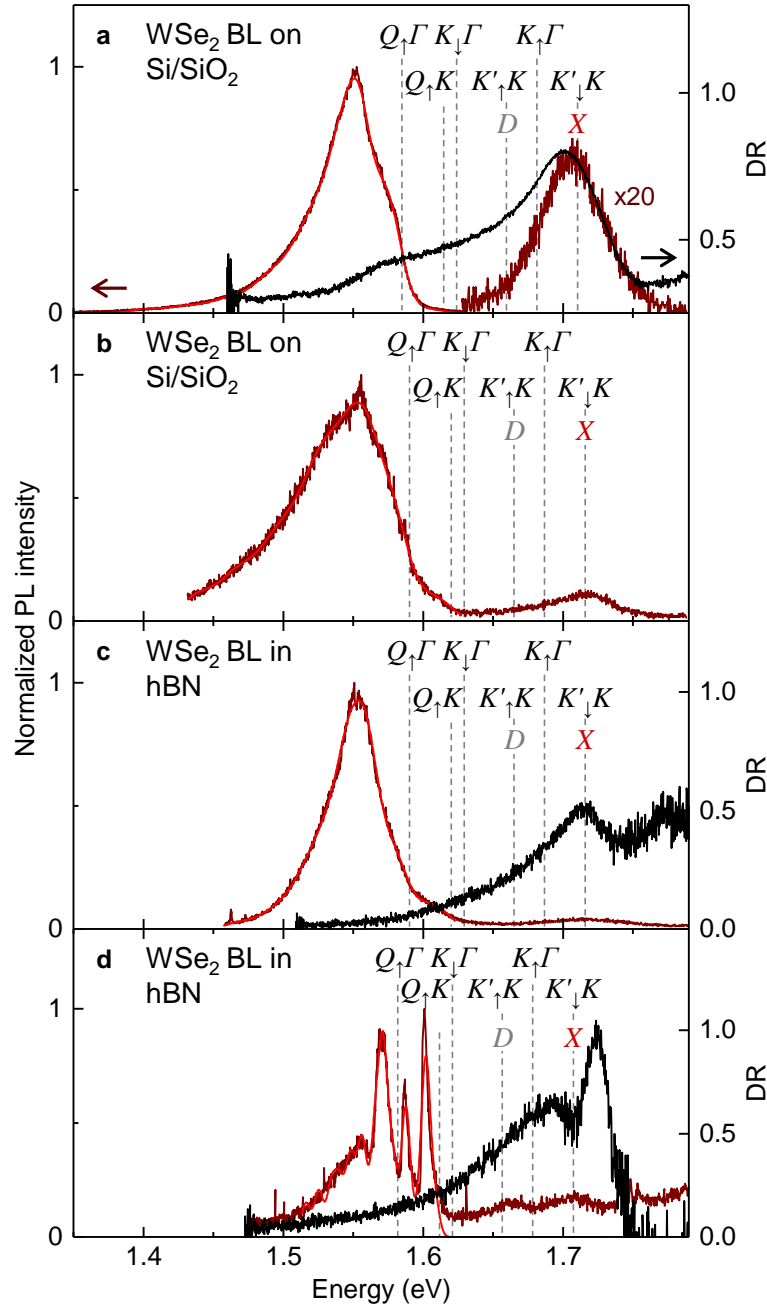


Figure 7.3: **a**, Photoluminescence spectrum (brown) with the respective model fit (red) duplicated from Fig. 7.1c, and differential reflectivity (black). **b**, Normalized photoluminescence (brown) and model fit (red) for a bilayer WSe_2 on Si/SiO₂ from a different sample. The exciton resonances are blueshifted by 6 meV with respect to **a** as indicated by the dashed lines. **c** and **d**, Normalized photoluminescence (brown) and differential reflectivity (black) spectra from two different samples of bilayer WSe_2 encapsulated in hexagonal boron nitride; brown and red traces in **d** are identical to Fig. 7.7a. Best model fits (red) were obtained for inhomogeneous linewidths of 21, 25, 21, and 8 meV in **a**, **b**, **c**, and **d**.

of BL WSe₂ with $Q_{\uparrow}\Gamma$ as the lowest-energy exciton branch, followed by $Q_{\uparrow}K$, $K_{\downarrow}\Gamma$, degenerate D and $K'_{\uparrow}K$ states, $K_{\uparrow}\Gamma$, and degenerate X and $K'_{\downarrow}K$ manifolds.

7.4 Effects of strain and local disorder

The first input to the experimental determination of the exciton energies is provided by the PL spectroscopy of QDs distributed randomly along the lines of disorder (Fig. 7.1b). BL QDs, with intense and spectrally narrow PL emission as in Fig. 7.4a, emerge as a result of local strain [34, 35]. Akin to ML QDs [34, 44–49], the QDs in disordered BL regions were characterized by strong antibunching signatures in the second-order correlation function $g^{(2)}(\tau)$ of their PL emission [34, 35], as demonstrated exemplarily by the inset data of Fig. 7.4a recorded on a different QD with a dip of 0.2 at $\tau = 0$ and an exponential rise to 1 on a timescale of ~ 10 ns. By plotting the PL intensity as a function of the respective energy maximum for all QDs of the hyperspectral map of Fig. 7.1b, we identify a sharp cutoff to the QD emission energy at 1.584 eV (indicated by the left-most dashed line in Fig. 7.4b), which we assign to the state $Q_{\uparrow}\Gamma$ (see Fig. 7.5 for assignment).

The energy position of the next higher-energy momentum-dark state is revealed by the PL spectroscopy of strained BL regions. The PL spectrum on a strained position features characteristic blue- and redshifts of a few meV for the upper and lower PL peaks (compare red and brown traces in Fig. 7.4a) consistent with $\sim 0.1\%$ of tensile strain which lowers (raises) the CB energy minimum at the K (Q) points [173]. In addition, a shoulder at 1.615 eV, indicated by the dashed line in Fig. 7.4a, becomes apparent due to strain-induced brightening of this momentum-dark transition [147]. The energy position of this shoulder reappears as a resonance in the PLE spectrum of a strained BL spot (open red circles in Fig. 7.4b). The resonance, marked by the dashed line and assigned to $Q_{\uparrow}K$, is even more pronounced in the PLE spectrum of the QD from the same spot position (with the spectrum in Fig. 7.4a) shown by open orange circles in Fig. 7.4b. We note that the PLE spectrum is not QD-specific, it rather represents generic BL resonances in the PLE of QDs emitting at different observation sites with different energies (see Fig. 7.6 for PLE spectra of other QDs).

The third successive energy level of momentum-dark states, identified at 1.624 eV by the resonance and the shoulder of the QD and strained BL PLE spectra of Fig. 7.4b, respectively, is ascribed to $K_{\downarrow}\Gamma$. With this energy, the experimental values of the three lowest-energy momentum-dark exciton states can now be hierarchically ordered with respect to the energy of the bright exciton X at 1.710 eV deduced from the peaks of both PLE spectra of Fig. 7.4b and from PL in Fig. 7.1c (and DR shown in Fig. 7.3a). Referencing all energies to that of X , we note first that

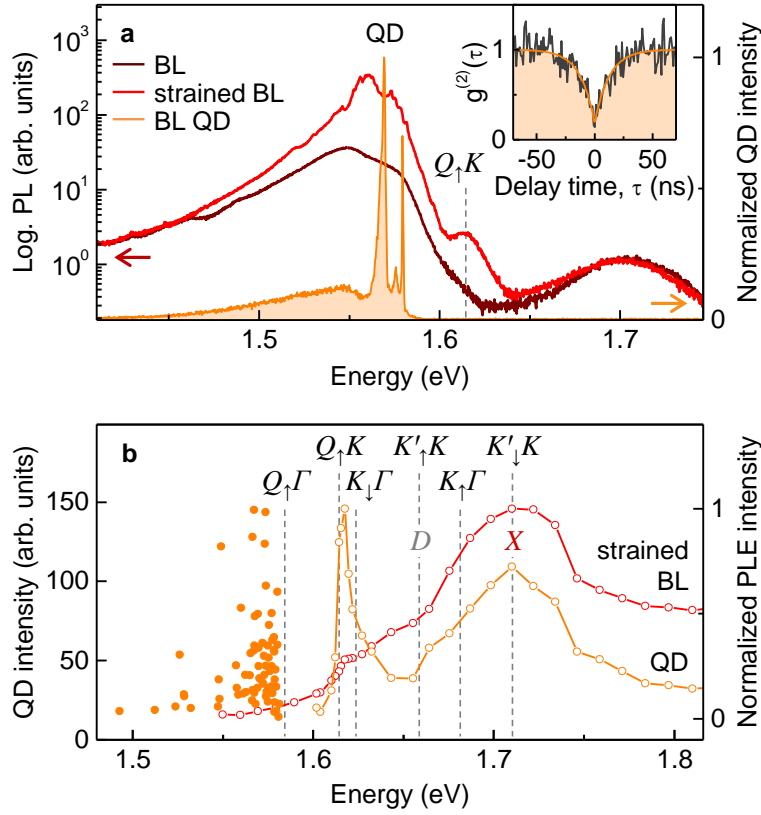


Figure 7.4: **a**, Photoluminescence from a strained bilayer (BL) region without (red) and with (orange) spectrally narrow and intense quantum dot (QD) emission recorded at a factor of 1000 lower excitation power. The bilayer spectrum away from strained regions (brown) is shown for reference. Note the strain-induced emergence of the shoulder at 1.615 eV labeled as $Q_{\uparrow}K$. Inset: typical second-order coherence of a single quantum dot with pronounced antibunching on ~ 10 ns time scale. **b**, Distribution of quantum dot intensities as a function of their peak emission energies (filled circles, extracted from the map of Fig. 7.1b), and photoluminescence excitation spectra of the quantum dot and strained bilayer emission in **a** (orange and red open circles, respectively). The dashed lines mark the energy positions of the relevant exciton states.

the lowest momentum-forbidden state $Q_{\uparrow}\Gamma$ is redshifted by 126 meV instead of the calculated value of 163 meV, while the second-lowest state $Q_{\uparrow}K$ exhibits a redshift of 95 meV instead of 161 meV expected from theory. Provided that the effective masses used in the calculations of exciton energies were correct, these quantitative discrepancies between theory and experiment convert into an upshift of the CB minimum at the Q valley by 66 meV and a downshift of the VB at the Γ point by 29 meV. Given the uncertainties in band structure calculations [166, 167] and

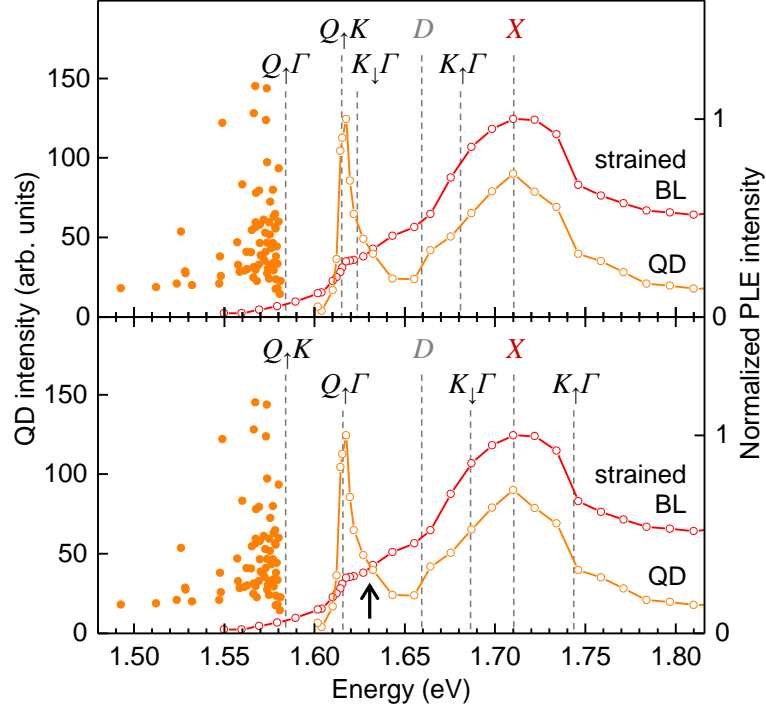


Figure 7.5: Data duplicated from Fig. 7.4b. Upper panel: energy positions and peak assignments of dark-exciton states according to the theoretically predicted energy-scale hierarchy. Lower panel: energy positions of momentum-dark excitons according to the reversed ordering of the two lowest-energy states. Note the missing peak assignment in the lower panel indicated by the arrow.

angle-resolved photoemission [161] used to calculate the exciton dispersion minima, these corrections of a few tens of meV seem reasonable.

Finally, with the energies of X and $K_{\downarrow}\Gamma$ at hand, we estimate the energies of D and $K_{\uparrow}\Gamma$ in Fig. 7.4b by using the respective spin-orbit splittings of 51 meV and 57 meV from Fig. 7.2b. While the energy level of $K_{\uparrow}\Gamma$ has no compelling signature in the PLE spectra of Fig. 7.4b, the D state coincides with a clearly pronounced shoulder in the PLE spectrum of the QD. To complete the energetic ordering of all lowest-lying excitons in BL WSe₂, the states $K'_{\uparrow}K$ and $K'_{\downarrow}K$ are placed in resonance with D and X by omitting electron-hole exchange.

In order to rationalize the energetic ordering of momentum-dark excitons, the data Fig. 7.4b is reproduced in both panels of Fig. 7.5. The energies identified from the cutoff to the QD PL as well as from QD and BL PLE spectra were referenced to the energy of the bright exciton X at $E_X = 1.710$ eV that lies 51 meV above its spin-orbit split momentum-direct spin-dark counterpart D according to theory. The energies of the two lowest-energy dark-exciton states were identified as $E_1 = 1.584$ eV

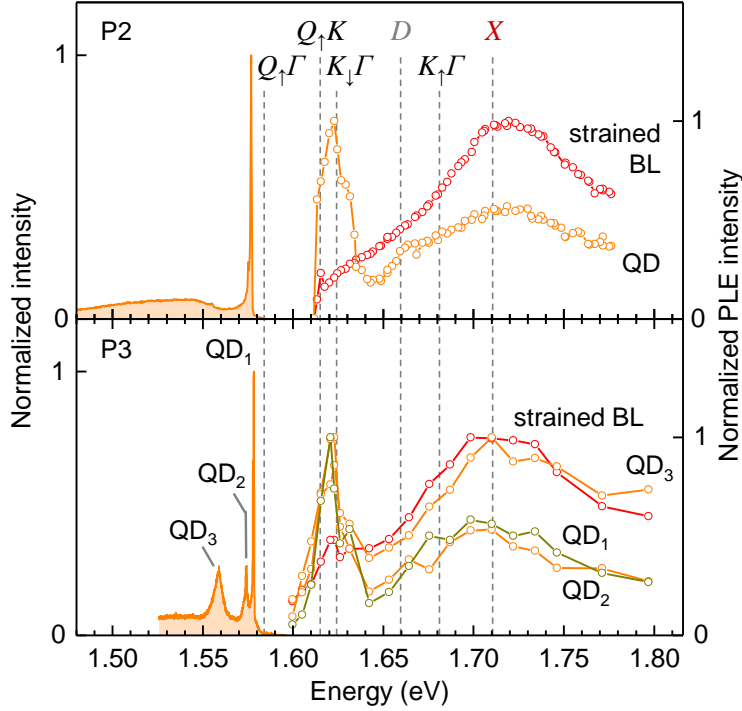


Figure 7.6: Photoluminescence excitation spectra (open circles) of quantum dot and strained bilayer emission recorded on two different positions P2 and P3 (top and bottom panels, respectively) of disorder-strained bilayer WSe₂ with photoluminescence spectra shown in orange (filled traces). The exciton energies marked by the dashed lines are the same as in the upper panel of Fig. 7.5 and in Fig. 7.4b.

and $E_2 = 1.615$ eV, yielding experimental shifts of $\Delta_{1-X}^{\text{exp}} = E_1 - E_X = -126$ meV and $\Delta_{2-X}^{\text{exp}} = E_2 - E_X = -95$ meV with respect to the energy of X . According to theoretical calculations, the two lowest-energy states $Q_{\uparrow}\Gamma$ and $Q_{\uparrow}K$, separated by $\Delta_{Q_{\uparrow}\Gamma-X}^{\text{th}} = -163$ meV and $\Delta_{Q_{\uparrow}K-X}^{\text{th}} = -161$ meV, respectively, compete for the assignment to the lowest-energy states.

First, we test the scenario of preserved energy-scale hierarchy with $Q_{\uparrow}\Gamma$ state being lowest in energy (with energy E_1), followed by the state $Q_{\uparrow}K$ (with energy E_2). We note that the states $Q_{\uparrow}K$ and X share their unoccupied state in the K valley and thus the energy difference can be entirely attributed to the electron in the CB minimum at Q. With $\Delta_{2-X}^{\text{exp}} - \Delta_{Q_{\uparrow}K-X}^{\text{th}} = 66$ meV, we thus directly obtain the upshift of the exciton energy with the unoccupied state in K and the electron in Q. For the state $Q_{\uparrow}\Gamma$ we obtain the difference between the experimental and theoretical values as $\Delta_{1-X}^{\text{exp}} - \Delta_{Q_{\uparrow}\Gamma-X}^{\text{th}} = 37$ meV, which implies a downshift of the VB maximum at Γ by 29 meV by using the upshift of the CB minimum at Q calculated above. The energy of the state $K_{\uparrow}\Gamma$, which shares with X the electron in

the spin-up polarized subband at K, computed by including the downshift of Γ to 1.681 eV. Finally, the energy of the state $K_{\downarrow}\Gamma$ is obtained as 1.624 eV by taking into account the theoretically calculated spin-orbit splitting of 57 meV between $K_{\uparrow}\Gamma$ and $K_{\downarrow}\Gamma$.

The second scenario probes the reversed ordering, where the state $Q_{\uparrow}K$ is lowest (with energy E_1) and $Q_{\uparrow}\Gamma$ is second-lowest state (with energy E_2). Calculations of the respective energies for all relevant momentum-dark states along the lines of arguments given above yields an upshift of the Q valley by 35 meV and an upshift of the Γ valley by 33 meV. Accordingly, the energies of $K_{\uparrow}\Gamma$ and $K_{\downarrow}\Gamma$ states are obtained as 1.743 eV and 1.686 eV, respectively.

The energy positions for all relevant excitons obtained from the two competing assignment scenarios are plotted as dashed lines in Fig. 7.5. The upper panel shows the energetic ordering in accord with preserved hierarchy, while the lower panel shows the results of reversed ordering. The failure of the latter to predict the resonance in PLE at 1.624 eV (indicated by the black arrow in the lower panel), which is consistently ascribed in the framework of the former to the state $K_{\downarrow}\Gamma$, provides strong evidence for $Q_{\uparrow}\Gamma$ being the lowest and $Q_{\uparrow}K$ being the second-lowest state.

Remarkably, all PLE resonances appeared at the same energy positions for different BL regions subjected to unintentional strain (PLE spectra in Fig. 7.6) with confocal PL from QDs emitting at different PL energies (orange spectra in Fig. 7.6). This observation indicates that the PLE resonances are not QD-specific (e.g. due to excited QD states that would differ from dot to dot because of different confinement potentials) but indeed probe the absorption of BL WSe_2 .

7.5 Field-effect control of doping in bilayer WSe_2

The set of exciton energies obtained from the analysis of PL signatures of BL WSe_2 on SiO_2 in Fig. 7.1c was tested on narrow spectra of a gate-tunable WSe_2 BL encapsulated in hBN (see section 7.3). Fig. 7.7a shows the normalized PL spectrum (brown) under charge neutrality conditions with the corresponding model fit (same PL data as in Fig. 7.3d). Remarkably, the intricate spectral features of the spectrum can be reproduced with the set of exciton energies established above with an overall redshift of 2 meV. The spectrally narrow inhomogeneous linewidths down to ~ 8 meV required a refined model fit with all phonon modes included and variations of ± 2 meV around the values calculated for ML WSe_2 in Ref. 61.

Including first-order scattering from $K_{\downarrow}\Gamma$ and $Q_{\uparrow}K$ exciton manifolds, and up to second-order scattering from $Q_{\uparrow}\Gamma$, our model identifies the blue-most peak at ~ 1.6 eV out of the three strong peaks in the spectrum of Fig. 7.7a in the range 1.61–1.57 eV as optical and acoustic phonon replica of $K_{\downarrow}\Gamma$ and $Q_{\uparrow}K$, respectively,

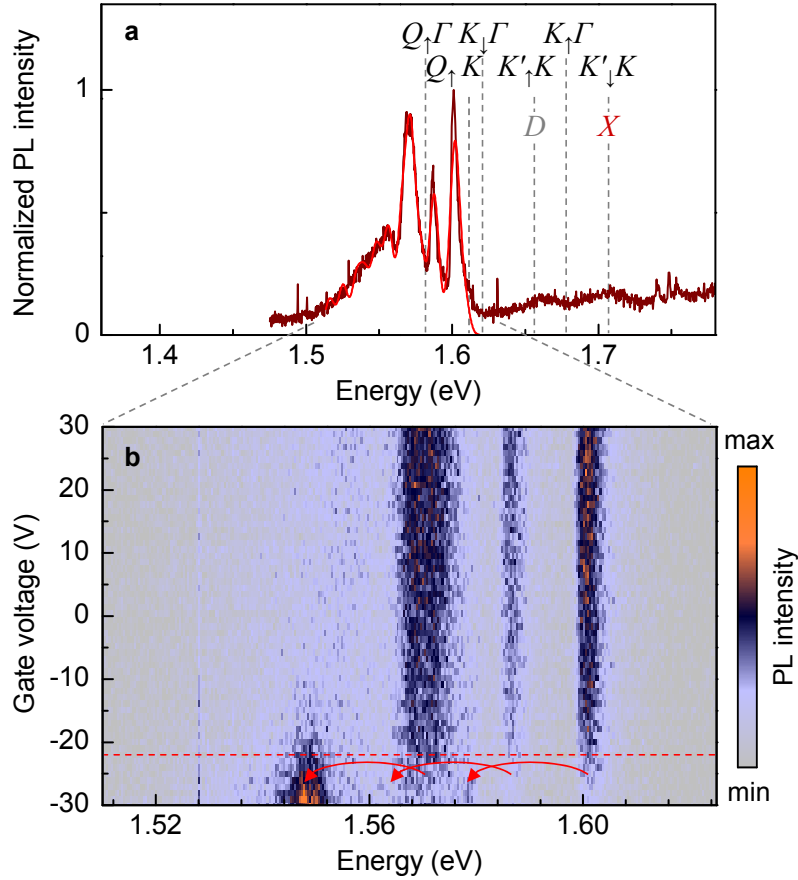


Figure 7.7: Field-effect control of bilayer WSe_2 photoluminescence. **a**, Normalized photoluminescence (brown) of a bilayer WSe_2 encapsulated in hexagonal boron nitride and tuned towards charge neutrality with positive gate voltages. Best fit to the spectrum (red) was obtained with the same set of exciton energies as in Fig. 7.1c and an overall redshift of 2 meV. **b**, Evolution of the photoluminescence with gate voltage from -30 V to 30 V. Note the crossover to the charged regime below -20 V signified by a simultaneous redshift of 22 meV for all peaks as indicated by the red arrows below the dashed line.

the central peak as an optical sideband of $Q_{\uparrow}K$, and the red-most peak as an acoustic sideband of $Q_{\uparrow}\Gamma$. The consecutive peak towards lower energies around 1.56 eV is an optical sideband of $Q_{\uparrow}\Gamma$ that merges with the extended red wing composed of higher-order phonon replicas from all the above mentioned momentum-dark states.

Interestingly, the ambiguity with respect to the origin of the blue-most peak as being composed of acoustic or optical sidebands of $K_{\downarrow}\Gamma$ and $Q_{\uparrow}K$ momentum-dark states is removed by the observation of a simultaneous shift of all three peaks upon negative doping at gate voltages below -20 V in Fig. 7.7b. At this voltage, finite electron population of the Q pockets favors the formation of BL trions with

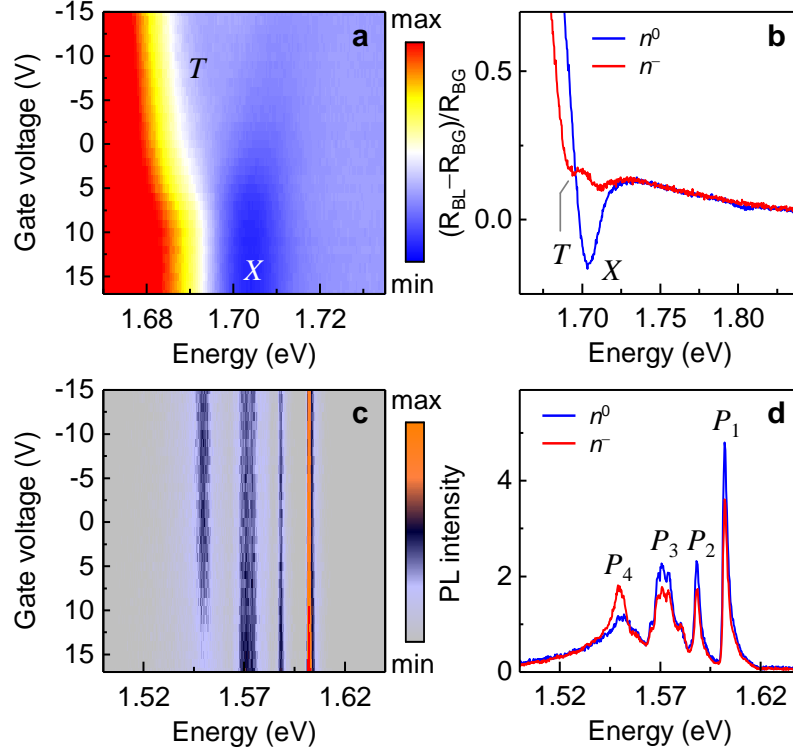


Figure 7.8: Field-effect control of differential reflectivity and photoluminescence for a second WSe₂ bilayer encapsulated in hexagonal boron nitride. **a**, Evolution of differential reflectivity with gate voltage from +17 V to −15 V. The data was measured as $(R_{\text{BL}} - R_{\text{BG}})/R_{\text{BG}}$, where R_{BL} and R_{BG} are reflectivities on and off the bilayer. Charge neutrality signified by X excitons occurred for gate voltages above 9 V; for smaller voltages in the electron-doped regime, formation of T trions was favored. **b**, Spectra extracted from **a** at neutral (n^0 , blue trace) and electron-doped conditions (n^- , red trace). **c**, Photoluminescence evolution for gate voltages ranging from +17 V to −15 V. The spectral region (similar to Fig. 7.7b) shows phonon-assisted emission of momentum-indirect excitons. **d**, Neutral (n^0 , blue trace) and electron-doped (n^- , red trace) photoluminescence spectra from the evolution in **c** with peaks labeled P_1 to P_4 .

electrons forced to reside in different Q valleys by the Pauli exclusion principle. Thus, all sideband replicas associated with $Q_{\uparrow}K$ and $Q_{\uparrow}\Gamma$ states are expected to shift simultaneously. This is exactly what we observe upon negative doping with a redshift by the trion binding energy of ~ 22 meV for all three peaks. The shift of the blue-most peak implies that it originates from the $Q_{\uparrow}K$ rather than the $K_{\downarrow}\Gamma$ state, as the latter is insensitive to the increasing doping level at Q.

Similar results were obtained from a second hBN-encapsulated WSe₂ BL. For this sample, the evolution of DR with gate voltage clearly shows a transition from charge neutrality to an electron-doped regime below 9 V (Fig. 7.8a). Representative

DR spectra at charge neutrality (n^0) and electron-doped regime (n^-) with neutral (X) and trion (T) resonances, respectively, are shown in Fig. 7.8b. Note that the high reflection intensity at energies below 1.68 eV is an artifact due to interference effects at the hBN layers and the Si/SiO₂ substrate. The PL of the low-energy WSe₂ BL spectrum showed a similar evolution with gate voltage as the first sample (compare Figs. 7.8c and 7.7b). With doping (red trace in Fig. 7.8d), the intensity of peaks labeled P_1 to P_3 decreased, while P_4 became more pronounced.

7.6 Magneto-optical properties of bilayer quantum dots

The notion of momentum-dark exciton states provides a new perspective on the origin of QDs in ML [34, 44–49] and BL [34, 35] TMDs. In addition to spectrally narrow and bright PL with antibunched photon emission statistics discussed above, BL QDs share all main signatures of localized excitons with ML QDs. In high-resolution micro-PL spectroscopy, they exhibit a doublet of states with orthogonal linear polarization (Figs. 7.9a and 7.9b), which evolves into a pair of circularly polarized Zeeman-split peaks with increasing magnetic field (Figs. 7.9a and 7.9c). The dispersion of the Zeeman splitting Δ between the blue and red QD branches with out-of-plane magnetic field B according to the hyperbolic function $\Delta = \sqrt{(g\mu_B B)^2 + \Delta_0^2}$ (solid line in Fig. 7.9c) is a hallmark of QDs with anisotropic fine-structure splitting Δ_0 [174]. At large enough fields, the linear asymptote of the Zeeman splitting is determined by the exciton g -factor scaled by the Bohr magneton μ_B .

By applying this analysis to ten randomly selected QDs on strained BL positions, we extracted g and Δ_0 from the hyperbolic fit to the Zeeman splitting as for the QD of Figs. 7.9a and 7.9c with $g = 9.5 \pm 0.1$ and $\Delta_0 = 500 \pm 10 \mu\text{eV}$. Remarkably, as evidenced from Fig. 7.9d, the g -factor of all ten QDs shows only minor variations around the average value of 9.5 independent of the QD PL energy and despite the spread in the fine-structure splittings in the range of ~ 400 – $900 \mu\text{eV}$ [34, 35, 44–47, 49]. This observation suggests that QD excitons relate to momentum-dark excitons that inherit their g -factor from the delocalized continuum state (i.e. $Q_\uparrow\Gamma$ in the case of BL WSe₂) and exhibit significant brightening due to their spread in momentum space upon spatial localization. This picture is further supported by the sharp cutoff to the emission energy of BL QDs at the energy of $Q_\uparrow\Gamma$ momentum-dark excitons in Fig. 7.4b as well as in previous studies [34, 35].

For QDs in ML WSe₂ with similarly sharp cutoff energies at ~ 20 – 25 meV below the bright state X [34, 35, 44, 46, 47, 49] and surprisingly large g -factors in the range of 6–12 [34, 35, 44–47], this insight suggests the presence of a momentum-

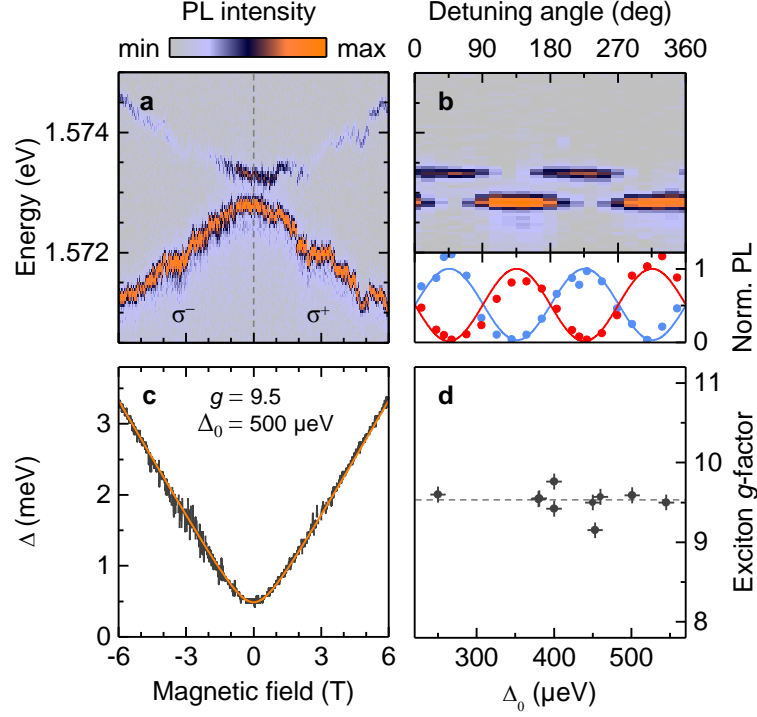


Figure 7.9: Quantum dots in bilayer WSe₂. **a**, False-color plot of quantum dot magnetoluminescence under σ^+ (σ^-) polarized excitation for positive (negative) magnetic fields in Faraday geometry. **b**, The quantum dot emission doublet (upper panel) is characterized by linearly polarized peaks with orthogonal polarization axes (lower panel; note the anti-correlation in the intensities of the higher- and lower-energy peaks shown in red and blue together with squared sine and cosine fits). **c**, Energy dispersion of the doublet splitting Δ in magnetic field. Best fit to the data with a hyperbolic function (solid line) was obtained for a zero-field fine-structure splitting Δ_0 of 500 μeV and an exciton g -factor of 9.5. **d**, Distribution of exciton g -factors around the mean value of 9.5 plotted for ten quantum dots with respect to their zero-field splitting.

dark reservoir between the bright and dark ML excitons X and D (see Chapter 5). In ML MoSe₂ void of momentum-dark states below the bright exciton, on the other hand, no cutoff energy to the QD emission was observed and similar values for the g -factors of QD excitons and the bright X exciton were found [48]. To leverage this speculation, theoretical calculations of exciton g -factors are required for all excitons constructed from CB electrons and VB unoccupied states in valleys other than K.

7.7 Spectral signatures in MoSe_2 - WSe_2 heterobilayers

In the following, we discuss optical signatures of TMD heterobilayers (HBL) formed by two different materials as counterparts to BLs consisting of same layers. With intrinsic type-II band alignment, they feature both intralayer excitons and spatially indirect (interlayer) excitons as lowest-energy states in their PL spectra. The interlayer excitons constructed with electrons and holes from different layers, exhibit a permanent electric dipole moment. Here, we study the main signatures of intralayer and interlayer excitons in a CVD-grown HBL with cryogenic PL spectroscopy. Our van der Waals heterostructure was synthesized by overgrowth of ML MoSe_2 with a ML of WSe_2 (Fig. 7.10a). Upon optical excitation, photogenerated electrons and holes relax into the CB minima and VB maxima of MoSe_2 and WSe_2 MLs, respectively [175]. After relaxation, zero-momentum excitons are formed with layer-separated electrons and holes, while excitons with finite momentum emerge from Coulomb correlations among electrons and holes in dissimilar valleys.

As opposed to exfoliation-stacking, CVD realizes inherently aligned TMD heterostructures with atomically sharp interfaces both in lateral and vertical geometries [176, 177]. However, even in the presence of inherent angular alignment, excitons in van der Waals stacks of incommensurate layers with dissimilar lattice constants are subject to moiré effects [178–182], just like twisted HBL systems [183]. In CVD-grown MoS_2 - WSe_2 HBLs, moiré patterns with a period of ~ 10 nm emerge from a lattice mismatch of 3.7% [180]. In MoSe_2 - WSe_2 heterostructures, on the other hand, the strain resulting from a lattice mismatch of 0.1% can be accommodated by atomic vacancies to yield a fully commensurate HBL system free of moiré effects [184]. Such commensurate van der Waals HBL realize ideal R- and H-type stacking geometries, respectively [185]. Here, we focus on systems with the latter geometry.

The interlayer excitonic band structure of H-type HBLs features momentum-bright X_B (bright) and lower-lying X_G (gray) excitons with equal and unequal spin configurations of CB and empty VB states. Their counterparts of K-momentum excitons are referred to as X_U and X_L for spin-unlike and spin-like configurations. Both the ZPL of momentum-bright excitons and the phonon sidebands of momentum-dark excitons contribute to the intense red-most peak around 1.4 eV in the PL spectrum of our as-grown MoSe_2 - WSe_2 HBLs shown in Fig. 7.10b. In addition to this low-energy HBL peak arising from interlayer excitons as in exfoliation-stacked heterostructures [175, 186–188], intralayer MoSe_2 excitons contribute a pair of blue peaks to the PL around 1.65 eV [175]. Commonly, the higher- and lower-energy ML peaks are assigned to neutral and charged excitons in MoSe_2 , respectively [60].

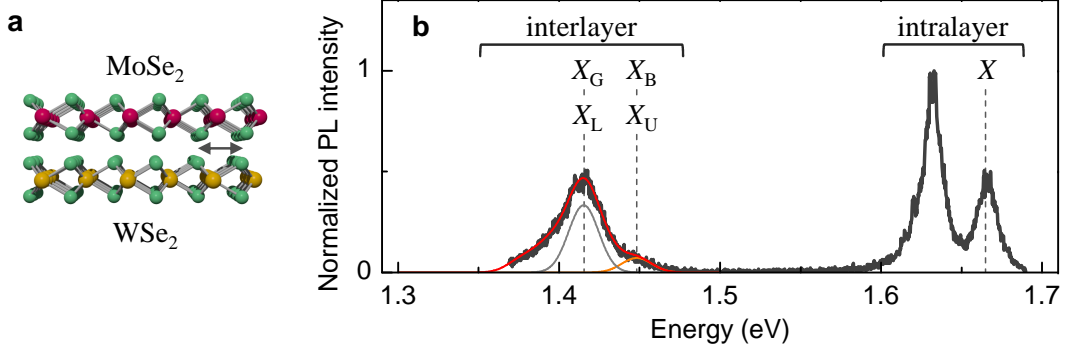


Figure 7.10: **a**, Real-space schematics of a MoSe₂-WSe₂ heterobilayer with a lattice mismatch (indicated by the arrow) between the monolayer constituents. **b**, Cryogenic PL from an as-grown MoSe₂-WSe₂ sample with spectral decomposition (red solid line) of the low-energy spectrum into contributions of zero-momentum bright (X_B , orange solid line) and gray (X_G , gray solid line) interlayer excitons, and phonon sidebands of momentum-dark spin-like and spin-unlike interlayer excitons X_L and X_U . Best-fit energies of interlayer exciton states with respect to MoSe₂ intralayer neutral excitons (X at 1.67 eV) are indicated by dashed lines.

With this notion of the interlayer exciton manifold, we decompose the HBL peak. Bright and gray excitons emit PL directly into ZPLs at their bare energy, indicated by the orange and gray solid lines in Fig. 7.10b. Momentum-indirect excitons, on the other hand, contribute to the PL spectrum as phonon sidebands (Refs. P4 and P3) downshifted from their bare energies X_U and X_L by the energy of acoustic or optical phonons that compensate for momentum mismatch in the light-matter coupling and thus promote radiative decay. The energies of X_B and X_U as well as X_G and X_L , degenerate in the absence of electron-hole exchange and indicated by the dashed lines in Fig. 7.10b, were determined from the best fit of the spectrum (red solid line) using inhomogeneously broadened Gaussians with one global linewidth γ of 18 meV and phonon energies of MoSe₂. The model fit includes one acoustic (LA) and two optical phonon modes (LO, A₁) with respective energies of 19.9 meV, 37.4 meV, and 25.6 meV [61]. For interlayer X_B excitons we obtained a redshift of 218 ± 8 meV with respect to the neutral ML X exciton. The energy separation between X_B and X_G , which accounts for the spin-orbit splitting of ~ 30 meV in ML MoSe₂ is difficult to determine with our fit, due to similar energies of optical phonon sidebands of X_U excitons combined with inhomogeneous broadening. However, the spectral analysis showed that dark excitons contribute to a large extent to the optical properties of MoSe₂-WSe₂ HBLs. Moreover, the model predicts different timescales for bright, gray, and momentum-dark interlayer excitons that were determined with time-resolved measurements (see Ref. P5).

7.8 Conclusions

Following the analysis developed for ML TMDs in Chapter 5, PL emission from BL and HBL systems was interpreted on the basis of spin- and momentum-dark interlayer excitons. This approach was used to qualitatively reconstruct spectra of BL samples in an uncontrolled charge environment. In our analysis, BL momentum-dark excitons were observed as absorption resonances in spectra of localized QD states, which offer large uncertainty in momentum for optical transitions. Apart from the microscopic understanding of QD formation in TMD crystals, our experiments revealed promising features of BL QDs for quantum information technology. Additional charge control of samples encapsulated in hBN allowed to identify momentum-dark BL trions with a binding energy of 22 meV. Furthermore, the lowest momentum-dark exciton state was found to be constructed with Q-valley CB states.

Chapter 8

Summary and perspectives

Within this thesis, optical properties of ML and BL TMDs were studied with confocal optical spectroscopy ranging from ambient to cryogenic environments and in magnetic fields of up to 9 T. The photophysics of TMDs are dominated by excitonic effects at the K and K' valleys of their hexagonal BZ, with unique optical selection rules [30]. In the exciton PL of CVD-grown ML MoS₂, optically initialized valley pseudospins were detected as a high degree of polarization. The robustness of this valley degree of freedom for excitons strongly depended on material quality and was influenced by exciton-phonon interactions [22, 23]. These properties were imaged with Raman spectroscopy and revealed spatial inhomogeneities across the crystal. Exciton-resonant Raman scattering was employed to identify defect-mediated forbidden scattering between excitons and LO phonons in MoS₂ MLs. Moreover, Raman intensities at regular crystal positions were tuned by perpendicular magnetic fields in accord with the resonance condition of valley Zeeman split excitons. This technique provided experimental support for the theoretically proposed scattering mechanism of the dispersive 'b' mode that involves E_{1u}² phonons [121]. Our studies identify magneto-Raman hyperspectroscopy as a valuable method to examine valley photodynamics in TMD crystals.

Apart from Raman spectroscopy, the focus of this thesis was directed towards the identification of low-temperature spectral signatures in the PL of ML and BL crystals. The interpretation of PL features was complicated by the ambiguity of similar trion binding energies and optical phonon energies. A model based on momentum-indirect excitons was developed to assign unidentified peaks in the emission spectra. An essential aspect for the study was the high material quality and control of doping provided by hBN-encapsulated samples with field-effect tunability. The samples allowed to assign unidentified PL peaks to acoustic and optical phonon replicas of momentum-dark excitons. We identified momentum-dark excitons in ML WSe₂ that reside 19 meV below the spin-bright fundamental exciton and are constructed with

an electron in the Q valley and an empty state in the K valley. Acoustic phonon replicas of these dark excitons were responsible for the most intense emission peak in low-temperature spectra.

Complementary optical experiments supported the model of momentum-indirect excitons in ML WSe₂. These include the absence in reflectance measurements of PL peaks assigned to phonon sidebands of momentum-indirect excitons. Their emission exhibited a sublinear power dependence without saturation at higher laser fluences and a dominant decay component of 20 ps, that was also found for momentum-indirect excitons in BLs [36]. In addition, exciton g -factors of phonon replicas ranging from 11 to 14 were also almost identical to the values obtained for BL WSe₂. While our model provides an indication for the large excitonic g -factors in TMD MLs, theoretical calculations are required to leverage our assignments.

Our analysis furthermore contributes to the discussion on conduction subband separations between the Q and K valley in tungsten-based MLs, which have been theoretically calculated in the range of 0–80 meV [19, 61, 73]. One route to resolve the energy of the lowest spin-subband at the Q points could be via the aid of charge-stability diagrams for PL and absorption spectra. This approach allows to deduce energies of different charged states of the system with respect to their doping as was successfully applied to self-assembled QDs [189]. In combination with experimentally determined g -factors of PL peaks in electron- and hole-doped regimes, charge stability diagrams could contribute to a comprehensive understanding of emission features in TMD MLs.

In analogy to the model developed for ML TMDs, spectral signatures of low-energy excitons in indirect band-gap BL WSe₂ were also identified. Theoretical calculations of the exciton band structure combined with elaborate experiments allowed to determine exciton states in BL WSe₂ that give rise to phonon-assisted emission. In our samples, unintentional strain and disorder induced brightening of momentum-dark excitons as well as narrow-lined QD emission. These single-photon emitters were used to sense low-energy excitons. Spectroscopy in a charge-controlled environment signified that lowest-energy BL excitons are constructed with an electron in the Q valley and an empty state in the K (K') or Γ valley. The experiments revealed momentum-indirect trions in BLs WSe₂ with binding energy of 22 meV. Our findings provide a detailed understanding of PL signatures and QD formation in WSe₂ BLs and can be generalized to other representative TMD BL and multilayer crystals. Furthermore, the QDs hosted by BL crystals showed promising features for quantum information technology such as a prolonged nanosecond lifetime. For commercial applications, strain landscapes provide an option to deterministically arrange QDs [35, 49, 190], plasmonic nanocavities could be used to enhance their QY [190], and active charge control would offer access to individual spins [191].

Having identified the spectral characteristics of ML and BL TMDs with emphasis on tungsten-based crystals, we combined MLs of nonequivalent TMDs to create HBLs with novel physical properties. HBLs are known for the formation of spatially indirect excitons hosting electrons and correlated empty states in different layers. In analogy to the model pioneered for ML and BL TMDs, the complex emission spectra of HBLs have been complemented by the realm of interlayer spin-dark and momentum-indirect excitons. Similar to intralayer excitons, interlayer excitons also memorize valley pseudospin information but in contrast exhibit extended lifetimes of up to hundreds of nanoseconds [175, 186–188] and suppressed electron-hole exchange interactions [192]. Incorporated in optical cavities, their inherent static dipole moment offers a playground to study collective coupling phenomena mediated among excitons and photons. One example, that could be realized even at room temperature, is Bose-Einstein condensation of interlayer exciton-polaritons [193] owed to their long lifetimes and repulsive dipolar interactions preventing a collapse to an electron-hole plasma at high densities [194]. Moreover, interactions of exciton-polariton condensates with a 2D electron system may provide new pathways towards high-temperature superconductivity [195–197].

In addition, HBLs form moiré patterns due to a lattice mismatch of dissimilar TMDs [178–182] or a twist angle between individual layers [183]. The moiré pattern causes a locally varying interlayer registry with a periodic modulation of the band gap across the HBL [198] as revealed by scanning tunneling microscopy [180]. These atomic registries form sequentially at high symmetry points of the moiré supercell, where the threefold rotational symmetry is preserved. As a consequence they invoke spatially alternating optical selection rules at the band extrema and may realize QD-like confinement potentials for interlayer excitons [182, 198]. Recent experimental approaches indicated trapped interlayer excitons with narrow PL peaks that exhibited strong valley polarization [199]. Moreover, it has been proposed that band gaps of different registries are electrically tunable by a perpendicular field, enabling a position switch for exciton confinement and inversion of optical selection rules [198]. This may offer new opportunities towards switchable single-photon emitter arrays and a platform to manipulate the properties of moiré excitons after fabrication. Exciting effects of moiré superlattices also appear in other van der Waals materials. In twisted BL graphene, for example, triangular networks of one-dimensional solitons can form at domain walls between different stacking configurations that exhibit distinct electrical and optical properties [200, 201]. At magic twist angles, interlayer orbital hybridization induces flat bands near zero Fermi energy with periodic localization of the real-space wavefunction [202]. These flat energy bands exhibit a correlated insulating phase at half-filling that is indicative for a phase transition to a Mott insulator [203]. Upon electrostatic doping away from the insulating phases,

the strongly correlated system becomes superconducting [204]. The pronounced pairing strength among electrons combined with their vanishing Fermi velocity provides unique possibilities to explore exotic phases of matter in van der Waals materials [205]. Analogously, rotational control of individual layers in semiconducting TMDs can create flat excitonic bands and enhance exciton-exciton interactions to explore and manipulate optically nonlinear effects [206]. In addition, a periodic moiré potential together with a Zeeman field are expected to create excitonic topological bands [181, 198]. These bands support chiral edge states that protect unidirectional exciton transport and can be exploited for topologically protected photonic circuitry [181].

References

- [1] F. Bonaccorso, L. Colombo, G. Yu, M. Stoller, V. Tozzini, A. C. Ferrari, R. S. Ruoff, and V. Pellegrini. *Graphene, related two-dimensional crystals, and hybrid systems for energy conversion and storage*. *Science* **347**, 1246501 (2015).
- [2] A. K. Geim. *Nobel Lecture: Random walk to graphene*. *Rev. Mod. Phys.* **83**, 851–862 (2011).
- [3] K. S. Novoselov. *Nobel Lecture: Graphene: Materials in the Flatland*. *Rev. Mod. Phys.* **83**, 837–849 (2011).
- [4] A. Splendiani, L. Sun, Y. Zhang, T. Li, J. Kim, C.-Y. Chim, G. Galli, and F. Wang. *Emerging Photoluminescence in Monolayer MoS₂*. *Nano Lett.* **10**, 1271–1275 (2010).
- [5] K. F. Mak, C. Lee, J. Hone, J. Shan, and T. F. Heinz. *Atomically Thin MoS₂: A New Direct-Gap Semiconductor*. *Phys. Rev. Lett.* **105**, 136805 (2010).
- [6] D. Xiao, G.-B. Liu, W. Feng, X. Xu, and W. Yao. *Coupled Spin and Valley Physics in Monolayers of MoS₂ and Other Group-VI Dichalcogenides*. *Phys. Rev. Lett.* **108**, 196802 (2012).
- [7] X.-X. Zhang, Y. You, S. Y. F. Zhao, and T. F. Heinz. *Experimental Evidence for Dark Excitons in Monolayer WSe₂*. *Phys. Rev. Lett.* **115**, 257403 (2015).
- [8] G. Wang, C. Robert, A. Suslu, B. Chen, S. Yang, S. Alamdari, I. C. Gerber, T. Amand, X. Marie, S. Tongay, and B. Urbaszek. *Spin-orbit engineering in transition metal dichalcogenide alloy monolayers*. *Nat. Commun.* **6**, 10110 (2015).
- [9] F. Withers, O. Del Pozo-Zamudio, S. Schwarz, S. Dufferwiel, P. M. Walker, T. Godde, A. P. Rooney, A. Gholinia, C. R. Woods, P. Blake, S. J. Haigh, K. Watanabe, T. Taniguchi, I. L. Aleiner, A. K. Geim, V. I. Fal’ko, A. I. Tartakovskii, and K. S. Novoselov. *WSe₂ Light-Emitting Tunneling Transistors with Enhanced Brightness at Room Temperature*. *Nano Lett.* **15**, 8223–8228 (2015).
- [10] M. R. Molas, C. Faugeras, A. O. Slobodeniuk, K. Nogajewski, M. Bartos, D. M. Basko, and M. Potemski. *Brightening of dark excitons in monolayers of semiconducting transition metal dichalcogenides*. *2D Mater.* **4**, 021003 (2017).
- [11] X.-X. Zhang, T. Cao, Z. Lu, Y.-C. Lin, F. Zhang, Y. Wang, Z. Li, J. C. Hone, J. A. Robinson, D. Smirnov, S. G. Louie, and T. F. Heinz. *Magnetic brightening and control of dark excitons in monolayer WSe₂*. *Nat. Nanotechnol.* **12**, 883–888 (2017).

- [12] Y. Zhou, G. Scuri, D. S. Wild, A. A. High, A. Dibos, L. A. Jauregui, C. Shu, K. d. Greve, K. Pistunova, A. Joe, T. Taniguchi, K. Watanabe, P. Kim, M. D. Lukin, and H. Park. *Probing dark excitons in atomically thin semiconductors via near-field coupling to surface plasmon polaritons*. *Nat. Nanotechnol.* **12**, 856–860 (2017).
- [13] Z. Wang, L. Zhao, K. F. Mak, and J. Shan. *Probing the Spin-Polarized Electronic Band Structure in Monolayer Transition Metal Dichalcogenides by Optical Spectroscopy*. *Nano Lett.* **17**, 740–746 (2017).
- [14] G. Wang, C. Robert, M. M. Glazov, F. Cadiz, E. Courtade, T. Amand, D. Lagarde, T. Taniguchi, K. Watanabe, B. Urbaszek, and X. Marie. *In-Plane Propagation of Light in Transition Metal Dichalcogenide Monolayers: Optical Selection Rules*. *Phys. Rev. Lett.* **119**, 047401 (2017).
- [15] G.-B. Liu, W.-Y. Shan, Y. Yao, W. Yao, and D. Xiao. *Three-band tight-binding model for monolayers of group-VIB transition metal dichalcogenides*. *Phys. Rev. B* **88**, 085433 (2013).
- [16] K. Kośmider and J. Fernández-Rossier. *Electronic properties of the MoS_2 - WS_2 heterojunction*. *Phys. Rev. B* **87**, 075451 (2013).
- [17] K. Kośmider, J. W. González, and J. Fernández-Rossier. *Large spin splitting in the conduction band of transition metal dichalcogenide monolayers*. *Phys. Rev. B* **88**, 245436 (2013).
- [18] A. Kormányos, V. Zólyomi, N. D. Drummond, and G. Burkard. *Spin-Orbit Coupling, Quantum Dots, and Qubits in Monolayer Transition Metal Dichalcogenides*. *Phys. Rev. X* **4**, 011034 (2014).
- [19] A. Kormányos, G. Burkard, M. Gmitra, J. Fabian, V. Zólyomi, N. D. Drummond, and V. Fal'ko. *k - p theory for two-dimensional transition metal dichalcogenide semiconductors*. *2D Mater.* **2**, 022001 (2015).
- [20] T. Cao, G. Wang, W. Han, H. Ye, C. Zhu, J. Shi, Q. Niu, P. Tan, E. Wang, B. Liu, and J. Feng. *Valley-selective circular dichroism of monolayer molybdenum disulphide*. *Nat. Commun.* **3**, 887 (2012).
- [21] K. F. Mak, K. He, J. Shan, and T. F. Heinz. *Control of valley polarization in monolayer MoS_2 by optical helicity*. *Nat. Nanotechnol.* **7**, 494–498 (2012).
- [22] H. Zeng, J. Dai, W. Yao, D. Xiao, and X. Cui. *Valley polarization in MoS_2 monolayers by optical pumping*. *Nat. Nanotechnol.* **7**, 490–493 (2012).
- [23] A. M. Jones, H. Yu, N. J. Ghimire, S. Wu, G. Aivazian, J. S. Ross, B. Zhao, J. Yan, D. G. Mandrus, D. Xiao, W. Yao, and X. Xu. *Optical generation of excitonic valley coherence in monolayer WSe_2* . *Nat. Nanotechnol.* **8**, 634–638 (2013).
- [24] J. Kim, X. Hong, C. Jin, S.-F. Shi, C.-Y. S. Chang, M.-H. Chiu, L.-J. Li, and F. Wang. *Ultrafast generation of pseudo-magnetic field for valley excitons in WSe_2 monolayers*. *Science* **346**, 1205–1208 (2014).
- [25] E. J. Sie, J. W. McIver, Y.-H. Lee, L. Fu, J. Kong, and N. Gedik. *Valley-selective optical Stark effect in monolayer WS_2* . *Nat. Mater.* **14**, 290–294 (2015).

- [26] G. Wang, X. Marie, B. Liu, T. Amand, C. Robert, F. Cadiz, P. Renucci, and B. Urbaszek. *Control of exciton valley coherence in transition metal dichalcogenide monolayers*. *Phys. Rev. Lett.* **117**, 187401 (2016).
- [27] Z. Ye, D. Sun, and T. F. Heinz. *Optical manipulation of valley pseudospin*. *Nat. Phys.* **13**, 26–29 (2017).
- [28] E. J. Sie, C. H. Lui, Y.-H. Lee, L. Fu, J. Kong, and N. Gedik. *Large, valley-exclusive Bloch-Siegert shift in monolayer WS_2* . *Science* **355**, 1066–1069 (2017).
- [29] W. Yao, D. Xiao, and Q. Niu. *Valley-dependent optoelectronics from inversion symmetry breaking*. *Phys. Rev. B* **77**, 235406 (2008).
- [30] X. Xu, W. Yao, D. Xiao, and T. F. Heinz. *Spin and pseudospins in layered transition metal dichalcogenides*. *Nat. Phys.* **10**, 343–350 (2014).
- [31] K. F. Mak, K. L. McGill, J. Park, and P. L. McEuen. *The valley Hall effect in MoS_2 transistors*. *Science* **344**, 1489–1492 (2014).
- [32] Y. J. Zhang, T. Oka, R. Suzuki, J. T. Ye, and Y. Iwasa. *Electrically Switchable Chiral Light-Emitting Transistor*. *Science* **344**, 725–728 (2014).
- [33] J. R. Schaibley, H. Yu, G. Clark, P. Rivera, J. S. Ross, K. L. Seyler, W. Yao, and X. Xu. *Valleytronics in 2D materials*. *Nat. Rev. Mater.* **1**, 16055 (2016).
- [34] S. Kumar, A. Kaczmarczyk, and B. D. Gerardot. *Strain-Induced Spatial and Spectral Isolation of Quantum Emitters in Mono- and Bilayer WSe_2* . *Nano Lett.* **15**, 7567–7573 (2015).
- [35] A. Branny, S. Kumar, R. Proux, and B. D. Gerardot. *Deterministic strain-induced arrays of quantum emitters in a two-dimensional semiconductor*. *Nat. Commun.* **8**, 15053 (2017).
- [36] G. Wang, X. Marie, L. Bouet, M. Vidal, A. Balocchi, T. Amand, D. Lagarde, and B. Urbaszek. *Exciton dynamics in WSe_2 bilayers*. *Appl. Phys. Lett.* **105**, 182105 (2014).
- [37] A. M. Jones, H. Yu, J. S. Ross, P. Klement, N. J. Ghimire, J. Yan, D. G. Mandrus, W. Yao, and X. Xu. *Spin-layer locking effects in optical orientation of exciton spin in bilayer WSe_2* . *Nat. Phys.* **10**, 130–134 (2014).
- [38] W.-T. Hsu, Z.-A. Zhao, L.-J. Li, C.-H. Chen, M.-H. Chiu, P.-S. Chang, Y.-C. Chou, and W.-H. Chang. *Second Harmonic Generation from Artificially Stacked Transition Metal Dichalcogenide Twisted Bilayers*. *ACS Nano* **8**, 2951–2958 (2014).
- [39] S. Huang, X. Ling, L. Liang, J. Kong, H. Terrones, V. Meunier, and M. S. Dresselhaus. *Probing the Interlayer Coupling of Twisted Bilayer MoS_2 Using Photoluminescence Spectroscopy*. *Nano Lett.* **14**, 5500–5508 (2014).
- [40] K. S. Novoselov, A. K. Geim, S. V. Morozov, D. Jiang, Y. Zhang, S. V. Dubonos, I. V. Grigorieva, and A. A. Firsov. *Electric Field Effect in Atomically Thin Carbon Films*. *Science* **306**, 666–669 (2004).

- [41] A. M. van der Zande, P. Y. Huang, D. A. Chenet, T. C. Berkelbach, Y. You, G.-H. Lee, T. F. Heinz, D. R. Reichman, D. A. Muller, and J. C. Hone. *Grains and grain boundaries in highly crystalline monolayer molybdenum disulphide*. *Nat. Mater.* **12**, 554–561 (2013).
- [42] S. Najmaei, Z. Liu, W. Zhou, X. Zou, G. Shi, S. Lei, B. I. Yakobson, J.-C. Idrobo, P. M. Ajayan, and J. Lou. *Vapour phase growth and grain boundary structure of molybdenum disulphide atomic layers*. *Nat. Mater.* **12**, 754–759 (2013).
- [43] Y. Zhang, T.-R. Chang, B. Zhou, Y.-T. Cui, H. Yan, Z. Liu, F. Schmitt, J. Lee, R. Moore, Y. Chen, H. Lin, H.-T. Jeng, S.-K. Mo, Z. Hussain, A. Bansil, and Z.-X. Shen. *Direct observation of the transition from indirect to direct bandgap in atomically thin epitaxial MoSe_2* . *Nat. Nanotechnol.* **9**, 111–115 (2014).
- [44] A. Srivastava, M. Sidler, A. V. Allain, D. S. Lembke, A. Kis, and A. Imamoglu. *Optically active quantum dots in monolayer WSe_2* . *Nat. Nanotechnol.* **10**, 491–496 (2015).
- [45] Y.-M. He, G. Clark, J. R. Schaibley, Y. He, M.-C. Chen, Y.-J. Wei, X. Ding, Q. Zhang, W. Yao, X. Xu, C.-Y. Lu, and J.-W. Pan. *Single quantum emitters in monolayer semiconductors*. *Nat. Nanotechnol.* **10**, 497–502 (2015).
- [46] M. Koperski, K. Nogajewski, A. Arora, V. Cherkez, P. Mallet, J.-Y. Veuille, J. Marcus, P. Kossacki, and M. Potemski. *Single photon emitters in exfoliated WSe_2 structures*. *Nat. Nanotechnol.* **10**, 503–506 (2015).
- [47] C. Chakraborty, L. Kinnischtzke, K. M. Goodfellow, R. Beams, and A. N. Vamivakas. *Voltage-controlled quantum light from an atomically thin semiconductor*. *Nat. Nanotechnol.* **10**, 507–511 (2015).
- [48] A. Branny, G. Wang, S. Kumar, C. Robert, B. Lassagne, X. Marie, B. D. Gerardot, and B. Urbaszek. *Discrete quantum dot like emitters in monolayer MoSe_2 : Spatial mapping, magneto-optics, and charge tuning*. *Appl. Phys. Lett.* **108**, 142101 (2016).
- [49] C. Palacios-Berraquero, D. M. Kara, A. R.-P. Montblanch, M. Barbone, P. Latawiec, D. Yoon, A. K. Ott, M. Loncar, A. C. Ferrari, and M. Atatüre. *Large-scale quantum-emitter arrays in atomically thin semiconductors*. *Nat. Commun.* **8**, 15093 (2017).
- [50] C. Lee, H. Yan, L. E. Brus, T. F. Heinz, J. Hone, and S. Ryu. *Anomalous Lattice Vibrations of Single- and Few-Layer MoS_2* . *ACS Nano* **4**, 2695–2700 (2010).
- [51] N. A. Lanzillo, A. Glen Birdwell, M. Amani, F. J. Crowne, P. B. Shah, S. Najmaei, Z. Liu, P. M. Ajayan, J. Lou, M. Dubey, S. K. Nayak, and T. P. O’Regan. *Temperature-dependent phonon shifts in monolayer MoS_2* . *Appl. Phys. Lett.* **103**, 093102 (2013).
- [52] C. Rice, R. J. Young, R. Zan, U. Bangert, D. Wolverson, T. Georgiou, R. Jalil, and K. S. Novoselov. *Raman-scattering measurements and first-principles calculations of strain-induced phonon shifts in monolayer MoS_2* . *Phys. Rev. B* **87**, 081307 (2013).
- [53] H. J. Conley, B. Wang, J. I. Ziegler, R. F. Haglund, S. T. Pantelides, and K. I. Bolotin. *Bandgap Engineering of Strained Monolayer and Bilayer MoS_2* . *Nano Lett.* **13**, 3626–3630 (2013).

- [54] C.H. Lui, Z. Ye, C. Keiser, X. Xiao, and R. He. *Temperature-Activated Layer-Breathing Vibrations in Few-Layer Graphene*. *Nano Lett.* **14**, 4615–4621 (2014).
- [55] B. Chakraborty, A. Bera, D. V. S. Muthu, S. Bhowmick, U. V. Waghmare, and A. K. Sood. *Symmetry-dependent phonon renormalization in monolayer MoS₂ transistor*. *Phys. Rev. B* **85**, 161403 (2012).
- [56] A. Chernikov, T. C. Berkelbach, H. M. Hill, A. Rigosi, Y. Li, O. B. Aslan, D. R. Reichman, M. S. Hybertsen, and T. F. Heinz. *Exciton Binding Energy and Nonhydrogenic Rydberg Series in Monolayer WS₂*. *Phys. Rev. Lett.* **113**, 076802 (2014).
- [57] K. He, N. Kumar, L. Zhao, Z. Wang, K. F. Mak, H. Zhao, and J. Shan. *Tightly Bound Excitons in Monolayer WSe₂*. *Phys. Rev. Lett.* **113**, 026803 (2014).
- [58] Z. Ye, T. Cao, K. O’Brien, H. Zhu, X. Yin, Y. Wang, S. G. Louie, and X. Zhang. *Probing excitonic dark states in single-layer tungsten disulphide*. *Nature* **513**, 214–218 (2014).
- [59] K. F. Mak, K. He, C. Lee, G. H. Lee, J. Hone, T. F. Heinz, and J. Shan. *Tightly bound trions in monolayer MoS₂*. *Nat. Mater.* **12**, 207–211 (2013).
- [60] J. S. Ross, S. Wu, H. Yu, N. J. Ghimire, A. M. Jones, G. Aivazian, J. Yan, D. G. Mandrus, D. Xiao, W. Yao, and X. Xu. *Electrical control of neutral and charged excitons in a monolayer semiconductor*. *Nat. Commun.* **4**, 1474 (2013).
- [61] Z. Jin, X. Li, J. T. Mullen, and K. W. Kim. *Intrinsic transport properties of electrons and holes in monolayer transition-metal dichalcogenides*. *Phys. Rev. B* **90**, 045422 (2014).
- [62] H. Dery and Y. Song. *Polarization analysis of excitons in monolayer and bilayer transition-metal dichalcogenides*. *Phys. Rev. B* **92**, 125431 (2015).
- [63] M. Koperski, M. R. Molas, A. Arora, K. Nogajewski, A. O. Slobodeniuk, C. Faugeras, and M. Potemski. *Optical properties of atomically thin transition metal dichalcogenides: observations and puzzles*. *Nanophotonics* **6**, 1289–1308 (2017).
- [64] W. Zhao, R. M. Ribeiro, M. Toh, A. Carvalho, C. Kloc, A. H. Castro Neto, and G. Eda. *Origin of Indirect Optical Transitions in Few-Layer MoS₂, WS₂, and WSe₂*. *Nano Lett.* **13**, 5627–5634 (2013).
- [65] Q. H. Wang, K. Kalantar-Zadeh, A. Kis, J. N. Coleman, and M. S. Strano. *Electronics and optoelectronics of two-dimensional transition metal dichalcogenides*. *Nat. Nanotechnol.* **7**, 699–712 (2012).
- [66] G.-B. Liu, D. Xiao, Y. Yao, X. Xu, and W. Yao. *Electronic structures and theoretical modelling of two-dimensional group-VIB transition metal dichalcogenides*. *Chem. Soc. Rev.* **44**, 2643–2663 (2015).
- [67] K. F. Mak and J. Shan. *Photonics and optoelectronics of 2D semiconductor transition metal dichalcogenides*. *Nat. Photonics* **10**, 216–226 (2016).
- [68] X. Qian, J. Liu, L. Fu, and J. Li. *Quantum spin Hall effect in two-dimensional transition metal dichalcogenides*. *Science* **346**, 1344–1347 (2014).

- [69] Z. Fei, T. Palomaki, S. Wu, W. Zhao, X. Cai, B. Sun, P. Nguyen, J. Finney, X. Xu, and D.H. Cobden. *Edge conduction in monolayer WTe_2* . *Nat. Phys.* **13**, 677 (2017).
- [70] S. Tang, C. Zhang, D. Wong, Z. Pedramrazi, H.-Z. Tsai, C. Jia, B. Moritz, M. Claassen, H. Ryu, S. Kahn, J. Jiang, H. Yan, M. Hashimoto, D. Lu, R. G. Moore, C.-C. Hwang, C. Hwang, Z. Hussain, Y. Chen, M. M. Ugeda, Z. Liu, X. Xie, T. P. Devereaux, M. F. Crommie, S.-K. Mo, and Z.-X. Shen. *Quantum spin Hall state in monolayer $1T'$ - WTe_2* . *Nat. Phys.* **13**, 683 (2017).
- [71] Z. Y. Zhu, Y. C. Cheng, and U. Schwingenschlöggl. *Giant spin-orbit-induced spin splitting in two-dimensional transition-metal dichalcogenide semiconductors*. *Phys. Rev. B* **84**, 153402 (2011).
- [72] H. Liu, J. Chen, H. Yu, F. Yang, L. Jiao, G.-B. Liu, W. Ho, C. Gao, J. Jia, W. Yao, and M. Xie. *Observation of intervalley quantum interference in epitaxial monolayer tungsten diselenide*. *Nat. Commun.* **6**, 8180 (2015).
- [73] C. Zhang, Y. Chen, A. Johnson, M.-Y. Li, L.-J. Li, P. C. Mende, R. Feenstra, and C.-K. Shih. *Probing Critical Point Energies of Transition Metal Dichalcogenides: Surprising Indirect Gap of Single Layer WSe_2* . *Nano Lett.* **15**, 6494 (2015).
- [74] Y. Li, J. Ludwig, T. Low, A. Chernikov, X. Cui, G. Arefe, Y. D. Kim, A. M. van der Zande, A. Rigosi, H. M. Hill, S. H. Kim, J. Hone, Z. Li, D. Smirnov, and T. F. Heinz. *Valley Splitting and Polarization by the Zeeman Effect in Monolayer MoS_2* . *Phys. Rev. Lett.* **113**, 266804 (2014).
- [75] D. MacNeill, C. Heikes, K. F. Mak, Z. Anderson, A. Kormányos, V. Zólyomi, J. Park, and D. C. Ralph. *Breaking of Valley Degeneracy by Magnetic Field in Monolayer $MoSe_2$* . *Phys. Rev. Lett.* **114**, 037401 (2015).
- [76] G. Aivazian, Z. Gong, A. M. Jones, R.-L. Chu, J. Yan, D. G. Mandrus, C. Zhang, D. Cobden, W. Yao, and X. Xu. *Magnetic control of valley pseudospin in monolayer WSe_2* . *Nat. Phys.* **11**, 148–152 (2015).
- [77] A. Srivastava, M. Sidler, A. V. Allain, D. S. Lembke, A. Kis, and A. Imamoglu. *Valley Zeeman effect in elementary optical excitations of monolayer WSe_2* . *Nat. Phys.* **11**, 141–147 (2015).
- [78] C. Robert, T. Amand, F. Cadiz, D. Lagarde, E. Courtade, M. Manca, T. Taniguchi, K. Watanabe, B. Urbaszek, and X. Marie. *Fine structure and lifetime of dark excitons in transition metal dichalcogenide monolayers*. *Phys. Rev. B* **96**, 155423 (2017).
- [79] M. Molas, A. Slobodeniuk, T. Kazimierzczuk, K. Nogajewski, M. Bartos, P. Kapuściński, K. Oreszczuk, K. Watanabe, T. Taniguchi, C. Faugeras, P. Kossacki, D. M. Basko, and M. Potemski. *Probing and manipulating valley coherence of dark excitons in monolayer WSe_2* . ArXiv e-prints (2019). [arXiv:1901.04431](https://arxiv.org/abs/1901.04431).
- [80] H. Rostami, A. G. Moghaddam, and R. Asgari. *Effective lattice Hamiltonian for monolayer MoS_2 : Tailoring electronic structure with perpendicular electric and magnetic fields*. *Phys. Rev. B* **88**, 085440 (2013).

- [81] G. F. Koster, J. O. Dimmock, R. G. Wheeler, and H. Statz. *Properties of the Thirty-Two Point Groups* (M.I.T. Press, 1963).
- [82] M. M. Glazov, T. Amand, X. Marie, D. Lagarde, L. Bouet, and B. Urbaszek. *Exciton fine structure and spin decoherence in monolayers of transition metal dichalcogenides*. *Phys. Rev. B* **89**, 201302 (2014).
- [83] H. Yu, X. Cui, X. Xu, and W. Yao. *Valley excitons in two-dimensional semiconductors*. *Natl. Sci. Rev.* **2**, 57–70 (2015).
- [84] D. Y. Qiu, F. H. da Jornada, and S. G. Louie. *Optical Spectrum of MoS₂: Many-Body Effects and Diversity of Exciton States*. *Phys. Rev. Lett.* **111**, 216805 (2013).
- [85] G. Wang, A. Chernikov, M. M. Glazov, T. F. Heinz, X. Marie, T. Amand, and B. Urbaszek. *Colloquium: Excitons in atomically thin transition metal dichalcogenides*. *Rev. Mod. Phys.* **90**, 021001 (2018).
- [86] D. Y. Qiu, T. Cao, and S. G. Louie. *Nonanalyticity, Valley Quantum Phases, and Lightlike Exciton Dispersion in Monolayer Transition Metal Dichalcogenides: Theory and First-Principles Calculations*. *Phys. Rev. Lett.* **115**, 176801 (2015).
- [87] J. O. Dimmock. In *Semiconductors and Semimetals*. Vol. 3, pp. 259–319. Edited by R. K. Willardson and A. C. Beer (Academic Press, 1967).
- [88] M. M. Glazov, E. L. Ivchenko, G. Wang, T. Amand, X. Marie, B. Urbaszek, and B. L. Liu. *Spin and valley dynamics of excitons in transition metal dichalcogenide monolayers*. *Phys. Status Solidi B* **252**, 2349–2362 (2015).
- [89] H. Yu, G.-B. Liu, P. Gong, X. Xu, and W. Yao. *Dirac cones and Dirac saddle points of bright excitons in monolayer transition metal dichalcogenides*. *Nat. Commun.* **5**, 3876 (2014).
- [90] Y. N. Gartstein, X. Li, and C. Zhang. *Exciton polaritons in transition-metal dichalcogenides and their direct excitation via energy transfer*. *Phys. Rev. B* **92**, 075445 (2015).
- [91] T. Yu and M. W. Wu. *Valley depolarization due to intervalley and intravalley electron-hole exchange interactions in monolayer MoS₂*. *Phys. Rev. B* **89**, 205303 (2014).
- [92] C. R. Zhu, K. Zhang, M. Glazov, B. Urbaszek, T. Amand, Z. W. Ji, B. L. Liu, and X. Marie. *Exciton valley dynamics probed by Kerr rotation in WSe₂ monolayers*. *Phys. Rev. B* **90**, 161302 (2014).
- [93] F. Wu, F. Qu, and A. H. MacDonald. *Exciton band structure of monolayer MoS₂*. *Phys. Rev. B* **91**, 075310 (2015).
- [94] H. Zhu, J. Yi, M.-Y. Li, J. Xiao, L. Zhang, C.-W. Yang, R. A. Kaindl, L.-J. Li, Y. Wang, and X. Zhang. *Observation of chiral phonons*. *Science* **359**, 579–582 (2018).
- [95] P. Y. Yu and M. Cardona. *Fundamentals of Semiconductors: Physics and Materials Properties*. 4th ed. (Springer, 2010).
- [96] R. Loudon. *The Raman effect in crystals*. *Adv. Phys.* **13**, 423–482 (1964).

- [97] R. M. Martin and T. C. Damen. *Breakdown of Selection Rules in Resonance Raman Scattering*. *Phys. Rev. Lett.* **26**, 86–88 (1971).
- [98] M. Hofmann. *Spectroscopy of localized excitons in carbon nanotubes*. Dissertation, Ludwig-Maximilians-Universität München (2016).
- [99] A. Neumann. *Cryogenic hyperspectroscopy of nanoemitters and atomically thin semiconductors*. Dissertation, Ludwig-Maximilians-Universität München (2017).
- [100] C. Kurtsiefer, S. Mayer, P. Zarda, and H. Weinfurter. *Stable Solid-State Source of Single Photons*. *Phys. Rev. Lett.* **85**, 290–293 (2000).
- [101] A. Gruber, A. Dräbenstedt, C. Tietz, L. Fleury, J. Wrachtrup, and C. v. Borczyskowski. *Scanning Confocal Optical Microscopy and Magnetic Resonance on Single Defect Centers*. *Science* **276**, 2012–2014 (1997).
- [102] F. Jelezko and J. Wrachtrup. *Single defect centres in diamond: A review*. *Phys. Status Solidi A* **203**, 3207–3225 (2006).
- [103] O. Gunawan, E. P. De Poortere, and M. Shayegan. *ALAs two-dimensional electrons in an antidot lattice: Electron pinball with elliptical Fermi contours*. *Phys. Rev. B* **75**, 081304 (2007).
- [104] D. Culcer, A. L. Saraiva, B. Koiller, X. Hu, and S. Das Sarma. *Valley-Based Noise-Resistant Quantum Computation Using Si Quantum Dots*. *Phys. Rev. Lett.* **108**, 126804 (2012).
- [105] A. Rycerz, J. Tworzydło, and C. W. J. Beenakker. *Valley filter and valley valve in graphene*. *Nat. Phys.* **3**, 172–175 (2007).
- [106] S. Tongay, J. Suh, C. Ataca, W. Fan, A. Luce, J. S. Kang, J. Liu, C. Ko, R. Raghunathanan, J. Zhou, F. Ogletree, J. Li, J. C. Grossman, and J. Wu. *Defects activated photoluminescence in two-dimensional semiconductors: interplay between bound, charged, and free excitons*. *Sci. Rep.* **3**, 2657 (2013).
- [107] G. Sallen, L. Bouet, X. Marie, G. Wang, C. R. Zhu, W. P. Han, Y. Lu, P. H. Tan, T. Amand, B. L. Liu, and B. Urbaszek. *Robust optical emission polarization in MoS₂ monolayers through selective valley excitation*. *Phys. Rev. B* **86**, 081301 (2012).
- [108] D. Lagarde, L. Bouet, X. Marie, C. R. Zhu, B. L. Liu, T. Amand, P. H. Tan, and B. Urbaszek. *Carrier and Polarization Dynamics in Monolayer MoS₂*. *Phys. Rev. Lett.* **112**, 047401 (2014).
- [109] S. Wu, J. S. Ross, G.-B. Liu, G. Aivazian, A. Jones, Z. Fei, W. Zhu, D. Xiao, W. Yao, D. Cobden, and X. Xu. *Electrical tuning of valley magnetic moment through symmetry control in bilayer MoS₂*. *Nat. Phys.* **9**, 149–153 (2013).
- [110] K. Hao, L. Xu, F. Wu, P. Nagler, K. Tran, X. Ma, C. Schüller, T. Korn, A. H. MacDonald, G. Moody, and X. Li. *Trion valley coherence in monolayer semiconductors*. *2D Mater.* **4**, 025105 (2017).
- [111] K. Tran, A. Singh, J. Seifert, Y. Wang, K. Hao, J.-K. Huang, L.-J. Li, T. Taniguchi, K. Watanabe, and X. Li. *Disorder-dependent valley properties in monolayer WSe₂*. *Phys. Rev. B* **96**, 041302 (2017).

- [112] K. Gołasa, M. Grzeszczyk, P. Leszczyński, C. Faugeras, A. A. L. Nicolet, A. Wysmołek, M. Potemski, and A. Babiński. *Multiphonon resonant Raman scattering in MoS_2* . *Appl. Phys. Lett.* **104**, 092106 (2014).
- [113] M. Staiger, R. Gillen, N. Scheuschner, O. Ochedowski, F. Kampmann, M. Schlegelberger, C. Thomsen, and J. Maultzsch. *Splitting of monolayer out-of-plane A'_1 Raman mode in few-layer WS_2* . *Phys. Rev. B* **91**, 195419 (2015).
- [114] T. Livneh and E. Sterer. *Resonant Raman scattering at exciton states tuned by pressure and temperature in 2H- MoS_2* . *Phys. Rev. B* **81**, 195209 (2010).
- [115] J.-H. Fan, P. Gao, A.-M. Zhang, B.-R. Zhu, H.-L. Zeng, X.-D. Cui, R. He, and Q.-M. Zhang. *Resonance Raman scattering in bulk 2H- MX_2 ($M=Mo, W$; $X=S, Se$) and monolayer MoS_2* . *J. Appl. Phys.* **115**, 053527 (2014).
- [116] T. Sohler, M. Calandra, and F. Mauri. *Two-dimensional Fröhlich interaction in transition-metal dichalcogenide monolayers: Theoretical modeling and first-principles calculations*. *Phys. Rev. B* **94**, 085415 (2016).
- [117] C.R. Zhu, G. Wang, B.L. Liu, X. Marie, X.F. Qiao, X. Zhang, X.X. Wu, H. Fan, P.H. Tan, T. Amand, and B. Urbaszek. *Strain tuning of optical emission energy and polarization in monolayer and bilayer MoS_2* . *Phys. Rev. B* **88**, 121301 (2013).
- [118] A. Castellanos-Gomez, R. Roldán, E. Cappelluti, M. Buscema, F. Guinea, H. S. J. van der Zant, and G. A. Steele. *Local Strain Engineering in Atomically Thin MoS_2* . *Nano Lett.* **13**, 5361–5366 (2013).
- [119] A. V. Stier, K.M. McCreary, B. T. Jonker, J. Kono, and S. A. Crooker. *Exciton diamagnetic shifts and valley Zeeman effects in monolayer WS_2 and MoS_2 to 65 Tesla*. *Nat. Commun.* **7**, 10643 (2016).
- [120] J. Ji, A. Zhang, J. Fan, Y. Li, X. Wang, J. Zhang, E. W. Plummer, and Q. Zhang. *Giant magneto-optical Raman effect in a layered transition metal compound*. *Proc. Natl. Acad. Sci. USA* **113**, 2349–2353 (2016).
- [121] T. Sekine, K. Uchinokura, T. Nakashizu, E. Matsuura, and R. Yoshizaki. *Dispersive Raman Mode of Layered Compound 2H- MoS_2 under the Resonant Condition*. *J. Phys. Soc. Jpn.* **53**, 811–818 (1984).
- [122] M. Sidler, P. Back, O. Cotlet, A. Srivastava, T. Fink, M. Kroner, E. Demler, and A. Imamoglu. *Fermi polaron-polaritons in charge-tunable atomically thin semiconductors*. *Nat. Phys.* **13**, 255–261 (2017).
- [123] F. Cadiz, E. Courtade, C. Robert, G. Wang, Y. Shen, H. Cai, T. Taniguchi, K. Watanabe, H. Carrere, D. Lagarde, M. Manca, T. Amand, P. Renucci, S. Tongay, X. Marie, and B. Urbaszek. *Excitonic Linewidth Approaching the Homogeneous Limit in MoS_2 -Based van der Waals Heterostructures*. *Phys. Rev. X* **7**, 021026 (2017).
- [124] D. Van Tuan, A.M. Jones, M. Yang, X. Xu, and H. Dery. *Virtual trions in the photoluminescence of monolayer transition-metal dichalcogenides*. ArXiv e-prints (2018). [arXiv:1805.08722](https://arxiv.org/abs/1805.08722).

- [125] A. M. Jones, H. Yu, J. R. Schaibley, J. Yan, D. G. Mandrus, T. Taniguchi, K. Watanabe, H. Dery, W. Yao, and X. Xu. *Excitonic luminescence upconversion in a two-dimensional semiconductor*. *Nat. Phys.* **12**, 323–327 (2015).
- [126] C. R. Dean, A. F. Young, I. Meric, C. Lee, L. Wang, S. Sorgenfrei, K. Watanabe, T. Taniguchi, P. Kim, K. Shepard, and J. Hone. *Boron nitride substrates for high-quality graphene electronics*. *Nat. Nanotechnol.* **5**, 722–726 (2010).
- [127] O. Ajayi, J. Ardelean, G. Shepard, J. Wang, A. Antony, T. Taniguchi, K. Watanabe, T. Heinz, S. Strauf, X.-Y. Zhu, and J. C. Hone. *Approaching the Intrinsic Photoluminescence Linewidth in Transition Metal Dichalcogenide Monolayers*. *2D Mater.* **4**, 031011 (2017).
- [128] C. Jin, J. Kim, J. Suh, Z. Shi, B. Chen, X. Fan, M. Kam, K. Watanabe, T. Taniguchi, S. Tongay, A. Zettl, J. Wu, and F. Wang. *Interlayer electron-phonon coupling in WSe_2/hBN heterostructures*. *Nat. Phys.* **13**, 127–131 (2016).
- [129] J. P. Echeverry, B. Urbaszek, T. Amand, X. Marie, and I. C. Gerber. *Splitting between bright and dark excitons in transition metal dichalcogenide monolayers*. *Phys. Rev. B* **93**, 121107 (2016).
- [130] M. Selig, G. Berghäuser, A. Raja, P. Nagler, C. Schüller, T. F. Heinz, T. Korn, A. Chernikov, E. Malic, and A. Knorr. *Excitonic linewidth and coherence lifetime in monolayer transition metal dichalcogenides*. *Nat. Commun.* **7**, 13279 (2016).
- [131] M. Selig, G. Berghäuser, M. Richter, R. Bratschitsch, A. Knorr, and E. Malic. *Dark and bright exciton formation, thermalization, and photoluminescence in monolayer transition metal dichalcogenides*. *2D Mater.* **5**, 035017 (2018).
- [132] J. R. Chelikowsky and M. L. Cohen. *Nonlocal pseudopotential calculations for the electronic structure of eleven diamond and zinc-blende semiconductors*. *Phys. Rev. B* **14**, 556–582 (1976).
- [133] G. Cassabois, P. Valvin, and B. Gil. *Hexagonal boron nitride is an indirect bandgap semiconductor*. *Nat. Photonics* **10**, 262–266 (2016).
- [134] A. Chernikov, A. M. van der Zande, H. M. Hill, A. F. Rigosi, A. Velauthapillai, J. Hone, and T. F. Heinz. *Electrical Tuning of Exciton Binding Energies in Monolayer WS_2* . *Phys. Rev. Lett.* **115**, 126802 (2015).
- [135] G. Cassabois, P. Valvin, and B. Gil. *Intervalley scattering in hexagonal boron nitride*. *Phys. Rev. B* **93**, 035207 (2016).
- [136] X. Zhang, X.-F. Qiao, W. Shi, J.-B. Wu, D.-S. Jiang, and P.-H. Tan. *Phonon and Raman scattering of two-dimensional transition metal dichalcogenides from monolayer, multilayer to bulk material*. *Chem. Soc. Rev.* **44**, 2757–2785 (2015).
- [137] E. Courtade, M. Semina, M. Manca, M. M. Glazov, C. Robert, F. Cadiz, G. Wang, T. Taniguchi, K. Watanabe, M. Pierre, W. Escoffier, E. L. Ivchenko, P. Renucci, X. Marie, T. Amand, and B. Urbaszek. *Charged excitons in monolayer WSe_2 : Experiment and theory*. *Phys. Rev. B* **96**, 085302 (2017).
- [138] E. Malic, M. Selig, M. Feierabend, S. Brem, D. Christiansen, F. Wendler, A. Knorr, and G. Berghäuser. *Dark excitons in transition metal dichalcogenides*. *Phys. Rev. Mater.* **2**, 014002 (2018).

- [139] G. Wang, L. Bouet, D. Lagarde, M. Vidal, A. Balocchi, T. Amand, X. Marie, and B. Urbaszek. *Valley dynamics probed through charged and neutral exciton emission in monolayer WSe_2* . *Phys. Rev. B* **90**, 075413 (2014).
- [140] A. Arora, M. Koperski, K. Nogajewski, J. Marcus, C. Faugeras, and M. Potemski. *Excitonic resonances in thin films of WSe_2 : from monolayer to bulk material*. *Nanoscale* **7**, 10421–10429 (2015).
- [141] T. Smoleński, M. Goryca, M. Koperski, C. Faugeras, T. Kazimierczuk, A. Bogucki, K. Nogajewski, P. Kossacki, and M. Potemski. *Tuning Valley Polarization in a WSe_2 Monolayer with a Tiny Magnetic Field*. *Phys. Rev. X* **6**, 021024 (2016).
- [142] D.-H. Lien, J.S. Kang, M. Amani, K. Chen, M. Tosun, H.-P. Wang, T. Roy, M. S. Eggleston, M. C. Wu, M. Dubey, S.-C. Lee, J.-H. He, and A. Javey. *Engineering Light Outcoupling in 2D Materials*. *Nano Lett.* **15**, 1356–1361 (2015).
- [143] G. Scuri, Y. Zhou, A. A. High, D. S. Wild, C. Shu, K. De Greve, L. A. Jauregui, T. Taniguchi, K. Watanabe, P. Kim, M. D. Lukin, and H. Park. *Large Excitonic Reflectivity of Monolayer $MoSe_2$ Encapsulated in Hexagonal Boron Nitride*. *Phys. Rev. Lett.* **120**, 037402 (2018).
- [144] C. Robert, M. A. Semina, F. Cadiz, M. Manca, E. Courtade, T. Taniguchi, K. Watanabe, H. Cai, S. Tongay, B. Lassagne, P. Renucci, T. Amand, X. Marie, M. M. Glazov, and B. Urbaszek. *Optical spectroscopy of excited exciton states in MoS_2 monolayers in van der Waals heterostructures*. *Phys. Rev. Mater.* **2**, 011001 (2018).
- [145] S. Refaely-Abramson, D. Y. Qiu, S. G. Louie, and J. B. Neaton. *Defect-Induced Modification of Low-Lying Excitons and Valley Selectivity in Monolayer Transition Metal Dichalcogenides*. *Phys. Rev. Lett.* **121**, 167402 (2018).
- [146] G. Wang, M. M. Glazov, C. Robert, T. Amand, X. Marie, and B. Urbaszek. *Double Resonant Raman Scattering and Valley Coherence Generation in Monolayer WSe_2* . *Phys. Rev. Lett.* **115**, 117401 (2015).
- [147] M. Feierabend, A. Morlet, G. Berghäuser, and E. Malic. *Impact of strain on the optical fingerprint of monolayer transition-metal dichalcogenides*. *Phys. Rev. B* **96**, 045425 (2017).
- [148] M. Barbone, A. R.-P. Montblanch, D. M. Kara, C. Palacios-Berraquero, A. R. Cadore, D. De Fazio, B. Pingault, E. Mostaani, H. Li, B. Chen, K. Watanabe, T. Taniguchi, S. Tongay, G. Wang, A. C. Ferrari, and M. Atatüre. *Charge-tuneable biexciton complexes in monolayer WSe_2* . *Nat. Commun.* **9**, 3721 (2018).
- [149] Z. Li, T. Wang, Z. Lu, C. Jin, Y. Chen, Y. Meng, Z. Lian, T. Taniguchi, K. Watanabe, S. Zhang, D. Smirnov, and S.-F. Shi. *Revealing the biexciton and trion-exciton complexes in BN encapsulated WSe_2* . *Nat. Commun.* **9**, 3719 (2018).
- [150] A. Steinhoff, M. Florian, A. Singh, K. Tran, M. Kolarczik, S. Helmrich, A. W. Achtstein, U. Woggon, N. Owschimikow, F. Jahnke, and X. Li. *Biexciton fine structure in monolayer transition metal dichalcogenides*. *Nat. Phys.* **14**, 1199–1204 (2018).

- [151] Z. Ye, L. Waldecker, E. Y. Ma, D. Rhodes, A. Antony, B. Kim, X.-X. Zhang, M. Deng, Y. Jiang, Z. Lu, D. Smirnov, K. Watanabe, T. Taniguchi, J. Hone, and T. F. Heinz. *Efficient generation of neutral and charged biexcitons in encapsulated WSe₂ monolayers*. *Nat. Commun.* **9**, 3718 (2018).
- [152] J. C. Kim, D. R. Wake, and J. P. Wolfe. *Thermodynamics of biexcitons in a GaAs quantum well*. *Phys. Rev. B* **50**, 15099–15107 (1994).
- [153] S. Mouri, Y. Miyauchi, M. Toh, W. Zhao, G. Eda, and K. Matsuda. *Nonlinear photoluminescence in atomically thin layered WSe₂ arising from diffusion-assisted exciton-exciton annihilation*. *Phys. Rev. B* **90**, 155449 (2014).
- [154] N. Kumar, Q. Cui, F. Ceballos, D. He, Y. Wang, and H. Zhao. *Exciton-exciton annihilation in MoSe₂ monolayers*. *Phys. Rev. B* **89**, 125427 (2014).
- [155] D. Sun, Y. Rao, G. A. Reider, G. Chen, Y. You, L. Brézin, A. R. Harutyunyan, and T. F. Heinz. *Observation of Rapid Exciton-Exciton Annihilation in Monolayer Molybdenum Disulfide*. *Nano Lett.* **14**, 5625–5629 (2014).
- [156] M. Danovich, V. Zóyomi, V. I. Fal’ko, and I. L. Aleiner. *Auger recombination of dark excitons in WS₂ and WSe₂ monolayers*. *2D Mater.* **3**, 035011 (2016).
- [157] M. Koperski, M. R. Molas, A. Arora, K. Nogajewski, M. Bartos, J. Wyzula, D. Vaclavkova, P. Kossacki, and M. Potemski. *Orbital, spin and valley contributions to Zeeman splitting of excitonic resonances in MoSe₂, WSe₂ and WS₂ Monolayers*. *2D Mater.* **6**, 015001 (2019).
- [158] A. Kuc, N. Zibouche, and T. Heine. *Influence of quantum confinement on the electronic structure of the transition metal sulfide TS₂*. *Phys. Rev. B* **83**, 245213 (2011).
- [159] A. Kumar and P. K. Ahluwalia. *Electronic structure of transition metal dichalcogenides monolayers 1H-MX₂ (M = Mo, W; X = S, Se, Te) from ab-initio theory: new direct band gap semiconductors*. *Eur. Phys. J. B* **85**, 186 (2012).
- [160] T. Cheiwchanchamnangij and W. R. L. Lambrecht. *Quasiparticle band structure calculation of monolayer, bilayer, and bulk MoS₂*. *Phys. Rev. B* **85**, 205302 (2012).
- [161] N. R. Wilson, P. V. Nguyen, K. Seyler, P. Rivera, A. J. Marsden, Z. P. Laker, G. C. Constantinescu, V. Kandyba, A. Barinov, N. D. M. Hine, X. Xu, and D. H. Cobden. *Determination of band offsets, hybridization, and exciton binding in 2D semiconductor heterostructures*. *Sci. Adv.* **3**, 1601832 (2017).
- [162] A. Ramasubramaniam, D. Naveh, and E. Towe. *Tunable band gaps in bilayer transition-metal dichalcogenides*. *Phys. Rev. B* **84**, 205325 (2011).
- [163] W. S. Yun, S. W. Han, S. C. Hong, I. G. Kim, and J. D. Lee. *Thickness and strain effects on electronic structures of transition metal dichalcogenides: 2H-MX₂ semiconductors (M = Mo, W; X = S, Se, Te)*. *Phys. Rev. B* **85**, 033305 (2012).
- [164] W. Zhao, Z. Ghorannevis, L. Chu, M. Toh, C. Kloc, P.-H. Tan, and G. Eda. *Evolution of Electronic Structure in Atomically Thin Sheets of WS₂ and WSe₂*. *ACS Nano* **7**, 791–797 (2013).

- [165] H. Sahin, S. Tongay, S. Horzum, W. Fan, J. Zhou, J. Li, J. Wu, and F. M. Peeters. *Anomalous Raman spectra and thickness-dependent electronic properties of WSe_2* . *Phys. Rev. B* **87**, 165409 (2013).
- [166] D. Wickramaratne, F. Zahid, and R. K. Lake. *Electronic and thermoelectric properties of few-layer transition metal dichalcogenides*. *J. Chem. Phys.* **140**, 124710 (2014).
- [167] H. Terrones and M. Terrones. *Bilayers of transition metal dichalcogenides: Different stackings and heterostructures*. *J. Mater. Res.* **29**, 373–382 (2014).
- [168] M. Kira and S. Koch. *Many-body correlations and excitonic effects in semiconductor spectroscopy*. *Prog. Quant. Electron.* **30**, 155–296 (2006).
- [169] H. Haug and S. W. Koch. *Quantum Theory of the Optical and Electronic Properties of Semiconductors*. 5th ed. (World Scientific Publishing, 2009).
- [170] L. V. Keldysh. *Coulomb interaction in thin semiconductor and semimetal films*. *J. Exp. Theor. Phys. Lett.* **29**, 658 (1978).
- [171] P. Cudazzo, I. V. Tokatly, and A. Rubio. *Dielectric screening in two-dimensional insulators: Implications for excitonic and impurity states in graphene*. *Phys. Rev. B* **84**, 085406 (2011).
- [172] G. Berghäuser and E. Malic. *Analytical approach to excitonic properties of MoS_2* . *Phys. Rev. B* **89**, 125309 (2014).
- [173] S. B. Desai, G. Seol, J. S. Kang, H. Fang, C. Battaglia, R. Kapadia, J. W. Ager, J. Guo, and A. Javey. *Strain-Induced Indirect to Direct Bandgap Transition in Multilayer WSe_2* . *Nano Lett.* **14**, 4592–4597 (2014).
- [174] M. Bayer, G. Ortner, O. Stern, A. Kuther, A. A. Gorbunov, A. Forchel, P. Hawrylak, S. Fafard, K. Hinzer, T. L. Reinecke, S. N. Walck, J. P. Reithmaier, F. Klopff, and F. Schäfer. *Fine structure of neutral and charged excitons in self-assembled $In(Ga)As/(Al)GaAs$ quantum dots*. *Phys. Rev. B* **65**, 195315 (2002).
- [175] P. Rivera, J. R. Schaibley, A. M. Jones, J. S. Ross, S. Wu, G. Aivazian, P. Klement, K. Seyler, G. Clark, N. J. Ghimire, J. Yan, D. G. Mandrus, W. Yao, and X. Xu. *Observation of long-lived interlayer excitons in monolayer $MoSe_2$ - WSe_2 heterostructures*. *Nat. Commun.* **6**, 6242 (2015).
- [176] Y. Gong, J. Lin, X. Wang, G. Shi, S. Lei, Z. Lin, X. Zou, G. Ye, R. Vajtai, B. I. Yakobson, H. Terrones, M. Terrones, B. K. Tay, J. Lou, S. T. Pantelides, Z. Liu, W. Zhou, and P. M. Ajayan. *Vertical and in-plane heterostructures from WS_2/MoS_2 monolayers*. *Nat. Mater.* **13**, 1135–1142 (2014).
- [177] M.-Y. Li, Y. Shi, C.-C. Cheng, L.-S. Lu, Y.-C. Lin, H.-L. Tang, M.-L. Tsai, C.-W. Chu, K.-H. Wei, J.-H. He, W.-H. Chang, K. Suenaga, and L.-J. Li. *Epitaxial growth of a monolayer WSe_2 - MoS_2 lateral p-n junction with an atomically sharp interface*. *Science* **349**, 524–528 (2015).
- [178] J. Kang, J. Li, S.-S. Li, J.-B. Xia, and L.-W. Wang. *Electronic Structural Moiré Pattern Effects on $MoS_2/MoSe_2$ 2D Heterostructures*. *Nano Lett.* **13**, 5485–5490 (2013).

- [179] Q. Tong, H. Yu, Q. Zhu, Y. Wang, X. Xu, and W. Yao. *Topological mosaics in moire superlattices of van der Waals heterobilayers*. *Nat. Phys.* **13**, 356–362 (2016).
- [180] C. Zhang, C.-P. Chuu, X. Ren, M.-Y. Li, L.-J. Li, C. Jin, M.-Y. Chou, and C.-K. Shih. *Interlayer couplings, Moiré patterns, and 2D electronic superlattices in $\text{MoS}_2/\text{WSe}_2$ hetero-bilayers*. *Sci. Adv.* **3**, e1601459 (2017).
- [181] F. Wu, T. Lovorn, and A.H. MacDonald. *Topological Exciton Bands in Moiré Heterojunctions*. *Phys. Rev. Lett.* **118**, 147401 (2017).
- [182] F. Wu, T. Lovorn, and A. H. MacDonald. *Theory of optical absorption by interlayer excitons in transition metal dichalcogenide heterobilayers*. *Phys. Rev. B* **97**, 035306 (2018).
- [183] H. Yu, Y. Wang, Q. Tong, X. Xu, and W. Yao. *Anomalous Light Cones and Valley Optical Selection Rules of Interlayer Excitons in Twisted Heterobilayers*. *Phys. Rev. Lett.* **115**, 187002 (2015).
- [184] Y. Gong, S. Lei, G. Ye, B. Li, Y. He, K. Keyshar, X. Zhang, Q. Wang, J. Lou, Z. Liu, R. Vajtai, W. Zhou, and P.M. Ajayan. *Two-Step Growth of Two-Dimensional $\text{WSe}_2/\text{MoSe}_2$ Heterostructures*. *Nano Lett.* **15**, 6135–6141 (2015).
- [185] J. He, K. Hummer, and C. Franchini. *Stacking effects on the electronic and optical properties of bilayer transition metal dichalcogenides MoS_2 , MoSe_2 , WS_2 , and WSe_2* . *Phys. Rev. B* **89**, 075409 (2014).
- [186] B. Miller, A. Steinhoff, B. Pano, J. Klein, F. Jahnke, A. Holleitner, and U. Wurstbauer. *Long-Lived Direct and Indirect Interlayer Excitons in van der Waals Heterostructures*. *Nano Lett.* **17**, 5229–5237 (2017).
- [187] C. Jiang, W. Xu, A. Rasmita, Z. Huang, K. Li, Q. Xiong, and W.-b. Gao. *Microsecond dark-exciton valley polarization memory in two-dimensional heterostructures*. *Nat. Commun.* **9**, 753 (2018).
- [188] P. Nagler, G. Plechinger, M. Ballotin, A. Mitioglu, S. Meier, N. Paradiso, C. Strunk, A. Chernikov, P. Christianen, C. Schüller, and T. Korn. *Interlayer exciton dynamics in a dichalcogenide monolayer heterostructure*. *2D Mater.* **4**, 025112 (2017).
- [189] S. Seidl, M. Kroner, P. A. Dalgarno, A. Högele, J.M. Smith, M. Ediger, B.D. Gerardot, J. M. Garcia, P. M. Petroff, K. Karrai, and R. J. Warburton. *Absorption and photoluminescence spectroscopy on a single self-assembled charge-tunable quantum dot*. *Phys. Rev. B* **72**, 195339 (2005).
- [190] Y. Luo, G.D. Shepard, J.V. Ardelean, D.A. Rhodes, B. Kim, K. Barmak, J.C. Hone, and S. Strauf. *Deterministic coupling of site-controlled quantum emitters in monolayer WSe_2 to plasmonic nanocavities*. *Nat. Nanotechnol.* **13**, 1137–1142 (2018).
- [191] X. Lu, X. Chen, S. Dubey, Q. Yao, X. Wang, Q. Xiong, and A. Srivastava. *Optical control of a single spin-valley in charged WSe_2 quantum dots*. ArXiv e-prints (2018). [arXiv:1810.01887](https://arxiv.org/abs/1810.01887).
- [192] P. Rivera, K. L. Seyler, H. Yu, J. R. Schaibley, J. Yan, D. G. Mandrus, W. Yao, and X. Xu. *Valley-polarized exciton dynamics in a 2D semiconductor heterostructure*. *Science* **351**, 688–691 (2016).

- [193] M. M. Fogler, L. V. Butov, and K. S. Novoselov. *High-temperature superfluidity with indirect excitons in van der Waals heterostructures*. *Nat. Commun.* **5**, 4555 (2014).
- [194] J. P. Eisenstein and A. H. MacDonald. *Bose-Einstein condensation of excitons in bilayer electron systems*. *Nature* **432**, 691 (2004).
- [195] F. P. Laussy, A. V. Kavokin, and I. A. Shelykh. *Exciton-Polariton Mediated Superconductivity*. *Phys. Rev. Lett.* **104**, 106402 (2010).
- [196] O. Cotlet, S. Zeytinoglu, M. Sigrist, E. Demler, and A. Imamoglu. *Superconductivity and other collective phenomena in a hybrid Bose-Fermi mixture formed by a polariton condensate and an electron system in two dimensions*. *Phys. Rev. B* **93**, 054510 (2016).
- [197] D. N. Basov, M. M. Fogler, and F. J. García de Abajo. *Polaritons in van der Waals materials*. *Science* **354**, 195 (2016).
- [198] H. Yu, G.-B. Liu, J. Tang, X. Xu, and W. Yao. *Moiré excitons: From programmable quantum emitter arrays to spin-orbit-coupled artificial lattices*. *Sci. Adv.* **3**, e1701696 (2017).
- [199] K. L. Seyler, P. Rivera, H. Yu, N. P. Wilson, E. L. Ray, D. Mandrus, J. Yan, W. Yao, and X. Xu. *Signatures of moiré-trapped valley excitons in $\text{MoSe}_2/\text{WSe}_2$ heterobilayers*. ArXiv e-prints (2018). [arXiv:1809.04562](https://arxiv.org/abs/1809.04562).
- [200] L. Jiang, Z. Shi, B. Zeng, S. Wang, J.-H. Kang, T. Joshi, C. Jin, L. Ju, J. Kim, T. Lyu, Y.-R. Shen, M. Crommie, H.-J. Gao, and F. Wang. *Soliton-dependent plasmon reflection at bilayer graphene domain walls*. *Nat. Mater.* **15**, 840 (2016).
- [201] S. S. Sunku, G. X. Ni, B. Y. Jiang, H. Yoo, A. Sternbach, A. S. McLeod, T. Stauber, L. Xiong, T. Taniguchi, K. Watanabe, P. Kim, M. M. Fogler, and D. N. Basov. *Photonic crystals for nano-light in moiré graphene superlattices*. *Science* **362**, 1153–1156 (2018).
- [202] R. Bistritzer and A. H. MacDonald. *Moiré bands in twisted double-layer graphene*. *Proc. Natl. Acad. Sci. USA* **108**, 12233–12237 (2011).
- [203] Y. Cao, V. Fatemi, A. Demir, S. Fang, S. L. Tomarken, J. Y. Luo, J. D. Sanchez-Yamagishi, K. Watanabe, T. Taniguchi, E. Kaxiras, R. C. Ashoori, and P. Jarillo-Herrero. *Correlated insulator behaviour at half-filling in magic-angle graphene superlattices*. *Nature* **556**, 80 (2018).
- [204] Y. Cao, V. Fatemi, S. Fang, K. Watanabe, T. Taniguchi, E. Kaxiras, and P. Jarillo-Herrero. *Unconventional superconductivity in magic-angle graphene superlattices*. *Nature* **556**, 43 (2018).
- [205] J. C. W. Song and N. M. Gabor. *Electron quantum metamaterials in van der Waals heterostructures*. *Nat. Nanotechnol.* **13**, 986–993 (2018).
- [206] K. F. Mak and J. Shan. *Opportunities and challenges of interlayer exciton control and manipulation*. *Nat. Nanotechnol.* **13**, 974–976 (2018).

Danksagung

Einen großen Beitrag zum Gelingen dieser Arbeit tragen all diejenigen, die mich die letzten Jahre begleitet und unterstützt haben.

Zuallererst möchte ich mich bei Alex Högele bedanken, für die Möglichkeit in einer angenehmen wissenschaftlichen Atmosphäre zweidimensionale Kristalle zu spektroskopieren. Vielen Dank Alex, dass du trotz deiner vielen Aufgaben stets Zeit gefunden hast aktuelle Daten zu enträtseln um die Experimente in eine aussichtsreiche Richtung zu lenken. Deine Art mit den Daten zu kommunizieren war sehr inspirierend für mich und gab mir das nötige Durchhaltevermögen Valleys zu überwinden. Vielen Dank für die finanzielle Unterstützung, die es mir auch ermöglicht hat, an einigen internationalen Konferenzen teilzunehmen.

Bei Jörg Kotthaus möchte ich mich für die einzigartige Lehrstuhlumgebung bedanken, die sich über die Jahre etabliert hat. Durch diverse Exzellenzinitiativen ist München zu einem herausragenden Standpunkt für Nanowissenschaften geworden.

I am very grateful to our collaborators for their contributions that enabled the success of individual projects: Tim Liedl and Tao Zhang (LMU) for introducing me to the world of DNA-origami. Hisato Yamaguchi (Los Alamos) for the fabrication of CVD-grown TMD crystals. Feng Wang (Berkeley) for providing a crucial WSe_2 sample. Special thanks also to Takashi Taniguchi (Japan) for providing highest quality hBN. Ermin Malic and Gunnar Berghäuser (Sweden) for their theory support. Many thanks to Ursula Wurstbauer and Bastian Miller (TUM) for the numerous discussions about phonons that triggered my interest in Raman spectroscopy. Thank you Ursula for kindly accepting to review this thesis. Furthermore, I want to thank our collaborators Bernhard Urbaszek and Xavier Marie (Toulouse), and Misha Glazov (St. Petersburg) with whom we started our journey to the dark side of excitons.

Einen wesentlichen Anteil zum Gelingen dieser Arbeit trägt Andre Neumann, mit dem ich eng zusammen gearbeitet habe. Vielen Dank für deine vielen Ratschläge und Tipps, die mir entscheidend geholfen haben Dreiecke und Sterne leuchten zu sehen. Unsere legendären Teepausen, bei denen wir aktuelle Daten und Paper diskutierten waren stets ein Highlight für mich. Vielen Dank für deine Unterstützung in allen Lebenslagen und Korrekturlesen meiner Arbeit.

Many thanks to Léo Colombier for the instructive discussions about symmetry groups and phonon selection rules. Danke an Lorenz Mayr und Lukas Renn, für das rege Engagement im Labor und die wertvollen Beiträge zur Charakterisierung von Tieftemperatur-Objektiven. Besonderer Dank geht auch an Victor Funk,

Jonathan Förste und Michi Förg für die Herstellung qualitativ hochwertiger, ladungsdurchstimmbarer TMD Proben und entscheidender Beiträge zum Bilagenprojekt.

Allen ehemaligen und derzeitigen Mitgliedern der Nanophotonik Gruppe möchte ich für die gute Atmosphäre auch außerhalb des Arbeitsalltages danken. Insbesondere auch meinen Bürokollegen Jonathan Noé, Manuel Nutz, Michi Förg und neuerdings Victor Funk und Jonathan Förste für eine humorvolle Abwechslung zwischendurch. Vielen Dank Manuel für deine Hilfsbereitschaft hinsichtlich IT-Fragen.

Besonders danken möchte ich auch Martina Edenhofer und Bert Lorenz für die administrative Unterstützung, die den Lehrstuhl zusammen hält. Vielen Dank an Anton Heindl und Reinhold Rath für technische Hilfe und regelmäßige Versorgung mit flüssigem Stickstoff und Helium. Die hervorragende Unterstützung durch Philipp Altpeter im Reinraum und Stefan Manus bei elektronischen Fragen war immer sehr hilfreich. Vielen Dank der Werkstatt mit Jürgen Aust und Thomas Großhauser für die Herstellung einiger mechanischer Komponenten.

Außerhalb der Uni möchte ich mich bei meinen Freunden für die Unterstützung bedanken und dem Team MGC für die nötige Abwechslung unter freiem Himmel neue Motivation zu finden.

Meiner lieben Familie danke ich besonders für den Zusammenhalt, dass sie immer für mich da waren, vor allem meinen Eltern Marina und Peter, und meiner Schwester Annika. Vielen Dank Andre, dass du mich in schwierigen Zeiten beruhigt und aufgebaut hast und immer an meiner Seite warst.